EFFICIENT MODELING OF THE INCOMPRESSIBLE FLOW WITH MODERATE LARGE REYNOLDS NUMBERS USING A DECONVOLUTION-BASED LERAY MODEL: ANALYSIS, UNCERTAINTY QUANTIFICATION AND APPLICATION IN AORTIC DISSECTIONS

A Dissertation
Presented to
The Academic Faculty

By

Huijuan Xu

In Partial Fulfillment
of the Requirements for the Degree
Doctor of Philosophy in the
George W. Woodruff School of Mechanical Engineering

Georgia Institute of Technology

May 2020

EFFICIENT MODELING OF THE INCOMPRESSIBLE FLOW WITH MODERATE LARGE REYNOLDS NUMBERS USING A DECONVOLUTION-BASED LERAY MODEL: ANALYSIS, UNCERTAINTY QUANTIFICATION AND APPLICATION IN AORTIC DISSECTIONS

Approved by:

Dr. Alessandro Veneziani, Advisor
School of Mathematics
Emory University

Dr. Robert M. Nerem, Co-Advisor
George W. Woodruff School of Mechanical Engineering
Georgia Institute of Technology

Dr. Alexander Alexeev
George W. Woodruff School of Mechanical Engineering
Georgia Institute of Technology

Dr. Rudolph L. Gleason
George W. Woodruff School of Mechanical Engineering
Georgia Institute of Technology

Dr. Robert Taylor
The Wallace H. Coulter Department of Biomedical Engineering
Georgia Institute of Technology

Dr. Bradley Leshnower
School of Medicine
Emory University

Date Approved: December 18, 2019

What I hear, I forget; What I see, I remember; What I do, I understand.

Confucius, 551-479 BC

To my family.

ACKNOWLEDGMENTS

First of all, I would like to express my gratitude to my thesis advisor, Dr. Alessandro Veneziani, for his continuous support and encouragement throughout my research. He introduced me to computational mathematics and mentored me with endless enthusiasm, patience and expertise. In addition, I would like to thank Dr. Veneziani for providing a collaborative research environment, introducing me to many amazing collaborators, as well as keeping the best interests of his students as a top priority.

I would like to thank my co-advisor Dr. Robert Nerem for his encouragement, support and many fruitful discussions during my research.

I would like to thank the rest of my thesis committee, Dr. Alexander Alexeev, Dr. Rudolph Gleason, Dr. Robert Taylor and Dr. Bradley Leshnower for reviewing my work, providing insightful comments and support.

I would like to thank my collaborators, Dr. Marina Piccinelli from the Department of Radiology and Imaging Sciences, Dr. Davide Baroli currently working at Aachen Institute for Advanced Study in Computational Engineering Science (DE), Dr. Adrien Lefieux as well as Dr. Annalisa Quaini. It is a great pleasure to work with them. All the research discussions with them are motivating, insightful and help me to widen my research perspective.

I would like to thank my labmates, Sofia Guzzetti and Alessandro Barone for their help and companion along the way.

Last but not the least, this work is dedicated to my family. I would not be who I am today without their unconditional love, encouragement and support. Special thanks go to my husband Yaroslav Vasyliv for spending our Ph.D. student lives together.

TABLE OF CONTENTS

LIST OF TABLES

LIST OF FIGURES

LIST OF ABBREVIATIONS

3WK Three-Element Windkessel. 26

AD Aortic Dissection. 1

CFD Computational Fluid Dynamics. 3

CoV Coefficient of Variation. 68, 74

cTBAD Complicated Type B Aortic Dissection. 2

DNS Direct Numerical Simulation. 4

FL False Lumen. 1–3

LES Large Eddy Simulation. 4

LSA Left Subclavian Artery. 89

OMT Optimal Medical Treatment. 2

OSI Oscillatory Shear Index. 29

PCE Polynomial Chaos Expansion. 17

QoI Quantity of Interest. 6, 7, 17

RANS Reynolds Average Navier Stokes. 4, 7

RRT Relative Residence Time. 3, 29

TAWSS Time Averaged Wall Shear Stress. 29

TBAD Type B Aortic Dissection. 1

TEVAR Thoracic Endovascular Aortic Repair. 2

TL True Lumen. 1, 3

uTBAD Uncomplicated Type B Aortic Dissection. 2

WSS Wall Shear Stress. 3, 28

SUMMARY

Progressive false lumen aneurysmal degeneration in the acute uncomplicated type B aortic dissection is a complex process with a combination of mechanical and biological etiologies. Patient-specific Computational Fluid Dynamics (CFD) provides spatial and temporal hemodynamic quantities that facilitate understanding of this disease progression. However, due to the moderate large Reynolds number and complex geometries, Direct Numerical Simulation (DNS) could be intimidatingly computational expensive. As a Large Eddy Simulation (LES) model, the Leray model solves the flow structure at large scales while models the effect of the small-scale flows using a deconvolution-based differential filter, whose efficiency and accuracy make it a promising candidate for the hemodynamic problem in human aortas. In order to evaluate the robustness of the model prediction, Uncertainty Quantification (UQ) and sensitivity analysis are necessary for understanding the effects of the model parameter and patients' data. The goal of this work is to develop and analyze the deconvolution-based Leray model for the incompressible flow problem in the hemodynamics of aortic dissections, to quantify the model uncertainty, and to apply the model to investigate the prognostic factors for the late complication of the originally uncomplicated type B aortic dissection in order to facilitate the decision of the less invasive early surgical intervention. The specific aims are: Aim 1, development and implementation of the deconvolution-based Leray model using the Finite Element Method. Aim 2, analysis of using the Leray model for suppressing the backflow instability, a common numerical instability in hemodynamic simulations. Aim 3, sensitivity analysis and uncertainty quantification of the influence of the Leray model parameter and patients' data. Aim 4, investigation of the hemodynamic indication factors of early surgical intervention for the acute uncomplicated type B aortic dissection by correlating the hemodynamic factors and false lumen degeneration in time.

CHAPTER 1
INTRODUCTION

1.1 Background: the Clinical Motivation

The acute Aortic Dissection (AD) is the most common catastrophic aortic-syndrome with the incidence of 35 per million per year [1]. In AD, tears occur in the intimal layer of the aortic wall, allowing the blood to flow in and divide the intimal-medial layer (Fig. 1.1). This, in turn, creates a new channel of blood flow known as the False Lumen (FL) [2]. The original lumen is referred to as the True Lumen (TL). AD is considered acute if the symptoms occur within two weeks after the onset of the dissection, subacute if within two to four weeks, otherwise it is considered chronic [3]. AD distal to the left subclavian artery is classified as "type B" according to the Stanford classification (Fig. 1.1).

While patients diagnosed of the Type B Aortic Dissection (TBAD) with complicated

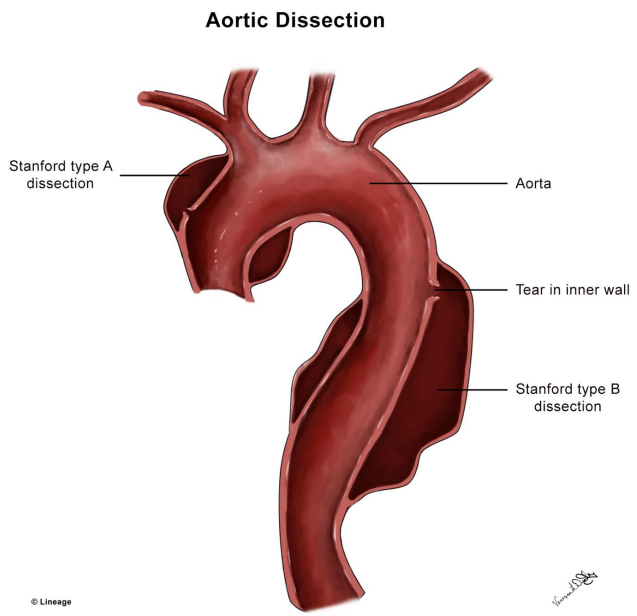

Figure 1.1: A schematic drawing of the aortic dissection (https:medbullets.com).

conditions, i.e. rupture or organ malperfusion, receive surgical interventions, acute Uncomplicated Type B Aortic Dissection (uTBAD) is commonly managed with the Optimal Medical Treatment (OMT). However, for patients with uTBAD, the OMT is associated with a high rate of late aneurysmal degeneration of the FL and consequently requiring the open or endovascular interventions [4, 5].

Thoracic Endovascular Aortic Repair (TEVAR) has replaced open surgery in most patients with acute Complicated Type B Aortic Dissection (cTBAD) with a lower mortality rate [6, 7]. In addition, the long-term follow-up data of acute cTBAD patients who have received TEVAR has shown that positive aortic remodeling happens in the stented section of the aorta [7, 8]. Moreover, the TEVAR cohort has been shown to have higher long-term survival rate than the OMT counterpart for patients with the subacute uTBAD [9]. Therefore, TEVAR has been proposed as an alternative therapy for acute uTBAD patients, to prevent later aneurysm formation and improve long-term outcomes. However, TEVAR has periprocedural risks of stroke, retrograde type A aortic dissection, and spinal cord ischemia, which is not ideal for patients at low risk for late complications [10]. Therefore the prognostic factors for late complication are necessary to indicate the needs of early TEVAR for patients with the acute uTBAD.

1.2 Current State of the Computational Study on Aortic Dissections

Ideally, anatomic risk factors could be identified based upon the non-invasive medical imaging at the initial diagnosis of acute uTBAD to predict if a patient would develop complications in the chronic phase. Previous investigations have identified anatomic criteria (e.g., the maximal thoracic aortic diameter, FL expansion rate, size and location of the entry tear) that are potential risk factors for the FL dilation and subsequent rupture [11, 12, 13, 14, 15]. However, there is a high individual variability in the results of these studies that limits their predictive value. Furthermore, the morphological evolution of the FL is three dimensional and complex, therefore measures such as localized diameters cannot fully represent the

global changes. Collectively, these issues require advanced image-based analyses. Moreover, identifying a set of criteria solely based on the morphology of the FL leaves an incomplete picture. For example, controversy also exists on the impact of FL thrombosis upon aneurysm formation and mortality [16, 9, 12, 17].

Patient-specific Computational Fluid Dynamics (CFD) simulations provide spatial and temporal hemodynamic quantities that facilitate the understanding of this disease progression [18]. The impact of hemodynamics on FL degeneration has been studied using CFD simulations. The effect of Wall Shear Stress (WSS) related factors, the percentage of blood flow passing through the FL, the pressure difference between TL and FL, and also the Relative Residence Time (RRT) of flow inside of the FL have been studied [19, 20, 21, 22, 23, 24]. However, when relating the hemodynamic factors with the FL evolution, these studies characterized the degeneration of the FL by localized measurements such as the change of the maximum aortic diameter. Observational conclusions were drawn, generally on one patient, possibly with a follow-up [20]. A systematic aggregation of all hemodynamic factors and how they correlate to this disease progression is still missing.

1.3 Challenges

1.3.1 3D quantification of the aneurysmal degeneration

To obtain reliable conclusions that could eventually provide clinically relevant indications, systematic quantitative analyses of the disease progression need to be performed in a reproducible way on the longitudinal patients' data, with a 3D quantification of the FL degeneration based on objective tools of the non-rigid image registration.

1.3.2 Efficient modeling of the incompressible flow with moderate large Reynolds numbers

Patient-specific computational studies over a large number of patients enrolled in longitudinal clinical trials are needed. Consequently, an efficient and accurate modeling of the hemodynamics in complex geometries with moderate large Reynolds numbers is indispensable.

The blood flow in the aorta at systolic peak is at the transitional stage to turbulence. Strong convective fields in specific geometrical configurations, like the dissected aorta, determine an energy cascade from the flow structure of large scales to small scales. Therefore, very fine discretizations are required to capture all the relevant scales of the dynamics of interest, i.e. Direct Numerical Simulation (DNS). For time-sensitive clinical studies involving a large cohort of patients, the computational costs required by DNS may be intimidatingly high. Therefore, turbulence modeling has been adopted in simulating hemodynamics in aorta [25]. Large Eddy Simulation (LES) is preferred to the classical Reynolds Average Navier Stokes (RANS) approach for flow with moderate Reynolds numbers ($Re < 10^4$) as it allows a better control of the approximation error.

The Leray model [26] was originally proposed by Jean Leray at 1934 as a regularization for the incompressible Navier-Stokes equations. Around early 2000s, the model was studied by Edriss Titi, Darryl Holm and their colleges as a LES model [27, 28]. In general, the model captures the small scales by an auxiliary differential problem ("filter") coupled with the Navier-Stokes equations. The original proposed filter was a Gaussian filter. Later the deconvolution filter was proposed by William Layton and his colleges to replace the Gaussian filter in the model to improve the computational efficiency and accuracy [29, 30, 31]. Since then, the deconvolution-based Leray model solved by evolve-filter-relax decoupling scheme (Leray-EFR) has shown a great potential in reducing computational cost in modeling turbulent flows, e.g. in the Food and Drug Administration benchmark nozzle problem [32]. Therefore, in aortic flow applications, the model could facilitate the reduction of the computational cost, while serving as a strong consistent stabilization for the numerical instabilities due to the strong convection during systole.

1.3.3 Defective boundary conditions

In simulations of the blood flow in aortas, the governing equations are approximated in a truncated domain (i.e. the location of interest) involving only the large arteries recon-

structed from patients' medical images, due to the constraint of the computational feasibility. Boundary conditions at the artificial boundaries of the truncated domain are in need to represent the downstream vasculature and therefore are of great importance for obtaining the physiological solution [33, 18, 34, 35, 36, 37]. However, practical and ethical constraints limit the access to the data to be used for a full patient-specific prescription of the boundary conditions required for the numerical simulations.

As the patient-specific velocity fields at the exact boundaries are rarely available, Neumann boundary conditions are widely adopted with traction or pressure data that are often derived from 1D or 0D surrogate models leveraged by patients' data [35, 38, 39, 37, 40]. The circumstance that boundary data in computational hemodynamics are partially missing led to the concept of *"defective boundary conditions"*. In this circumstance, 1D and 0D model were often introduced to provide an educated estimate of missing data from measurements available in (accessible) vascular districts peripheral to the one of interest. Data assimilation procedures could be adopted [41, 35, 19]. The assimilation process is regarded as a minimization procedure of the mismatch between the computed and the limited measured boundary data. This automatically provides an "optimal" enforcement of the available data, a versatile general approach for any kind of concerns and a natural management of noise and errors in the data, since the conditions are enforced in a "least square" sense. The strong concern of this approach is the computational costs. As the problem is resolved in a constrained minimization with many parameters, the computational costs may rapidly increase - at the bottom line, the governing equations must be solved several times at each time step. For this reason, keeping in mind the general "exact" data assimilation approach, practical solutions are proposed that preserve the "optimal" enforcement in an approximate way that preserves the computational efficiency [37].

However, in most retrospective study, no boundary data is available at all. It's the co-called "image-legacy" problem, i.e. as the patients' images are routinely acquired and stored and imaging processing tools can guarantee nowadays a trustworthy description of

the geometry, either the relevant pressure or flow data are not recorded. In this situation, the missing data are usually replaced by modeling assumptions (e.g. zero pressure at outflow branches) [22] or by adapting literature data to the case of interest [20, 23, 24], which could be far from ideal, and sometimes leading to nonphysical results.

1.3.4 Backflow instability

When the Neumann boundary conditions are commonly enforced at aortic branches due to lack of the patient-specific velocity data [35, 38, 39, 37, 40], a well known numerical instability called *backflow instability* potentially occurs. In the relative large aortic branches, i.e. the supra aortic branches and renal artery, the retrograde flows, namely backflow, might present during late systole and early diastole when the blood flow is decelerating. These backflows on the Neumann Boundaries induce numerical instability due to the energy injection caused by the convection term even with Reynolds numbers of hundreds, which is the so-called *backflow instability*. There have been various study on stabilizing the backflow instability with velocity-based, velocity gradient-based and other formulations [42, 43, 44, 45]. Many of these contributions rely on the modification of the Neumann boundary conditions to damp flow reversal, following the ideas of [46], yet stemming from a different motivation.

1.3.5 Uncertainty in predictions of clinical quantities of interest

In addition to ensure the numerical stability and accuracy, it is crucial to understand the uncertainty involved in the simulations and their impact on the clinical quantities we ultimately care about, i.e. the model *predictions*. The global sensitivity analysis, which reflects the overall sensitivity properties across the entire inputs' domain, quantifies the importance of each uncertain inputs with respect to the predictive uncertainty of the given Quantity of Interest (QoI).

Uncertainty in patients' data

Generally, various sources of uncertainty are present in patient-specific simulations, either due to the lack of patients' data, measurement errors, or intrinsic variations of the physiological parameters. Uncertainty quantification considering patients' data has attracted substantial attention recently years [47, 48, 49, 50, 51, 52, 53, 54, 55, 56].

Boundary conditions have a crucial effect on the reliability of the predicted clinical QoI. However, the complete data set on patient-specific boundary conditions either are not available or contain measurement noises. There have been study investigating the impact of uncertainty of inflow and outflow boundary conditions on simulation results of blood flows [47, 48, 49, 50, 51, 52, 56]. The arterial morphology also has a significant influence on the hemodynamic prediction, especially considering the evolution of the arterial wall as the progression of the disease [51, 53, 54]. The variations has to be considered to seek the disease-relevant hemodynamic factors. There are also other uncertainties affecting the clinical QoIs, such as parameters of material constitutive model of the arterial wall and the rheology of the blood [55, 56, 51].

Uncertainty in the model parameter

In addition to uncertainty in patients' data, the prediction of the complex fluid flow of large Reynolds numbers using turbulence modeling exhibits model-form uncertainties, which originate from the closure model and discrepancy in time-scale. It is crucial not only to acknowledge and but also to quantify the influence of the model parameters on the model predictions. At the state of art, several attempts of investigating the model-form uncertainty in turbulence modeling are made, such as physics-based Bayesian framework for the stress closure in the RANS model [57, 58, 59, 60, 61], Bayesian calibration of the closure coefficient in $\kappa - \epsilon$ models [62, 63], and etc.

Similar as other turbulence models, Leray model has problem-dependent parameters prescribed by users, among which the filter radius is a key parameter to the effectiveness

of this model. The filter radius dictates the regularization of the convection velocity field, which drives the energy norm of the model error [29]. There have been some numerical evidence and analysis results showing that an appropriate and effective choice could be the minimum mesh size h_{min} [32]. Moreover, a local sensitivity analysis [64] study on this specific model with respect to fixed nominal values of the filter radius [65] has been conducted. However, a global sensitivity analysis is in need to explore the complete parameter space, specifically for the hemodynamic applications, to investigate the influence of the choice of the filter radius on the simulation results comparing to other hemodynamic parameters.

1.4 Objectives

Despite of a significant amount of research that has been conducted to better understand correlations between the hemodynamic quantities and the false lumen aneurysmal degeneration and therefore the prognostic factors for the disease progression for type B aortic dissection, most of the challenges mentioned above remain unresolved, which prohibits more conclusive clinical-relevant results.

The goal of this thesis, therefore, is to contribute to the search of the prognostic factors for the false lumen degeneration by addressing these challenges, i.e. investigating the efficiency of a LES model (the deconvolution-based Leray mode) in aortic simulations and its potential for the backflow stabilization; analyzing model uncertainty and other forms of uncertainty involved in the patient-specific simulations to quantify the confidence in model predictions; applying the model to simulating the hemodynamics of type B aortic dissections and correlate the hemodynamic factors with the 3D false lumen degeneration quantified by a registration method.

The specific aims are:

- Aim 1. Development, implementation and deployment of the deconvolution-based Leray model using the Finite Element Method.

- Aim 2. Analysis of using the Leray model for suppressing the backflow instability, a common numerical instability in hemodynamic simulations.

- Aim 3. Sensitivity analysis and uncertainty quantification of the effect of the Leray model parameter and patients' data on clinical quantities of interest, therefore quantifying the robustness of the model.

- Aim 4. Investigation of the hemodynamic indication factors of early surgical intervention for the acute uncomplicated type B aortic dissection by correlating the hemodynamic factors and 3D false lumen degeneration quantified by a registration method.

The insights gained from this research will provide a thorough understanding of not only the general efficacy, but also the parameters' choice for the deconvolution-based Leray model in hemodynamics applications. Moreover, the combined CFD and imaging process of longitudinal dataset may be a valuable tool to predict which patients with complicated TBAD will develop late complication requiring surgical intervention, by elucidating the interplay between geometry and hemodynamics relevant for the pathology. These methods proposed here are likely applicable to study other aortic disease with large cohort of patients, e.g. aortic aneurysms, that could enable us to reach our ultimate goal of developing predictive algorithms based on these methodologies.

1.5 Thesis Outline

A detailed description on the main methods involved in this thesis is provided in Chapter 2. Firstly, the model under investigation, i.e. the deconvolution-based Leray model, is introduced, as well as the numerical methods used to solve the model. Secondly, the methods adopted in the global sensitivity analysis and uncertainty quantification (Aim 3), specifically details on the Polynomial Chaos Expansion and Sobol' index, are provided. Several methodological details involved in the patient-specific study (Aim 4) are then given, including imaging reconstruction and registration, patient-specific boundary conditions and the mathematical definitions of the hemodynamic quantities discussed in this thesis.

The investigation of the deconvolution-based Leray model starts with the analysis on its potential in stabilizing the backflow instability (Aim 3), as detailed in Chapter 3. Specifically, a theorem is proposed and proved rigorously based on the energy analysis. The numerical evidence that corroborates the theory on both idealized and realistic cases are also provided. The realistic case is a patient-specific simulation of the hemodynamics in an aorta with the abdominal aortic aneurysm.

Uncertainties affect the reliability of the numerical simulation of hemodynamics in patient-specific settings and rigorous uncertainty quantification is presented in Chapter 4 (Aim 3). This Chapter presents an uncertainty quantification study on the aorta flow, for assessing the sensitivity of the clinical relevant quantities to the morphology and imprecise knowledge of the boundary condition using the Polynomial Chaos Expansion based Sobol' indices. Specifically, we focused on (i) the variation of the geometry of the patient-specific aorta reconstructed from medical images; (ii) the inflow boundary condition. In addition to the uncertainty in patients' data, the influence of the problem-dependent parameter in the Leray model, i.e. the filter radius, is also investigated. The sensitivity of the total kinetic energy , the time average wall shear stress and the oscillatory shear index are analyzed.

Chapter 5 focuses on the patient-specific study of the uncomplicated type B aortic dis-

section by applying the deconvolution-based Leray model to hemodynamic simulations and investigating its potential prognostic factors for the late false lumen degeneration. This Chapter first focuses on a single patient with a longitudinal imaging data for a comprehensive correlation analysis between morphological and functional (hemodynamics) factors. Then a cross-sectional study involves multiple patients are carried out for a further investigation.

The large eddy simulation model, the deconvolution-based Leray model, investigated in this thesis are implemented in both C++ and Python, based on two parallel Finite Element libraries. The implementations are detailed in Chapter 6.

Lastly, major conclusions are drawn from the research work in Chapter 7. Future plans as the continuation of current research are also discussed in this Chapter.

CHAPTER 2

METHODS

2.1 The Deconvolution-based Leray-EFR Model

2.1.1 The incompressible Navier-Stokes Equations

In this thesis, the blood in aortas is assumed to be the incompressible, isothermal and Newtonian fluid, with density $\rho = 1.06\,\mathrm{g/cm^3}$ and dynamic viscosity $\mu = 0.035\,\mathrm{dyn}\cdot\mathrm{s/cm^2}$. Also, the aortic wall is assumed to be rigid therefore no fluid-structure interaction modeling. As this may be considered a cruel approximation in aortic domains, the inclusion of a deformable arterial wall, dictated by the constitutive model of the tissue, calls for very expensive numerical procedures. The possible gain in accuracy is questioned by a lack of substantial knowledge, quantitatively and also qualitatively, of the constitutive laws in pathological tissues. The rigid-assumption is, in fact, shared by most of the literature in this field, with the exception of some work on idealized geometries [66].

Under these assumptions, the appropriate mathematical model of the blood flow is given by the incompressible Navier-Stokes equations (INSE), which reads: in $\Omega \times (0,T)$

$$\rho\frac{\partial \mathbf{u}}{\partial t} + \rho\left(\mathbf{u}\cdot\nabla\right)\mathbf{u} - 2\mu\Delta^s\mathbf{u} + \nabla p = \mathbf{0}, \tag{2.1}$$

$$\nabla\cdot\mathbf{u} = 0, \tag{2.2}$$

with the boundary and initial conditions

$$\mathbf{u} = \mathbf{u}_D \ \text{ on } \ \Gamma_D \times (0,T)\,, \tag{2.3}$$

$$(\mu\nabla\mathbf{u} - p\mathbf{I})\mathbf{n} = \mathbf{g} \ \text{ on } \ \Gamma_N \times (0,T)\,, \tag{2.4}$$

$$\mathbf{u}(t=0) = \mathbf{u}^0 \ \text{ in } \ \Omega, \tag{2.5}$$

where $\mathbf{u}$ denotes the blood velocity and p is the pressure. These equations are completed by corresponding initial and boundary conditions. The operators ∇^s and Δ^s are defined as

$$\nabla^s \mathbf{u} \equiv \frac{1}{2}(\nabla \mathbf{u} + \nabla \mathbf{u}^T), \qquad \Delta^s \mathbf{u} \equiv \nabla \cdot (\nabla^s \mathbf{u}) \tag{2.6}$$

where ∇^s is the symmetric part of the gradient.

As well known, when the Reynolds number of the fluid increases past a certain threshold, the nonlinear convective term determines an energy cascade from large to small space scales. These dynamics challenge the numerical simulation, as the reticulation for the spatial discretization must adjust to properly describe the small-scale energy. The scale at which we can consider the energy to be dissipated is given by the Kolmogorov theory [67] as

$$\eta \approx \left(\frac{\mu^3 L}{\rho^3 U^3} \right)^{1/4} \approx L Re^{-3/4}$$

where L is a characteristic length of the problem, U the maximum velocity magnitude, and Re the Reynolds number. A possible approach to overcome the burden of exceedingly fine meshes is to resort to LES modeling. Generically speaking, LES incorporates the effect of small under-resolved space scales - i.e. in the range between η and the size of the mesh h (with $\eta < h$) - by an appropriate average-based approximation of their effect on the resolved scales. This general idea can be realized in different ways [68, 28, 69, 70].

2.1.2 The deconvolution-based Leray-EFR model

To avoid the curse of high Re and with the perspective of setting up an efficient CFD solver for a large number of patients, we follow an approach developed by W. Layton, L. Rebholz and collaborators [31, 29, 71, 72], where the unresolved scales are incorporated into the simulation by a differential operator acting as a filter, triggered by an appropriate indicator function that identifies where and when we actually have unresolved scales.

The model reads: in $\Omega \times (0, T)$

$$\rho \frac{\partial \mathbf{u}}{\partial t} + \rho \left(\mathbf{u}_f \cdot \nabla \right) \mathbf{u} - 2\mu \Delta^s \mathbf{u} + \nabla p = \mathbf{0}, \tag{2.7}$$

$$\nabla \cdot \mathbf{u} = 0, \tag{2.8}$$

$$-2\delta^2 \nabla \cdot (a(\mathbf{u}) \nabla^s \mathbf{u}_f) + \mathbf{u}_f + \nabla p_f = \mathbf{u}, \tag{2.9}$$

$$\nabla \cdot \mathbf{u}_f = 0; \tag{2.10}$$

with the boundary and initialconditions:

$$\mathbf{u} = \mathbf{u}_f = \mathbf{u}_D \ \text{ on } \ \Gamma_D \times (0, T)\,, \tag{2.11}$$

$$(\mu \nabla \mathbf{u} - p\mathbf{I})\mathbf{n} = \mathbf{g} \ \text{ on } \ \Gamma_N \times (0, T)\,, \tag{2.12}$$

$$(\delta^2 a(\mathbf{u}) \nabla \mathbf{u}_f - p_f \mathbf{I})\mathbf{n} = \mathbf{0} \ \text{ on } \ \Gamma_N \times (0, T)\,; \tag{2.13}$$

$$\mathbf{u}(t = 0) = \mathbf{u}^0 \ \text{ in } \ \Omega. \tag{2.14}$$

Here, $\mathbf{u}$ and p denotes the velocity and pressure at the resolved scales, respectively. ρ is the density and μ is the dynamic viscosity. The equation (2.7) is a variation of the momentum equation (2.1) in the INSE. The convection field is replaced by $\mathbf{u}_f$, which is the filtered velocity. The filtered velocity $\mathbf{u}_f$ is obtained by the nonlinear filter (the equations (2.9)-(2.10)) applied to the velocity at the resolved scales $\mathbf{u}$. The filter takes into account of the flow field at the unresolved scales using the flow at the resolved scales within a spatial range δ, where δ is called the filter radius. p_f is commonly known as the filtered pressure field, which enforces the incompressibility of the filtered velocity.

The scalar functional $a(\mathbf{u}) = |\mathbf{u} - D(F(\mathbf{u}))| \geq 0$ is the deconvolution based indicator function with F being the linear Helmholtz filter and D representing the Van Cittert deconvolution operator [32]. The indicator function detects the intensity of the flow at the unresolved scales and controls the on/off of the differential filter (2.9)-(2.10). $a(\mathbf{u}) \simeq 0$ when there is no unresolved flow needs to be modeled and $a(\mathbf{u}) \simeq 1$ when the unresolved

velocity is strong and the filter is needed. The role of the indicator function is to detect the regions of disturbed flow.

Evolve-Filter-Relax scheme

For the numerical approximation, system (2.7)-(2.10) requires time and space discretizations. The time discretization can be carried out by a collocation finite-difference approach. Let the time step be Δt (uniform) and the problem in the instants $t^n \equiv n\Delta t$, for $n = 1, \ldots, N_T$, and $T = N_T \Delta t$. The time-derivative is then approximated by finite differences involving the unknowns in these collocation points. A Backward Differentiation Formula of order p (BDFp) is adopted, see e.g. [73]. The Leray system (2.7)-(2.10) discretized in time reads: given $\mathbf{u}^0$, for $n \geq 0$ find the solution $(\mathbf{u}^{n+1}, p^{n+1}, \mathbf{u}_f^{n+1}, p_f^{n+1})$ of the system:

$$\rho \frac{\alpha}{\Delta t} \mathbf{u}^{n+1} + \rho(\mathbf{u}_f^{n+1} \cdot \nabla)\mathbf{u}^{n+1} - 2\mu \Delta^s \mathbf{u}^{n+1} + \nabla p^{n+1} = \mathbf{b}^{n+1}, \tag{2.15}$$

$$\nabla \cdot \mathbf{u}^{n+1} = 0, \tag{2.16}$$

$$-2\delta^2 \nabla \cdot \left(a(\mathbf{u}^{n+1}) \nabla^s \mathbf{u}_f^{n+1}\right) + \mathbf{u}_f^{n+1} + \nabla p_f^{n+1} = \mathbf{u}^{n+1}, \tag{2.17}$$

$$\nabla \cdot \mathbf{u}_f^{n+1} = 0, \tag{2.18}$$

where α is a coefficient that depends on the order of BDF chosen, and $\mathbf{b}^{n+1}$ contains the forcing term $\mathbf{f}^{n+1}$ and the solution at the previous time steps used to approximate the time derivative of $\mathbf{u}$ at time t^{n+1}. For example,

$$\text{BDF1}: \begin{cases} \partial_t \mathbf{u} \simeq \dfrac{1}{\Delta t}\left(\mathbf{u}^{n+1} - \mathbf{u}^n\right) \\ \alpha = 1 \\ \mathbf{b}^{n+1} = \mathbf{f}^{n+1} + \dfrac{1}{\Delta t}\mathbf{u}^n \end{cases}, \text{BDF2}: \begin{cases} \partial_t \mathbf{u} \simeq \dfrac{1}{2\Delta t}\left(3\mathbf{u}^{n+1} - 4\mathbf{u}^n + \mathbf{u}^{n-1}\right) \\ \alpha = 3/2 \\ \mathbf{b}^{n+1} = \mathbf{f}^{n+1} + \dfrac{1}{2\Delta t}\left(4\mathbf{u}^n - \mathbf{u}^{n-1}\right) \end{cases}. \tag{2.19}$$

The semi-discretized system (2.15)-(2.18) can be efficiently implemented in the so-called *Evolve-Filter-Relax* scheme.

Evolve: solve $(\mathbf{v}^{n+1}, q^{n+1})$,

$$\rho\frac{\alpha}{\Delta t}\mathbf{v}^{n+1} + \rho\left(\mathbf{u}^{*}\cdot\nabla\right)\mathbf{v}^{n+1} - \mu\Delta\mathbf{v}^{n+1} + \nabla q^{n+1} = \mathbf{b}^{n+1}, \tag{2.20}$$

$$\nabla\cdot\mathbf{v}^{n+1} = 0. \tag{2.21}$$

Filter: solve $(\mathbf{v}_f^{n+1}, \lambda^{n+1})$,

$$-\delta^2\nabla\cdot\left[a(\mathbf{v}^{n+1})\nabla\mathbf{v}_f^{n+1}\right] + \mathbf{v}_f^{n+1} + \nabla\lambda^{n+1} = \mathbf{v}^{n+1}, \tag{2.22}$$

$$\nabla\cdot\mathbf{v}_f^{n+1} = 0. \tag{2.23}$$

Relax: $(\mathbf{u}^{n+1}, p^{n+1})$,

$$\mathbf{u}^{n+1} = (1-\chi)\mathbf{v}^{n+1} + \chi\mathbf{v}_f^{n+1}, \tag{2.24}$$

$$p^{n+1} = q^{n+1} + \alpha\chi\lambda^{n+1}. \tag{2.25}$$

The convection term in (2.20) is treated semi-implicitly with the convection field being a second order extrapolation from previous time steps, $\mathbf{u}^{*} = 2\mathbf{u}^{n} - \mathbf{u}^{n-1}$. $\chi \in [0,1]$ here is the relaxation parameter and $\chi = O(\triangle t)$ to aviod over dissipation [72].

For the space discretization, the Finite Element method with the inf-sup stable Taylor-Hood elements ($\mathbb{P}_2/\mathbb{P}_1$ or $\mathbb{P}_1 -$ Bubble$/\mathbb{P}_1$) are adopted [74]. For solving the resulting linear systems associated with the two saddle point problem, namely the evolve and filter steps, the Yosida splitting method is adopted [75].

2.2 Uncertainty Quantification and Sensitivity Analysis

In addition to the deterministic patient-specific simulations, uncertain quantification and global sensitivity analysis are conducted to analyze the robustness of the Leray-EFR model and the effect of uncertainty in the clinical relevant quantity of interest, for the purpose of investigating the confidence in the model predictions. Global sensitivity analysis quantifies the importance of each uncertain inputs with respect to the predictive uncertainty of the given QoIs by exploring the entire input parameters' domain [76]. Traditionally, a comprehensive global sensitivity study of the model parameter in patient-specific applications has been prohibitive due to the high computational expanse of the Monte Carlo (MC) method. MC approaches generally requires many samples, since the accuracy improves with only the square root of the number of samples. In this thesis, therefore, Polynomial Chaos Expansion (PCE) is adopted as a surrogate model to compute the statistical moments. The uncertainty in the filter radius δ, inflow boundary condition and morphology in aorta are considered and propagated using the truncated PCE. Furthermore, in order to quantify the effect of each uncertain input, the Sobol' indices of the uncertain inputs with respect to the output QoI are computed and investigated. The notations in this section follow the previous study [77, 65, 78].

2.2.1 The Sobol' index

A variance-based sensitivity index, the Sobol' index [79], is adopted in this work to characterize the dependence of the output variance on the uncertain inputs, and therefore rank the influence of the inputs, especially for non-linear models [77, 65, 80]. Sobol proved that the output of a model can be decomposed into summands with increasing dimensions of the input parameters [79]. Let $\boldsymbol{\xi} = (\xi_1, ..., \xi_d)$ represents the the vector of d dimensional inputs, which are independent random variables with a joint distribution $\pi(\boldsymbol{\xi})$ defined on the sample space Ω of a probability measure space $(\Omega, \mathcal{F}, P)$, where P is the probability

measure defined on the sigma-algebra $\mathcal{F}$. The Sobol' decomposition [81] of the model output reads

$$
\begin{aligned}
f(\boldsymbol{\xi}) &= f_0 + \sum_{i=1}^{d} f_i(\xi_i) + \sum_{1 \le i < j \le d} f_{ij}(\xi_i, \xi_j) + ... \\
&+ f_{1,...,d}(\xi_1, ..., \xi_d) \\
&= f_0 + \sum_{1 \le i_1 < ... < i_s \le d} f_{i_1,...,i_s}(\xi_{i_1}, ...\xi_{i_s})
\end{aligned}
\tag{2.26}
$$

for $s = 1, ..., d$, where all summands depend on time t and spatial variables $\mathbf{x}$. Keep in mind that f here represents a generic QoI such as the TAWSS or OSI. To further simplify the decomposition, assume the index sets $A = \{i_1, ..., i_s\} \subset \{1, ..., d\}$ for $s = 1, ..., d$, the decomposition (2.26) can be written as

$$
f(\boldsymbol{\xi}) = \sum_{A \subset \{1,...,d\}} f_A(\boldsymbol{\xi}_A) \tag{2.27}
$$

with $f_\emptyset \coloneqq f_0$, $\boldsymbol{\xi}_A = (\xi_{i_1}, ..., \xi_{i_s})$. The summands satisfy

$$
\int f_A(\boldsymbol{\xi}_A)\pi(\xi_i)d\xi_i = 0, \quad \forall i \in A, \tag{2.28}
$$

by the construction of the decomposition. Therefore the orthogonality between the summands follows as

$$
\int f_A(\boldsymbol{\xi}_A) f_B(\boldsymbol{\xi}_B)\pi(\boldsymbol{\xi})d\boldsymbol{\xi} \tag{2.29}
$$

$$
= \delta_{AB} \int f_A(\boldsymbol{\xi}_A) f_A(\boldsymbol{\xi}_A)\pi(\boldsymbol{\xi})d\boldsymbol{\xi}, \tag{2.30}
$$

$$
\forall A, B \subset \{1, ..., d\} \tag{2.31}
$$

where δ_{AB} is the Kronecker delta ($\delta_{AB} = 1$ for $A \equiv B$; $\delta_{AB} = 0$ otherwise).

Due to the orthogonality, the total and partial expectation of output are simply

$$\mathbb{E}(f) = \int f(\boldsymbol{\xi})\pi(\boldsymbol{\xi})d\boldsymbol{\xi} = f_0 \tag{2.32}$$

$$\mathbb{E}(f_A) = \int f_A(\boldsymbol{\xi}_A)\pi(\boldsymbol{\xi}_A)d\boldsymbol{\xi}_A = 0 \tag{2.33}$$

The total variance and partial variance are defined as

$$\begin{aligned} V &:= \text{Var}[f] = \mathbb{E}(f^2 - \mathbb{E}(f)^2) \\ &= \int f(\boldsymbol{\xi})^2\pi(\boldsymbol{\xi})d\boldsymbol{\xi} - f_0^2, \end{aligned} \tag{2.34}$$

$$\begin{aligned} V_A &:= \text{Var}[f_A] = \mathbb{E}(f_A^2 - \mathbb{E}(f_A)^2) \\ &= \int f_A^2(\boldsymbol{\xi}_A)\pi(\boldsymbol{\xi}_A)d\boldsymbol{\xi}_A. \end{aligned} \tag{2.35}$$

Subsequently, the Sobol' indices [81] corresponding the specific set A of inputs are defined as the ratios between the partial variances and the total variance

$$S_A = V_A/V \tag{2.36}$$

which are the global sensitivity indices indicating the functional structure of the model [81] related to the combination of the input parameters $\boldsymbol{\xi}_A$. Notice that $f_A = 0$ if and only if $V_A = 0$.

2.2.2 Truncated polynomial chaos expansion

Considering the computational cost, truncated PCE is adopted in this thesis to computed the Sobol' indices. Any 2nd order random process (i.e. finite variance) can be represented as a series of polynomials in random inputs [82, 83]. Consider a set $\{\xi_i(\omega)\}_{i=1}^{\infty}$ of independent random variables with a joint distribution $\pi(\boldsymbol{\xi})$ defined on the sample space Ω of a probability measure space $(\Omega, \mathcal{F}, P)$, where P is the probability measure defined on the

sigma-algebra $\mathcal{F}$ as the previous section. The corresponding image probability space of the random variables is $(\Gamma, \mathcal{B}(\Gamma), \pi(\boldsymbol{\xi})d\boldsymbol{\xi})$, where Γ is the image of $\boldsymbol{\xi}$, $\mathcal{B}(\Gamma)$ is the Borel σ-algebra on Γ and $\pi(\boldsymbol{\xi})d\boldsymbol{\xi}$ is the probability measure defined on $\mathcal{B}(\Gamma)$. Consider

- $\mathbb{P}_p$ as the space of all polynomials in $\xi_i(\omega)$ with degree up to p;
- $\hat{\mathrm{P}}_p$ as the set of all polynomials in $\mathbb{P}_p$ orthogonal to $\mathbb{P}_{p-1}$ with respect to the probability measure $\pi(\boldsymbol{\xi})d\boldsymbol{\xi}$;
- $\overline{\mathbb{P}}_p$ as the space of polynomials spanned by $\hat{\mathrm{P}}_p$.

The subspace $\overline{\mathbb{P}}_p$ is called the pth homogeneous Chaos [84] originally and $\hat{\mathrm{P}}_p$ is called the Polynomial Chaos of order p. For $(t, \mathbf{x}) \in [0, T] \times \mathcal{D}$, a random process $u(t, \mathbf{x}, \boldsymbol{\xi})$ can be represented as

$$\begin{aligned} u(t, \mathbf{x}, \boldsymbol{\xi}) = u_0(t, \mathbf{x})\hat{\mathrm{P}}_0 &+ \sum_{i_1=1}^{\infty} u_{i_1}(t, \mathbf{x})\hat{\mathrm{P}}_1(\xi_{i_1}(\omega) \\ &+ \sum_{i_1=1}^{\infty}\sum_{i_2=1}^{i_1} u_{i_1 i_2}(t, \mathbf{x})\hat{\mathrm{P}}_2(\xi_{i_1}(\omega), \xi_{i_2}(\omega)) \\ &+ \sum_{i_1=1}^{\infty}\sum_{i_2=1}^{i_1}\sum_{i_3=1}^{i_2} u_{i_1 i_2 i_3}(t, \mathbf{x})\hat{\mathrm{P}}_3(\xi_{i_1}(\omega), \xi_{i_2}(\omega), \xi_{i_3}(\omega)) + ... \end{aligned} \tag{2.37}$$

with $u_{i_1 i_2 ...}(t, \mathbf{x})$ being the deterministic coefficients. This expansion can be re-written as

$$u(t, \mathbf{x}, \boldsymbol{\xi}) = \sum_{k=0}^{\infty} u_k(t, \mathbf{x})\Phi_k(\boldsymbol{\xi}) \tag{2.38}$$

where $\boldsymbol{\xi} = (\xi_1, \xi_2, ...)$. Clearly there is a one to one correspondence between the functionals $\hat{\mathrm{P}}_p$ and Φ_k. Therefore Φ_k are orthogonal polynomial basis with respect to probability

measure, i.e.

$$
\begin{aligned}
&< \Phi_i, \Phi_j > \\
&= \int \Phi_i(\boldsymbol{\xi})\Phi_j(\boldsymbol{\xi})\pi(\boldsymbol{\xi})d\boldsymbol{\xi} \\
&= \delta_{ij} \int \Phi_i(\boldsymbol{\xi})\Phi_i(\boldsymbol{\xi})\pi(\boldsymbol{\xi})d\boldsymbol{\xi} \\
&= \delta_{ij}||\Phi_i(\boldsymbol{\xi})||^2
\end{aligned}
\tag{2.39}
$$

where δ_{ij} is the Kronecker delta ($\delta_{ij} = 1$ for $i \equiv j$; $\delta_{ij} = 0$ otherwise). Φ_0 is conventionally taken as $\Phi_0 = 1$. Due to the orthogonality, the polynomial basis with degree greater than 0 has zero expectation.

In practice, only a finite set of d input parameters are considered with polynomial basis of limited degrees no greater than p. The truncated polynomial chaos expansion is

$$
u(t, \mathbf{x}, \boldsymbol{\xi}) = \sum_{k=0}^{K} u_k(t, \mathbf{x})\Phi_k(\boldsymbol{\xi}) \tag{2.40}
$$

where $K + 1 = \frac{(p+d)!}{p!d!}$.

The multivariate polynomial basis with degree up to p can be constructed by the tensor product of uni-dimensional basis

$$
\Phi_k(\boldsymbol{\xi}) = \Phi_{\boldsymbol{\alpha}^k}(\boldsymbol{\xi}) := \prod_{i=1}^{n} \phi_{a_i^k}(\xi_i) \tag{2.41}
$$

where $\boldsymbol{\alpha}^k = (\alpha_1^k, ..., \alpha_d^k) \in \mathbb{N}^n$ with $|\boldsymbol{\alpha}^k| = \sum_{i=1}^{n} \alpha_i^k \leq p$, $n \leq d$ and $k = 0, 1, ...K$. The moments of the output random process can be computed based on the PCE with minimum

computational effort. For a fixed $(t, \mathbf{x})$, the mean and variance of $u(t, \mathbf{x}, \boldsymbol{\xi})$ is given by

$$\mathbb{E}[u(t, \mathbf{x}, \boldsymbol{\xi})] \simeq u_0(t, \mathbf{x}) \tag{2.42}$$

$$Var[u(t, \mathbf{x}, \boldsymbol{\xi})] \simeq \sum_{k=1}^{K} u_k(t, \mathbf{x})^2 ||\Phi_k||^2 \tag{2.43}$$

2.2.3 PCE-based Sobol' indices

The summands of the Sobol's decomposition, depending only on the subset of parameters $\{\xi_1, ..., \xi_d\}$ indicated by the index set A, can be approximated using PCE as

$$f_A(t, \mathbf{x}, \boldsymbol{\xi}) \simeq f_A^{PC}(t, \mathbf{x}, \boldsymbol{\xi}) \tag{2.44}$$

In order to re-group the multidimensional polynomial basis $\Phi_{\boldsymbol{\alpha}}$ which depend only on a subset of parameters $A = \{i_1, ..., i_s\} \subset \{1, ..., d\}$ with $|A| := card(A)$, define the sets $I_A := \{k \in \{1, ..., K\} : \Phi_k = \prod_{i=1}^{|A|} \phi_{\alpha_i^k}(\boldsymbol{\xi}_{A_i}), \boldsymbol{\alpha}^k \in \mathbb{N}^d, |\boldsymbol{\alpha}^k| \leq p\}$. Therefore we have

$$f_A^{PC}(t, \mathbf{x}, \boldsymbol{\xi}_A) := \sum_{k \in I_A} f_k(t, \mathbf{x}) \Phi_k(\boldsymbol{\xi}_A) \tag{2.45}$$

where $f_k(t, \mathbf{x})$ is the deterministic coefficient.

Therefore the the Sobol' decomposition can be approximated by the truncated polynomial expansion as

$$\begin{aligned} f^{PC}(t, \mathbf{x}, \boldsymbol{\xi}) &\simeq \sum_{A \subset \{1, ..., d\}} f_A^{PC}(t, \mathbf{x}, \boldsymbol{\xi}_A) \\ &= \sum_{k \in I_A} f_k(t, \mathbf{x}) \Phi_k(\boldsymbol{\xi}_A) \end{aligned} \tag{2.46}$$

Due to the orthogonality of the polynomial basis, the total variance and partial variance can

be conveniently computed as

$$V^{PC} := \text{Var}[f^{PC}] = \sum_{k=1}^{K} y_k(t, \mathbf{x})^2 ||\Phi_k||^2 \tag{2.47}$$

$$V_A^{PC} := \text{Var}[f_A^{PC}] = \sum_{k \in I_A} y_k(t, \mathbf{x})^2 ||\Phi_k||^2 \tag{2.48}$$

Therefore, the PCE based Sobol' indices are

$$S_A^{PC} = V_A^{PC} / V^{PC} \tag{2.49}$$

Specifically, first-order Sobol' indices quantify the contribution of the total variance from the sole input parameter ξ_i

$$S_i^{PC} = \frac{\sum_{k \in I_{A_i}} f_k(t, \mathbf{x})^2 ||\Phi_k||^2}{\sum_{k=1}^{K} f_k(t, \mathbf{x})^2 ||\Phi_k||^2} \tag{2.50}$$

where $A_i = \{i\}$ for $i = 1, ..., d$. As shown in equation (2.50), the cost of computing the the Sobol' indices reduces to the cost of evaluating the coefficients in the truncated PCE.

2.2.4 Computing the coefficients of the polynomial chaos expansion

Intrusive (i.e. *Galerkin approach* [77, 85]) and *non-intrusive* (*point collocation* [86] and *pseudo-spectral projection*) methods [87, 86, 88] are used to compute the stochastic modes for the PCE. *Compressed sensing* is normally used together with the point collocation method to enforce the sparsity of the coefficients [89].

Considering the computational complexity of the application at hand and the dimension of the input parameter space, the *non-intrusive pseudo-spectral* method is adopted to estimate the coefficients of the truncated PCE due to its relatively low computational cost. By taking advantage of the orthogonality, the deterministic coefficients can be approximated

by the quadrature

$$f_k(t, \mathbf{x}) \simeq \frac{1}{||\Phi_k||^2} \sum_{r=1}^{R} f(t, \mathbf{x}, \boldsymbol{\xi}^r) \Phi_k(\boldsymbol{\xi}^r) \pi(\boldsymbol{\xi}^r) w^r \tag{2.51}$$

where $\boldsymbol{\xi}^r$ and w^r are quadrature points and associated weights. Nested sparse grid quadrature points based on Leja sequence [90] are adopted in this work and generated by Chaospy [91]. Note that the forward simulation is only evaluated at the quadrature points. For example, the number of forward simulations required for evaluating the stochastic modes for PCE of degree of two is 15 while it is 21 for PCE of degree of three, as shown in Fig. 4.4.

2.3 Patient-specific Study of Aortic Dissections

2.3.1 CT Angiography Acquisition and Imaging Reconstruction

The patient-specific CT images of aortas were performed at EUH with the intravenous injection of a contrast agent on a Siemens device. All DICOM slices were processed using the Vascular Modeling Toolkit (VMTK) [92] and 3D Slicer [93], open-source frameworks for image segmentation and geometric analysis. The geometry of the aortas were reconstructed by the state-of-the-art implicit deformable models and level-set tracking techniques [92]. The assumption for a contrast-enhanced acquisition is that the position of the vessel wall is at the locations of the maximum of the gradient of the image intensity. The region of interest is then obtained by solving an appropriate partial differential equation that detects this transition as the level set of the unknown. The final reconstructed models cover from the ascending aorta to the initial portion of the right and left common iliac arteries. The inclusion of aortic branches is dictated by the quality of the images.

2.3.2 Patient-specific Boundary Conditions

In the aortic geometries, the following portions are identified as boundaries.

- The arterial wall Γ_w

- The inflow Γ_{in}: the portion corresponding to the entrance of the blood flow, usually locates at the ascending aorta.

- The outflow Γ_{out}: one for each of the aortic branches (i.e. brachiocephalic trunk, left common carotid, left subclavian, superior mesenteric, renal arteries) and the common iliac arteries or the descending aorta.

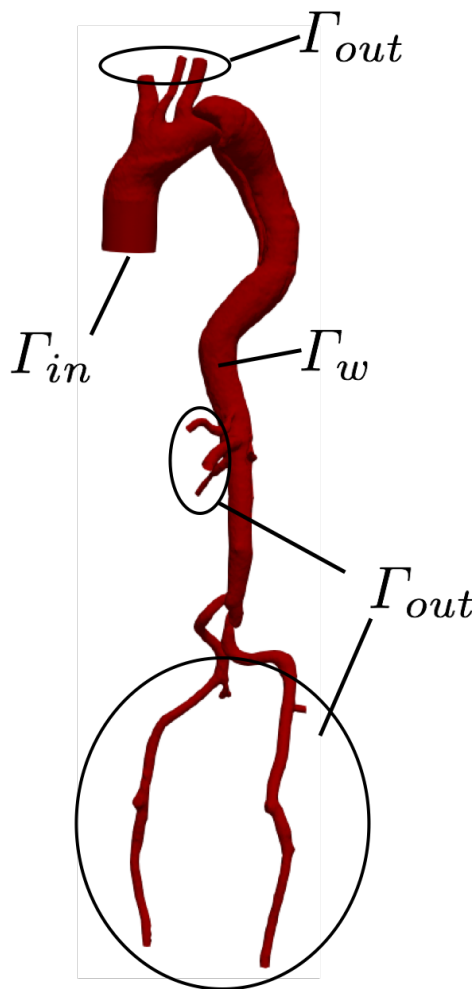

Figure 2.1: The boundaries of an aortic geometry.

An example is shown in Fig. 2.1. The aortic wall is assumed to be rigid and the non-slip condition leads to $\mathbf{u}(\Gamma_w, t) = \mathbf{0}, \forall t > 0$. At the inflow Γ_{in}, the flow rate from a previous study [94] is adopted with the flat velocity profile, due to the lack of patient-specific data. It is more difficult to adapt literature data for the outflow sections Γ_{out} , due

to the more significant individual variations of the arterial branches. As the geometry is the only patient-specific data available, a surrogate modeling strategy is developed in this study to convert morphological information into boundary data, by utilizing the Murray's law and the Three-Element Windkessel (3WK) model.

The Murray's law, defining the flow rate entering an branch based on the vessel diameter d_b and the inlet diameter d_{in}, reads

$$\frac{Q_b}{Q_{in}} = \left(\frac{d_i}{d_{in}}\right)^s \tag{2.52}$$

where s is an empirical parameter in the range $[2, 3]$ [95, 96]. For non-circular sections the diameter is defined as the hydraulic diameter, e.g. $d_b = \sqrt{\frac{4A_b}{\pi}}$, $d_{in} = \sqrt{\frac{4A_{in}}{\pi}}$.

This condition could be converted into a velocity condition by assuming a velocity profile fitting to the given flow rate. However there are two downsides: one is that assumptions are required for the velocity profile. Secondly, mass conservation is not always guaranteed by Murray's law and the stress on one of the outflows needs to be assumed. These arbitrary assumptions are expected to have a significant impact on the final results [37].

To avoid these issues, we resort to the 3WK as a surrogate model for the Neumann boundary condition and calibrate its parameters by the flow splitting results from Murray's law. The 3WK model is a well-known lumped parameter description of the downstream circulation, that enforces the following pressure $P(t)$ and flow $Q(t)$ relation at the outflows

$$P(t) = R_1 Q(t) + P_p(0)e^{-t/(CR_2)} + \frac{e^{-t/(CR_2)}}{C}\int_0^t Q(\tau)e^{\tau/(CR_2)}d\tau, \tag{2.53}$$

where R_1 and R_2 represent the viscous resistance of the peripheral arteries, while C represents the compliance. $P_p(0)$ is the initial value of the distal pressure. The parameters are calibrated here based on the patient-specific flow splitting. This formula stems from a standard application of the integrating factor method. However, it is more practical to reformulate the problem in the frequency domain, via Fourier transform. Let us denote $\hat{P}(\omega)$

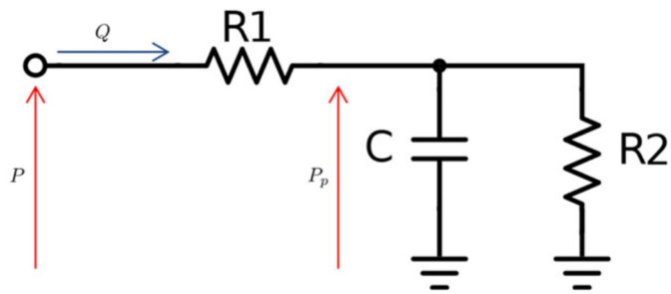

Figure 2.2: The Three Element Windkessel model.

and $\hat{Q}(\omega)$ as the Fourier transform of the pressure $P(t)$ and flow $Q(t)$.

Using the Fourier transform, we recall the impedance of the 3WK (see details in [18]) reads

$$Z_b(\omega) = \frac{\hat{P}(\omega)}{\hat{Q}(\omega)} = \frac{R_1 + R_2 + \omega^2 C^2 R_2^2 R_1}{1 + \omega^2 C^2 R_2^2} - j\frac{\omega^2 C R_{2,i}^2}{1 + \omega^2 C^2 R_2^2} \tag{2.54}$$

where $j = \sqrt{-1}$. Note that

$$|Z(\omega = 0)| = R_1 + R_2,\ |Z(\omega \to \infty)| = R_1 \tag{2.55}$$

with the angle frequency has an absolute minimum in

$$\omega_{min} = \sqrt{\frac{R_1 + R_2}{(CR_2)^2 R_1}} \tag{2.56}$$

Therefore, the 3WK parameters can be caliberated according to the following algorithm.

- A pressure waveform P_{avg}.
- For b^{th} outflow branch, the associated flow rate $Q_b(t)$ based the Murray's law with $s = 2$ [96] and the hydraulic diameters extracted from the patient images is computed. To maintain mass conservation, the flow in the right common iliac artery is computed as the difference between the inflow and the other flow rates.
- The impedance for b^{th} branch is computed as $Z_b(\omega)$.

- Finally, the parameters $R1$, $R2$, C are calibrated to match the landmark values of the impedance outlined above, leading to
  $R_1 = Z_b(\omega \to \infty)$, $R_2 = Z_b(\omega = 0) - R_1$, $C = \sqrt{\frac{R_1+R_2}{(\omega_{min}R_2)^2 R_1}}$.

These 3WK parameters are computed for each outflow to enforce the Neumann boundary condition using 3WK.

2.3.3 3D Quantification of Morphological Evolution using Registration

In order to quantify the degeneration of the aorta comprehensively, an non-rigid Point Set Registration (PSR) method based on the probability regression [97] is adopted to automatically co-register the initial and follow-up geometries. This method is capable of finding the non-rigid transformation between two geometries with soft assigning of the correspondence, without prior knowledge of the correspondence. It also utilizes a regularization based on filtering displacement field during the transformation to preserve the topological structures of the aorta.[1] In order to eliminate the influence of rigid body displacement, including translation and rotation, and capture the real aneurysm dilation, the initial and follow-up configurations were pre-aligned based on geometrical features before registration,

2.3.4 Definitions of clinical relevant hemodynamic quantities

The hemodynamic quantities in this thesis are computed as following.

The Wall Shear Stress (WSS) is defined as the tangential component of the normal stress. The normal stress for a Newtonian fluid is defined as

$$\mathbf{w} = p\mathbf{n} - \mu(\nabla\mathbf{u} + \nabla^T\mathbf{u}) \cdot \mathbf{n}$$

[1] The open source code offered by the research groups (https://sites.google.com/site/myronenko/research/cpd) facilitated the quick application of the registration method in this study.

and correspondingly the WSS reads

$$WSS \equiv \mathbf{w} - (\mathbf{w} \cdot \mathbf{n})\mathbf{n}.$$

The Time Averaged Wall Shear Stress (TAWSS) is defined as the time average over the heart beat of the WSS,

$$TAWSS = \frac{1}{T} \int_0^T WSS(t)dt.$$

The Oscillatory Shear Index (OSI) [98] is a way for measuring the occurrence of retrograde flows during the heart beat on the wall and it is defined as

$$OSI = \frac{1}{2}\left(1 - \frac{T \times |TAWSS|}{\int_0^T |WSS|dt}\right).$$

OSI of values around $\frac{1}{2}$ indicates a high occurrence of retrograde flows.

The Relative Residence Time (RRT) is defined as

$$RRT = \frac{1}{(1 - 2OSI)TAWSS}$$

is computed to assess the occurrence of stagnating regions of the blood flow, as a proxy for possible particle deposition.

CHAPTER 3

ANALYSIS OF THE LERAY-EFR MODEL

3.1 Motivation

In the numerical simulation of incompressible fluids, the occurrence of incoming flows through boundaries where Neumann conditions are prescribed may introduce numerical instability. This *backflow instability* is related to the nonlinear convective term and are often challenging the numerical simulation of blood flow in large vessels. In fact, the alternation of systole and diastole induces backflows at the outlets, which are usually Neumann boundaries since the lack of velocity data requires the prescription of traction/pressure conditions. The Reynolds numbers that produce backflow instability are generally moderate (above a few hundreds).

In this chapter, the Leray-EFR model is proved to be able to implicitly stabilize the backflow instability. This LES model uses deconvolution filters and is the basis of the so-called Evolve-Filter-Relax scheme recently introduced by Layton, Rebholz and their collaborators as an effective alternative to Direct Numerical Simulations for moderate or large Reynolds number flow [31, 99, 100]. The model is particularly attractive in computational clinical studies, where many cases need to be studied in a relatively short time. This Chapter shows that, with a judicious selection of the parameters of this LES scheme, it is possible to suppress the term that triggers the numerical backflow instability, so to obtain reliable and efficient numerical simulations. Aortic simulations feature Reynolds numbers and flow regimes that particularly benefit from this *serendipity* (aka 'two-birds-one-stone') circumstance.

A rigorous proof of our statement is carried out and so is numerical evidence that cor-

The work of Chapter 3 is published in Xu et al., Backflow Stabilization by Deconvolution-based Large Eddy Simulation Modeling. Journal of Computational Physics, 2019 (In press)

roborates the theory on both a idealized case and realistic one of a patient-specific aortic aneurysm geometry.

3.2 Theoretical Proof by Energy Analysis

3.2.1 The root of backflow instability

The occurrence of backflow instabilities can be explained by looking at the energy estimate for the Navier-Stokes equations (2.1)-(2.2). For the stability analysis, let us assume that all the Dirichlet and Neumann data as well as the forcing term are set to 0 so to consider the evolution of the solution to 0 from a generic initial condition $\mathbf{u}_0$. In what follows, we refer to the usual notation $L^2(\Omega)$ for functions with square integrable according to Lebesgue. We do not introduce a different notation for scalar or vector functions as it will be clear from the context. Also, functions with s distributional derivatives in $L^2(\Omega)$ will be denoted with the usual notation for Sobolev spaces $H^s(\Omega)$. As usual, $(\cdot,\cdot)$ denotes the scalar product in L^2 and $\|\cdot\|$ the associated norm. Following standard arguments, we multiply the momentum equation by the velocity $\mathbf{u}$ and the mass conservation by the pressure field p, we integrate on the space time domain $\Omega \times (0,T]$. Let us denote for the sake of brevity

$$E(T) \equiv \frac{\rho}{2}\|\mathbf{u}\|^2_{L^2}(T) + \mu \int_0^T \|\nabla^s \mathbf{u}\|^2_{L^2}(t)dt.$$

With a standard procedure, we get

$$E(T) + \frac{1}{2}\int_0^T \int_{\Gamma_N} |\mathbf{u}|^2 \mathbf{u}\cdot\mathbf{n} d\gamma dt \leq \|\mathbf{u}_0\|^2_{L^2} \equiv E(0).$$

Here, $\mathbf{n}$ is the outward normal unit vector. If $\mathbf{u}\cdot\mathbf{n} \geq 0$ for any $t > 0$, then the previous inequality does actually provide a stability estimate for the solution, as clearly we can conclude that $\|\mathbf{u}\|^2_{L^2}(T) \leq \|\mathbf{u}_0\|^2_{L^2}$ for any $T > 0$. This fails in the case of backflows, as *a priori* we may loose the control on the sign of $\int_0^T \int_{\Gamma_N} |\mathbf{u}|^2 \mathbf{u}\cdot\mathbf{n} d\gamma dt$ and eventually on the

bound for $E(T)$.

To fix this numerical problem grounded in the occurrence of physical flow reversal on Neumann boundaries, several remedies have been proposed, ranging from the introduction of flow extensions, or specific regions at the boundaries to damp the incoming energy [43], to the constraint of favorable velocity profiles by Lagrange multipliers [101], to the introduction of specific stabilization of the tangential components of the stress tensor [45, 44]. Benchmarks and comparisons among the different strategies have been considered in [102, 42].

A popular stabilization technique relies on the modification of the Neumann condition into a Robin one, with a resistance parameter R. This can be done in several ways [103, 46]. We specifically mention the excellent description in [43, 42]. For instance, in a simplified setting, in the strong form we can prescribe on $\Gamma_N \times (0, T)$

$$\left((\mu \nabla^s \mathbf{u} - \left(p - R \int_{\Gamma_N} \mathbf{u} \cdot \mathbf{n} d\gamma \right) \mathbf{I} \right) \mathbf{n} = g_N \mathbf{n} \tag{3.1}$$

corresponding to the introduction of a pressure drop in the direction of the flow weighted by the coefficient R. Specifically, with this term, the energy estimate (for $g_N = 0$) becomes

$$E(T) + \frac{1}{2} \int_0^T \int_{\Gamma_N} |\mathbf{u}|^2 \mathbf{u} \cdot \mathbf{n} d\gamma dt + R \int_0^T \left(\int_{\Gamma_N} \mathbf{u} \cdot \mathbf{n} d\gamma \right)^2 dt \leq \|\mathbf{u}_0\|_{L^2}^2 \equiv E(0).$$

For a proper calibration of the parameter R, the second and third terms on the left hand side are positive, to obtain the desired bound. This modifies the prescribed boundary conditions, with a damping as a sort lumped parameter modeling of a flow extension.

In the subsequent section, we prove that with our LES modeling there is no need of acting on the boundary conditions to obtain the bound on the discrete counterpart of $E(T)$ and eventually on the numerical solution.

3.2.2 Theoretical analysis

In this section, we establish the theoretical result showing that the numerical solution of our Leray-EFR scheme is bounded by the data for a judicious choice of the parameters δ and χ. We postulate some regularity for the domain and the data, so we can assume the velocity field to feature $H^3(\Omega)$ regularity in space. For simplicity, we refer our analysis to the regular Laplace operator as opposed to the symmetric one Δ^s, the extension to this case being a matter of technicalities. Also, we refer to the time discretization BDF1 (Implicit Euler) scheme, as this is an unconditionally stable method, with no limitations on the time step to achieve stability. We argue (and demonstrate numerically) that the analysis can be extended to high order time discretizations, with the possible limitations on the time step required by the time advancing method.

THEOREM

Assume that the data of the problem at hand are regular enough s.t. $\mathbf{u} \in L^2(0, T, H^3(\Omega))$. Also, assume that the problem has homogeneous boundary conditions ($\mathbf{u}_D = 0$ on Γ_D and $g_N = 0$ on Γ_N) and a null forcing term $\mathbf{f}$. For $\chi \to 1$ and a suitable choice of the filter radius δ, the Leray-EFR scheme features a solution such that for any $n > 0$

$$\|\mathbf{u}^n\|_{L^2} \leq \|\mathbf{u}_0\|_{L^2}. \tag{3.2}$$

$\triangle$

The condition (3.2) actually means that the backflow instabilities cannot occur, as we will demonstrate numerically.

PROOF

We restart from the reinterpretation of the method as a perturbation of the Navier-Stokes equations (see [32]), with BDF1 time discretization ($\alpha = 1$), homogeneous boundary data

and $\mathbf{f} = \mathbf{0}$:

$$\begin{aligned}&\tfrac{\rho}{\Delta t}\mathbf{u}^{n+1} + L_{NS}[\mathbf{u}^*]\mathbf{u}^{n+1} + \nabla(q^{n+1} + \chi q_f^{n+1}) + \\ &\qquad \chi\{L_{NS}[\mathbf{u}^*]\left(\mathbf{v}^{n+1} - \mathbf{v}_f^{n+1}\right) + \alpha L_F[\mathbf{v}^{n+1}]\mathbf{v}_f^{n+1}\} = \tfrac{\rho}{\Delta t}\mathbf{u}^n,\end{aligned} \tag{3.3}$$

where the right hand side incorporates the terms of the discretization of the time derivative. The third term on the first line can be written as ∇p^{n+1}, using (2.25).

In what follows, we use the following well-known generic identities for two generic arguments of the scalar product a and b

$$(a, a-b) = \frac{1}{2}\|a\|^2 + \frac{1}{2}\|a-b\|^2 - \frac{1}{2}\|b\|^2, \qquad (b, a-b) = \frac{1}{2}\|a\|^2 - \frac{1}{2}\|a-b\|^2 - \frac{1}{2}\|b\|^2 \tag{3.4}$$

and the specific equations

$$\mathbf{v}^{n+1} - \mathbf{u}^{n+1} = \chi\left(\mathbf{v}^{n+1} - \mathbf{v}_f^{n+1}\right), \quad \chi\mathbf{v}_f^{n+1} = \mathbf{u}^{n+1} - (1-\chi)\mathbf{v}^{n+1}. \tag{3.5}$$

Also, we will refer to the traditional form of the gradient for simplicity.

By standard multiplication of (3.3) by $\mathbf{u}^{n+1}$ and integration by parts, considering the Neumann conditions for $\mathbf{v}^{n+1}$ and $\mathbf{v}_f^{n+1}$ on Γ_N we obtain

$$\begin{aligned}&\frac{\rho}{\Delta t}\|\mathbf{u}^{n+1}\|^2 + \frac{1}{2}\int_{\Gamma_N} \rho|\mathbf{u}^{n+1}|^2\mathbf{u}^* \cdot \mathbf{n}d\gamma + \mu\|\nabla\mathbf{u}^{n+1}\|^2 + \\ &\chi\left(\int_\Omega \rho(\mathbf{u}^* \cdot \nabla)(\mathbf{v}^{n+1} - \mathbf{v}_f^{n+1}) \cdot \mathbf{u}^{n+1}d\omega + \mu(\nabla(\mathbf{v}^{n+1} - \mathbf{v}_f^{n+1}), \nabla\mathbf{u}^{n+1})\right) + \\ &\chi(\mu_f\nabla\mathbf{v}_f^{n+1}, \nabla\mathbf{u}^{n+1}) = \frac{\rho}{\Delta t}(\mathbf{u}^n, \mathbf{u}^{n+1}).\end{aligned} \tag{3.6}$$

As previously pointed out, the second term in the first line in the presence of backflow prevents a bound on the solution, as it may be negative. To the two terms in the second line

we apply the first equation in (3.5) and obtain

$$\int_\Omega \rho(\mathbf{u}^* \cdot \nabla)(\mathbf{v}^{n+1} - \mathbf{u}^{n+1}) \cdot \mathbf{u}^{n+1} d\omega + \mu(\nabla(\mathbf{v}^{n+1} - \mathbf{u}^{n+1}), \nabla \mathbf{u}^{n+1})$$
$$= \int_\Omega \rho(\mathbf{u}^* \cdot \nabla)(\mathbf{v}^{n+1} - \mathbf{u}^{n+1}) \cdot \mathbf{u}^{n+1} d\omega + \frac{\mu}{2}\|\nabla \mathbf{v}^{n+1}\|^2 - \frac{\mu}{2}\|\nabla(\mathbf{v}^{n+1} - \mathbf{u}^{n+1})\|^2 - \frac{\mu}{2}\|\nabla \mathbf{u}^{n+1}\|^2, \tag{3.7}$$

where we used the second identity in (3.4).

For the term in the third line of (3.6), using the second equation in (3.5) we obtain

$$(\mu_f \nabla \mathbf{u}^{n+1}, \nabla \mathbf{u}^{n+1}) - (1-\chi)(\mu_f \nabla \mathbf{v}^{n+1}, \nabla \mathbf{u}^{n+1}). \tag{3.8}$$

From (3.6), after a standard application of the Young inequality at the right hand side, we obtain therefore

$$\frac{\rho}{2\Delta t}\|\mathbf{u}^{n+1}\|^2 + \frac{1}{2}\int_{\Gamma_N} \rho|\mathbf{u}^{n+1}|^2 \mathbf{u}^* \cdot \mathbf{n} d\gamma + \frac{\mu}{2}\|\nabla \mathbf{u}^{n+1}\|^2 + \frac{\mu}{2}\|\nabla \mathbf{v}^{n+1}\|^2 - \frac{\mu}{2}\|\nabla(\mathbf{v}^{n+1} - \mathbf{u}^{n+1})\|^2 +$$
$$\rho \int_\Omega (\mathbf{u}^* \cdot \nabla)(\mathbf{v}^{n+1} - \mathbf{u}^{n+1}) \cdot \mathbf{u}^{n+1} d\omega +$$
$$(\mu_f \nabla \mathbf{u}^{n+1}, \nabla \mathbf{u}^{n+1}) - (1-\chi)(\mu_f \nabla \mathbf{v}^{n+1}, \nabla \mathbf{u}^{n+1}) \leq \frac{\rho}{2\Delta t}\|\mathbf{u}^n\|^2. \tag{3.9}$$

Let us focus on the term in the second line. By direct computation and the divergence

Theorem, we have

$$
\begin{aligned}
&\int_\Omega (\mathbf{u}^* \cdot \nabla)(\mathbf{v}^{n+1} - \mathbf{u}^{n+1}) \cdot \mathbf{u}^{n+1} d\omega \\
&= \frac{1}{2}\int_\Omega (\mathbf{u}^* \cdot \nabla)\mathbf{v}^{n+1} \cdot \mathbf{u}^{n+1} d\omega - \frac{1}{2}\int_\Omega (\mathbf{u}^* \cdot \nabla)\mathbf{u}^{n+1} \cdot \mathbf{u}^{n+1} d\omega + \\
&\frac{1}{2}\int_\Omega (\mathbf{u}^* \cdot \nabla)(\mathbf{v}^{n+1} - \mathbf{u}^{n+1}) \cdot (\mathbf{u}^{n+1} - \mathbf{v}^{n+1}) d\omega + \frac{1}{2}\int_\Omega (\mathbf{u}^* \cdot \nabla)\mathbf{v}^{n+1} \cdot \mathbf{v}^{n+1} d\omega \\
&= \frac{1}{2}\int_{\Gamma_N} (\mathbf{u}^* \cdot \mathbf{n})\, \mathbf{v}^{n+1} \cdot \mathbf{u}^{n+1} d\gamma - \frac{1}{2}\int_\Omega (\mathbf{u}^* \cdot \nabla)\mathbf{u}^{n+1} \cdot \mathbf{v}^{n+1} d\omega \\
&-\frac{1}{4}\int_{\Gamma_N} (\mathbf{u}^* \cdot \mathbf{n})\, |\mathbf{u}^{n+1}|^2 d\gamma - \frac{1}{4}\int_{\Gamma_N} (\mathbf{u}^* \cdot \mathbf{n})\, |\mathbf{v}^{n+1} - \mathbf{u}^{n+1}|^2 d\gamma + \frac{1}{4}\int_{\Gamma_N} (\mathbf{u}^* \cdot \mathbf{n})\, |\mathbf{v}^{n+1}|^2 d\gamma \\
&-\frac{1}{2}\int_\Omega (\mathbf{u}^* \cdot \nabla)\mathbf{u}^{n+1} \cdot \mathbf{v}^{n+1} d\omega
\end{aligned}
$$

Sum the term $\frac{1}{2}\int_{\Gamma_N} |\mathbf{u}^{n+1}|^2 \mathbf{u}^* \cdot \mathbf{n} d\gamma$ in (3.9) to what we obtained above, to get

$$
\begin{aligned}
&\frac{1}{2}\int_{\Gamma_N} (\mathbf{u}^* \cdot \mathbf{n})\, \mathbf{v}^{n+1} \cdot \mathbf{u}^{n+1} d\gamma - \int_\Omega (\mathbf{u}^* \cdot \nabla)\mathbf{u}^{n+1} \cdot \mathbf{v}^{n+1} d\omega \\
&+\frac{1}{4}\int_{\Gamma_N} (\mathbf{u}^* \cdot \mathbf{n})\, |\mathbf{u}^{n+1}|^2 d\gamma - \frac{1}{4}\int_{\Gamma_N} (\mathbf{u}^* \cdot \mathbf{n})\, |\mathbf{v}^{n+1} - \mathbf{u}^{n+1}|^2 d\gamma + \frac{1}{4}\int_{\Gamma_N} (\mathbf{u}^* \cdot \mathbf{n})\, |\mathbf{v}^{n+1}|^2 d\gamma \\
&= -\int_\Omega (\mathbf{u}^* \cdot \nabla)\mathbf{u}^{n+1} \cdot \mathbf{v}^{n+1} d\omega + \frac{1}{4}\int_{\Gamma_N} (\mathbf{u}^* \cdot \mathbf{n}) \left(|\mathbf{u}^{n+1}|^2 + |\mathbf{v}^{n+1}|^2 - 2\mathbf{v}^{n+1} \cdot \mathbf{u}^{n+1}\right) d\gamma \\
&-\frac{1}{4}\int_{\Gamma_N} (\mathbf{u}^* \cdot \mathbf{n})\, |\mathbf{v}^{n+1} - \mathbf{u}^{n+1}|^2 d\gamma \\
&= -\int_\Omega (\mathbf{u}^* \cdot \nabla)\mathbf{u}^{n+1} \cdot \mathbf{v}^{n+1} d\omega.
\end{aligned}
$$

Now, let us consider the second term in the third line of (3.9). Using the fact that

$$
\mathbf{u}^{n+1} = \mathbf{v}^{n+1} - \chi(\mathbf{v}^{n+1} - \mathbf{v}_f^{n+1})
$$

we obtain

$$
\begin{aligned}
&-(1-\chi)(\mu_f \nabla \mathbf{v}^{n+1}, \nabla \mathbf{u}^{n+1}) = (1-\chi)\left[-(\mu_f \nabla \mathbf{v}^{n+1}, \nabla \mathbf{v}^{n+1})\right.\\
&\left.+\chi(\mu_f \nabla \mathbf{v}^{n+1}, \nabla(\mathbf{v}^{n+1} - \mathbf{v}_f^{n+1}))\right] = (1-\chi)\left[-\left(1-\frac{\chi}{2}\right)(\mu_f \nabla \mathbf{v}^{n+1}, \nabla \mathbf{v}^{n+1})\right.\\
&\left.+\frac{\chi}{2}(\mu_f \nabla(\mathbf{v}^{n+1} - \mathbf{v}_f^{n+1}), \nabla(\mathbf{v}^{n+1} - \mathbf{v}_f^{n+1})) - \frac{\chi}{2}(\mu_f \nabla \mathbf{v}_f^{n+1}, \nabla \mathbf{v}_f^{n+1})\right].
\end{aligned}
$$

Finally, notice that

$$
\frac{\mu}{2}\|\nabla \mathbf{u}^{n+1}\|^2 + \frac{\mu}{2}\|\nabla \mathbf{v}^{n+1}\|^2 - \frac{\mu}{2}\|\nabla(\mathbf{v}^{n+1} - \mathbf{u}^{n+1})\|^2 = \mu(\nabla \mathbf{u}^{n+1}, \nabla \mathbf{v}^{n+1}).
$$

Collecting all the steps so far, inequality (3.9) becomes

$$
\begin{aligned}
&\frac{\rho}{2\Delta t}\|\mathbf{u}^{n+1}\|^2 - \rho\int_\Omega (\mathbf{u}^* \cdot \nabla)\mathbf{u}^{n+1} \cdot \mathbf{v}^{n+1} d\omega + \mu(\nabla \mathbf{u}^{n+1}, \nabla \mathbf{v}^{n+1}) + (\mu_f \nabla \mathbf{u}^{n+1}, \nabla \mathbf{u}^{n+1})\\
&+(1-\chi)\left[-\left(1-\frac{\chi}{2}\right)(\mu_f \nabla \mathbf{v}^{n+1}, \nabla \mathbf{v}^{n+1}) + \frac{\chi}{2}(\mu_f \nabla(\mathbf{v}^{n+1} - \mathbf{v}_f^{n+1}), \nabla(\mathbf{v}^{n+1} - \mathbf{v}_f^{n+1}))\right.\\
&\left.-\frac{\chi}{2}(\mu_f \nabla \mathbf{v}_f^{n+1}, \nabla \mathbf{v}_f^{n+1})\right] \leq \frac{\rho}{2\Delta t}\|\mathbf{u}^n\|^2.
\end{aligned}
\tag{3.10}
$$

Notice that for $\chi = 0$, i.e. in absence of stabilization ($\mathbf{u}^{n+1} = \mathbf{v}^{n+1}$), we retrieve the standard energy estimate where the convective term is negative for the backflows, so it prevents a bound on the solution. Also, notice that all the terms multiplied by $(1-\chi)$ are negative. This can be promptly proved under the assumption that $\mathbf{v}^{n+1} \in H^3(\Omega)$ (which is a consequence of regularity of the data as inferred in [104]). In this case, also $\mathbf{v}_f^{n+1} \in H^3(\Omega)$. Then, from the weak formulation of (2.22), with the test function $\nabla \cdot (\mu_f \nabla \mathbf{v}_f^{n+1})$ (that belongs to H^1 for the regularity assumptions), we find that $(\mu_f \nabla \mathbf{v}^{n+1}, \nabla \mathbf{v}_f^{n+1}) > 0$ [105, 106, 107, 108]. The statement follows observing that

$$
\begin{aligned}
&-(1-\chi)\left(1-\frac{\chi}{2}\right)(\mu_f \nabla \mathbf{v}^{n+1}, \nabla \mathbf{v}^{n+1}) + \frac{\chi}{2}(1-\chi)(\mu_f \nabla(\mathbf{v}^{n+1} - \mathbf{v}_f^{n+1}), \nabla(\mathbf{v}^{n+1} - \mathbf{v}_f^{n+1}))\\
&-\frac{\chi}{2}(1-\chi)(\mu_f \nabla \mathbf{v}_f^{n+1}, \nabla \mathbf{v}_f^{n+1}) = -(1-\chi)^2(\mu_f \nabla \mathbf{v}^{n+1}, \nabla \mathbf{v}^{n+1}) - (1-\chi)\chi(\mu_f \nabla \mathbf{v}^{n+1}, \nabla \mathbf{v}_f^{n+1}).
\end{aligned}
$$

Another way of proving the statement is to recall that all the terms multiplied by $(1-\chi)$ come from the second term in the third line of (3.9). Then, by using (2.24), we have:

$$-(1-\chi)(\mu_f \nabla \mathbf{v}^{n+1}, \nabla \mathbf{u}^{n+1}) = -(1-\chi)^2(\mu_f \nabla \mathbf{v}^{n+1}, \nabla \mathbf{v}^{n+1}) - (1-\chi)\chi(\mu_f \nabla \mathbf{v}^{n+1}, \nabla \mathbf{v}_f^{n+1}).$$

Now, we prove that for $\chi = 1$ the stabilizing term, i.e. the fourth term in (3.10), can be selected to control the convective term. In fact, for $\chi = 1$, we have $\mathbf{u}^{n+1} = \mathbf{v}_f^{n+1}$. Thus, following the same arguments used above and noting that $\mu_f \geq c > 0$ for c constant we have that $(\nabla \mathbf{v}^{n+1}, \nabla \mathbf{u}^{n+1}) > 0$. Then, (3.10) reads

$$\begin{aligned} &\frac{\rho}{2\Delta t}\|\mathbf{u}^{n+1}\|^2 - \int_\Omega \rho(\mathbf{u}^* \cdot \nabla)\mathbf{u}^{n+1} \cdot \mathbf{v}^{n+1} d\omega + \mu(\nabla \mathbf{u}^{n+1}, \nabla \mathbf{v}^{n+1}) + \alpha(\mu_f \nabla \mathbf{u}^{n+1}, \nabla \mathbf{u}^{n+1}) \\ &\leq \frac{\rho}{2\Delta t}\|\mathbf{u}^n\|^2. \end{aligned} \tag{3.11}$$

As μ_f is proportional to the filter radius δ^2, it is enough to select a radius large enough to guarantee

$$(\mu_f \nabla \mathbf{u}^{n+1}, \nabla \mathbf{u}^{n+1}) \geq \left| \int_\Omega \rho(\mathbf{u}^* \cdot \nabla)\mathbf{u}^{n+1} \cdot \mathbf{v}^{n+1} d\omega \right|$$

As the entire energy depends continuously on χ, by a continuity argument we have that for $\chi \to 1^-$

$$\|\mathbf{u}^{n+1}\| \leq \|\mathbf{u}^n\|$$

and then recursively

$$\|\mathbf{u}^n\| \leq \|\mathbf{u}_0\|.$$

$\triangle$

Although the proof does not give specific indication on the choice of δ, it does actually show that there exists a choice of the filtering radius and the relaxation parameter that allows to control the occurrence of backflows. Numerical experiments in the next Section

support this statement.

3.3 Numerical Experiments

In order to verify our theory numerically, we perform three tests. The first two tests feature idealized geometries: a straight channel for test 1 and a curved channel for test 2. For the third test, we use a patient-specific geometry of the aorta with an abdominal aneurysm. In all the tests, a combination of the geometry and boundary conditions trigger the backflow instability. The purpose of Test 1 is to compare the results obtained using our Leray-EFR model with the benchmark results in [42] for a "stress test" that does not refer to any specific physical condition. Test 2 is not realistic either, yet it aims at investigating the sensitivity of the stabilization provided by the LES-EFR model to model parameters δ and χ for different meshes and time steps. Finally, test 3 assesses the efficacy of our method in a realistic setting. The results are compared with an alternative methodology currently used in the literature, emphasizing the excellent accuracy in terms of flow rates.

We use the Leray-EFR scheme (2.20) - (2.25), with a space discretization based on inf-sup stable finite element pairs: $\mathbb{P}_2/\mathbb{P}_1$ for test 1 and 2, and $\mathbb{P}_1 - \text{Bubble}/\mathbb{P}_1$ for test 3. Since test 3 involves flow in a complex geometry, the choice of the $\mathbb{P}_1 - \text{Bubble}/\mathbb{P}_1$ pair is motivated by the reduced computational cost. For all the tests we used BDF2 (2.19) for the time-discretization of problem (2.20)-(2.21), with a semi-implicit treatment of the convective term based on a second order extrapolation.

3.3.1 Test 1: asymmetrical reversed flow in a straight channel

Inspired by a benchmark test proposed in [42] for a 2D problem with backflow in a rectangular domain, we consider fluid flow in a 3D straight channel with the inflow boundary condition given by a skewed Womersley-like solution. We recall that the Womersley solution is the counterpart of the well-known Poiseuille-Hagen solution for a steady incompressible fluid in a cylinder when a periodic-in-time pressure drop is prescribed [109]. The

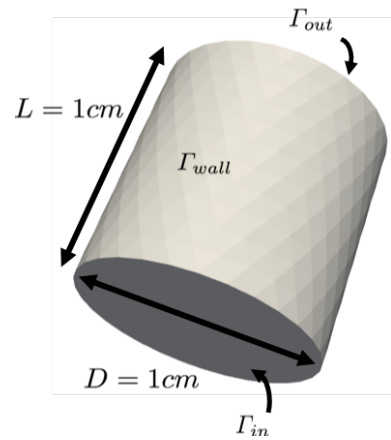

Figure 3.1: Numerical experiment 1: asymmetrical reversed flow in a straight channel

2D version of the Womersley solution advocated in [42] can be found in [110].

Problem setup

Let $\mathbf{x} = (x_1, x_2, x_3)$ be a point in $\mathbb{R}^3$. The domain $\Omega \subset \mathbb{R}^3$ is a cylinder, shown in Fig. 3.1, with $\Gamma_{in} = \{\mathbf{x} \in \Omega : x_3 = 0\}$, $\Gamma_{out} = \{\mathbf{x} \in \Omega : x_3 = L\}$, and $\Gamma_{wall} = \{\mathbf{x} \in \Omega : \sqrt{x_1^2 + x_2^2} = D/2\}$. Here, L and D are the cylinder height and diameter with the value $D = L = 1\,\mathrm{cm}$. We consider the flow of an incompressible fluid with density $\rho = 1.06\,\mathrm{g/cm^3}$ and viscosity $\mu = 0.035\,\mathrm{dyn} \cdot \mathrm{s/cm^2}$ (as described in 2.1.1) in domain Ω. The combination of geometrical and physical parameters described here generates the physiological backflow conditions that arise in aortic branches like supra aortic, renal and celiac arteries during the deceleration phase of blood flow. The peak Reynolds number for this test is around 200.

Let W be a Womersley-like velocity profile:

$$W(\mathbf{x}, t) = \sum_{k=0}^{K} d_k \Phi_k(t) S_k(\mathbf{x})$$

with

$$
\begin{aligned}
d_k &= \frac{4\Delta P}{\rho\pi(2k+1)((2k+1)^4\sigma^2\pi^4+\omega^2)}, \quad \sigma = \frac{\mu}{\rho L^2}, \\
\Phi_k(t) &= (2k+1)^2\sigma\pi^2\sin(\omega t) - \omega\cos(\omega t) + \omega\exp((-2k+1)^2\sigma\pi), \\
S_k(\mathbf{x}) &= \sin\left(\pi(2k+1)\frac{\sqrt{(x_1^2+x_2^2)}}{D}\right).
\end{aligned}
$$

Here, K is the number of modes, ΔP and ω are the prescribed pressure drop and its frequency. For the numerical results, we set $K = 19$, $\Delta P = 40\,\mathrm{dyn/cm^2}$, and $\omega = 2\pi\,\mathrm{rad/s}$.

We define velocity $\mathbf{u}_W$ as a skewed velocity profile based on W [42]:

$$
\mathbf{u}_W = \left(0, 0, \frac{3}{2}x_1^{0.7}W(\mathbf{x}, t)\right)
$$

where the x_1 factor is intended to break the symmetry so to trigger the non-linear convective terms, which are otherwise vanishing in the original Womersley solution. Then, we call reference solution $(\mathbf{u}_{ref}, p_{ref})$ the solution to the incompressible Navier-Stokes equations (2.1)-(2.2) with boundary conditions:

$$
\mathbf{u}_{ref} = \mathbf{u}_W \ \text{ on } \ \Gamma_{in} \times (0, T)\,, \tag{3.12}
$$

$$
\mathbf{u}_{ref} = \mathbf{0} \ \text{ on } \ \Gamma_{wall} \times (0, T)\,, \tag{3.13}
$$

$$
(\mu\nabla\mathbf{u}_{ref} - p_{ref}\mathbf{I})\mathbf{n} = \mathbf{0} \ \text{ on } \ \Gamma_{out} \times (0, T)\,. \tag{3.14}
$$

The Navier-Stokes problem with these boundary conditions (3.12)-(3.14) will be denoted hereafter as *reference problem*.

To induce backflow instability and therefore test the performance of the Leray-EFR scheme, this first benchmark problem is constructed with Neumann boundary condition at Γ_{in} corresponding to the reference solution $(\mathbf{u}_{ref}, p_{ref})$. In particular, let $(\mathbf{u}_{back}, p_{back})$ be the solution to the Navier-Stokes equations with the inlet condition ”borrowed” from the

reference problem and the following boundary conditions on Γ_{wall} and Γ_{out}:

$$(\mu\nabla\mathbf{u}_{back} - p_{back}\mathbf{I})\mathbf{n} = (\mu\nabla\mathbf{u}_{ref} - p_{ref}\mathbf{I})\mathbf{n} \text{ on } \Gamma_{in} \times (0,T)\,, \tag{3.15}$$

$$\mathbf{u}_{back} = \mathbf{0} \text{ on } \Gamma_{wall} \times (0,T)\,, \tag{3.16}$$

$$(\mu\nabla\mathbf{u}_{back} - p_{back}\mathbf{I})\mathbf{n} = \mathbf{0} \text{ on } \Gamma_{out} \times (0,T)\,. \tag{3.17}$$

Hereafter, we call *backflow problem* the Navier-Stokes problem with boundary conditions (3.15)-(3.17). Since we prescribe Neumann boundary condition (3.15) at Γ_{in}, the problem becomes unstable because of the $\mathbf{u}\cdot\mathbf{n}$ term and therefore backflow stabilization at the inflow boundary is needed. To this purpose, we use the Leray-EFR scheme for the backflow problem. The numerical results obtained with the Leray-EFR algorithm are then compared to the reference solution.

REMARK The reference and the backflow boundary problems are solved with the same mesh, so the boundary data $(\mu\nabla\mathbf{u}_{ref} - p_{ref}\mathbf{I})\mathbf{n}$ on Γ_{in} are promptly retrieved in the finite element formulation at each time step by taking the residual of the system assembled for the reference problem *before the enforcement of the Dirichlet condition* (3.12). In fact, this residual applied to the reference solution returns at the degrees of freedom of Γ_{in} the vector to be prescribed as boundary data for condition (3.15) with no additional numerical error.

At each time iteration $n+1$, we perform the following three steps:

1. Solve the reference problem.

2. Compute the residual of the system before the application of the Dirichlet inflow condition (3.12) to obtain the weak form of the traction to be used as data in (3.15).

3. Solve the backflow problem stabilized by the EFR scheme.

△

Numerical results

The solution of the backflow problem over time interval $[0, 0.5]\mathrm{s}$ was approximated, with time step $\Delta t = 5 \times 10^{-3}\,\mathrm{s}$. The peak backflow occurs at $t = 0.48\,\mathrm{s}$.

The spatial domain is discretized with an unstructured tetrahedral mesh with the minimum mesh size $h_{min} = 0.07\,\mathrm{cm}$ and average mesh size $h_{avg} = 0.12\,\mathrm{cm}$. The choice of the spatial discretization is such that the reference problem is solved without the need of stabilization for the convective term.

With the Leray-EFR model with $\chi = 0.4$ and $\delta = h_{avg}$, we obtain a solution that compares well with the reference solution. The choice of δ is consistent with the general strategies advocated in the literature (δ scaling linearly with the mesh size), while the choice of χ here is empirical, since we have no theoretical background for a specific choice. While the Theorem states that the backflow stabilization becomes effective for $\chi \to 1^-$, we opted for a selection of a smaller χ, to be progressively increased in order to achieve stability. For $\chi = 0.4$, we get a stable result. In particular, we get an accurate pressure drop over time and velocity magnitude at Γ_{in}, as shown in Fig. 3.2 and 3.3b, respectively. Notice that Fig. 3.3b pinpoints the excellent reconstruction of the pressure. Fig. 3.3a shows flow rate at Γ_{in} over time. We see that the stabilization introduces dissipation. This dissipation, taken as the maximum reduction of the stabilized flow rate vs. the reference solution, is around the 30%. This damping occurs in this specific test and it compares very well with the extensive results presented in [42]. In fact, the flow rate damping induced by popular stabilization techniques in the 2D benchmark of reference [42] can be up to the 90% (see, e.g., Fig. 4 in [42]). These percentages refer to the peak of the dissipation in a specific boundary point. We notice that the damping effect over the entire domain in realistic simulations is much less, as the subsequent numerical simulations will demonstrate. It is enough to get a stable solution and it is worth to mention that there is no boundary condition modification in the approach we propose, since the backflow instability is fixed directly by the LES modeling.

The success of the Leray-EFR model as a backflow stabilization technique depends

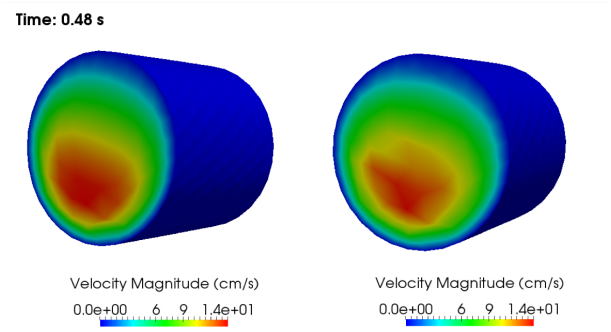

Figure 3.2: Test 1: velocity magnitude at the inflow boundary at the time when peak backflow occurs. Left: reference solution. Right: solution to the backflow problem stabilized by Leray-EFR scheme.

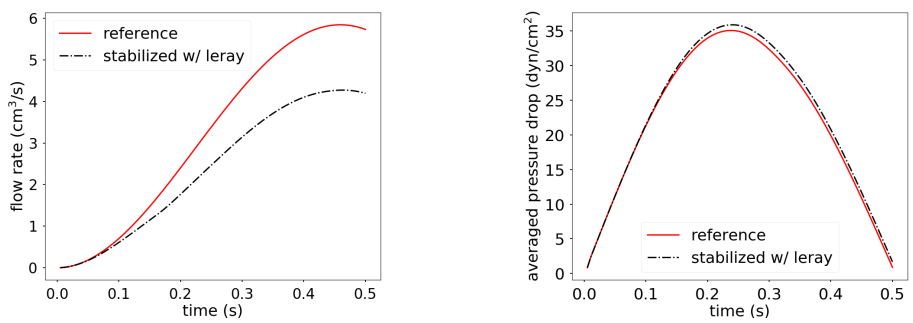

(a) flow rate at Γ_{in} over time

(b) pressure drop over time

Figure 3.3: Test 1: flow rate at Γ_{in} over time and pressure drop over time - comparison between the reference and the stabilized solutions.

on two parameters: δ and χ. By carefully tuning these parameters, less damped inflow rates can be achieved. In the absence of theoretical statements, and consistently with the literature in this field (where these parameters are recognized to be generally problem-dependent), the next test aims at establishing some qualitative indications.

3.3.2 Test 2: reversed flow in a curved channel

For this second benchmark test, an idealized curved tube that can possibly trigger backflow instability is considered. The aim is to investigate the sensitivity of the stabilization to model and discretization parameters in an idealized - yet nontrivial - case and to probe the interplay between these parameters and the discretization.

Problem setup

The idealized geometry under consideration is a portion of a torus whose cross-section has a decreasing radius, from $0.7\,\mathrm{cm}$ at one end to $0.3\,\mathrm{cm}$ at the other end as in Fig. 3.4. We consider the flow of an incompressible fluid with the kinematic viscosity $\nu = \dfrac{\mu}{\rho} = 0.01\,\mathrm{cm}^2/\mathrm{s}$ for this problem. Let the section with the largest (resp., smallest) diameter be the inlet (resp., outlet).

Three unstructured tetrahedral meshes were created with *NetGen* [111] (Fig. 3.4). These meshes have progressive refinements to check that the instability is due to back-flows and not to under-refinement. The details about the three different meshes are listed in Tab. 3.1. From now on, the three cases will be referred to as *coarse mesh* (C), *medium mesh* (M) and *fine mesh* (F).

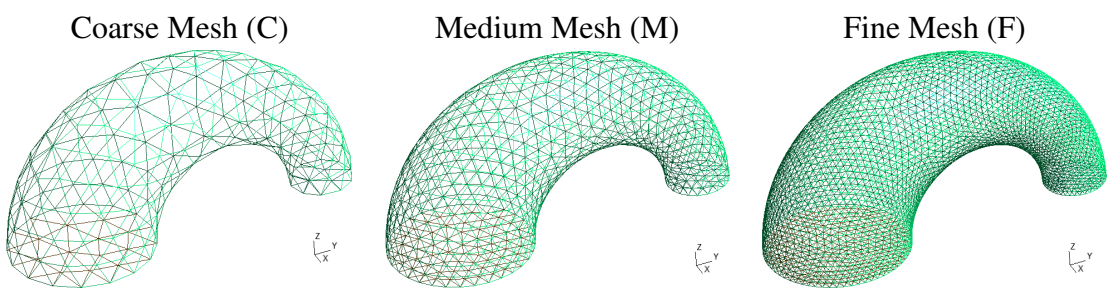

Figure 3.4: Test 2: progressively refined meshes for the geometry, visualization of the surface triangles. GMSH [112] Visualization with green lines in the foreground and black lines in the background.

Table 3.1: Test 2: mesh details for the three meshes under consideration.

mesh	# nodes	# surface elements	# tetrahedra	h_{min}	h_{max}
C	266	418	824	0.191	0.805
M	1564	1672	6592	0.095	0.591
F	10555	6688	52736	0.047	0.295

Numerical results

We preliminaryly run the Navier-Stokes solver (no LES modeling) with the three meshes under consideration to certify that the reason of the instability is due to the backflow. The

flow in this case is driven by a periodic pressure drop described by $8\sin(\pi t)$. A no-slip boundary condition is prescribed on the lateral wall. The simulation is started from fluid at rest and has a peak Reynolds number of about 800.

The velocity magnitude and pressure field on the medial plane, and velocity vectors near the outlet at time $1.0\,\mathrm{s}$ computed with mesh C are shown in Fig. 3.5. One can clearly see the onset of the instability near the outlet. The instability occurred for all meshes. In particular, they arise at time $t = 1.0, 0.9, 0.8\,\mathrm{s}$ for mesh C, M and F, respectively. The fact that the instability do not disappear or reduce as the mesh gets refined indicates that the cause is the backflow, rather than the large Reynolds number.

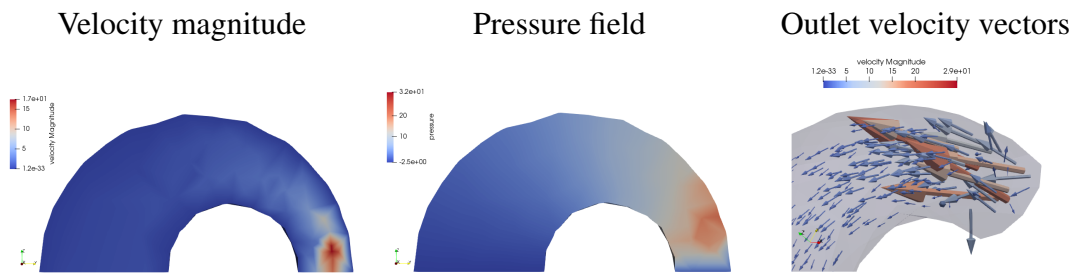

Figure 3.5: Test 2: velocity magnitude (left) and pressure field (center) on a section of the domain, and velocity vectors near the outlet (right) at time $t = 1.0\,\mathrm{s}$ computed by the Navier-Stokes solver (no LES modeling) with mesh C and time step $\Delta t = 0.1\,\mathrm{s}$.

Successively, we focus on meshes M and F with two different time steps, $\Delta t = 0.01$ s and 0.005 s and our LES-EFR scheme. With these time steps and meshes, the BDF2 semi-implicit time advancing scheme is stable. The ultimate goal is a qualitative understanding of how δ and χ should be selected in practice. The flow in this case is driven by a a parabolic inflow (at the larger entrance) with the inflow rate of $2\sin(\pi t)$. The no-slip boundary condition is prescribed on the lateral wall and the homogeneous Neumann condition is enforced at the outlet. The simulation starts at rest and has a peak Reynolds number of about 300.

We tested the statement of the Theorem that for χ large enough backflow instabilities are suppressed. The results for the mesh F and $\Delta t = 0.005$ s, $\delta = h_{min}$ and two different choices of χ, 0.04 and 0.06 respectively, are reported in Fig. 3.6. As shown in Fig. 6,

for $\chi = 0.04$ the simulation suffers from backflow instability, while it runs regularly for $\chi = 0.06$. Therefore, the results confirm that LES-EFR with a large enough χ damps backflow instabilities.

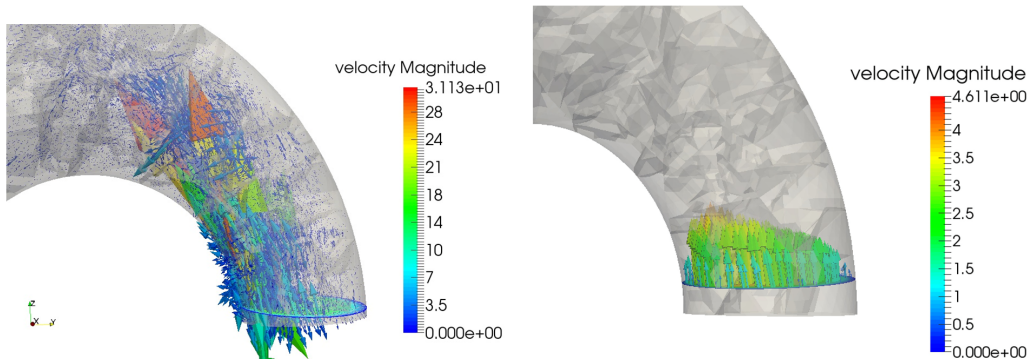

Figure 3.6: Test 2, role of χ for suppressing backflows instability: on mesh F, with $\Delta t = 0.005$s, for $\delta = h_{min}$, a value of $\chi = 0.04$ does not prevent backflow instability (left), while $\chi = 0.06$ does (right).

In a subsequent set of simulations, we tested the interplay between χ and δ. The rationale is to verify that they may mutually compensate, so that a large figure for one can reduce the value of the other. The value of the minimal relaxation parameter that attains stability for different values of δ is reported In Tab. 3.3.2. In one case, we selected $\delta = h_{min}$ (as recommended in the relevant literature on LES-EFR), in the other one, we fixed $\delta = 0.9$. The results show that, in general, with a larger δ, χ can be decreased to obtain the stability. For instance, for the mesh F ($\Delta t = 0.01s$), with $\delta = 0.9$ a relaxation of $\chi = 0.06$ is enough for stabilization, while we need at least $\chi = 0.08$ for a smaller δ. On the other hand, without relaxation, a large δ is however not sufficient, i.e. χ must be always large enough ($\chi = 0$ does not work). For the smaller Δt ($\Delta t = 0.005s$), the value of χ that guarantees stability is virtually independent of δ.

$\delta = 0.9$			
Mesh		M	F
Δt	0.01	0.06	0.06
	0.005	0.04	0.05

Table 3.2: Test 2, minimal values of χ to obtain stability for different values of δ: a larger δ can be compensated by a smaller χ (and vice-versa).

$\delta = h_{min}$			
Mesh		M	F
Δt	0.01	0.07	0.08
	0.005	0.04	0.06

$\delta = 0.9$			
Mesh		M	F
Δt	0.01	0.06	0.06
	0.005	0.04	0.05

Finally, we tested the interplay between the LES-EFR parameters and the time discretization. It is generally recommended [72] that χ scales with Δt. However, this recommendation refers to the modeling of turbulence and not to the backflow stabilization. It can be inferred from Tab. 3.3.2 that the reduction of the relaxation parameter with Δt is apparent, yet the scaling is sub-linear. This holds for the two meshes M and F when $\delta = h_{min}$.

Figure 3.7: Test 2: interplay between χ and Δt in the mesh F: time step $\Delta t = 0.01$ is stable with $\chi = 0.08$ (left), while for $\Delta t = 0.005$ stability requires $\chi = 0.06$ (right). In the latter case, the solution shows less dissipation - as expected - inferred by the larger velocity magnitude.

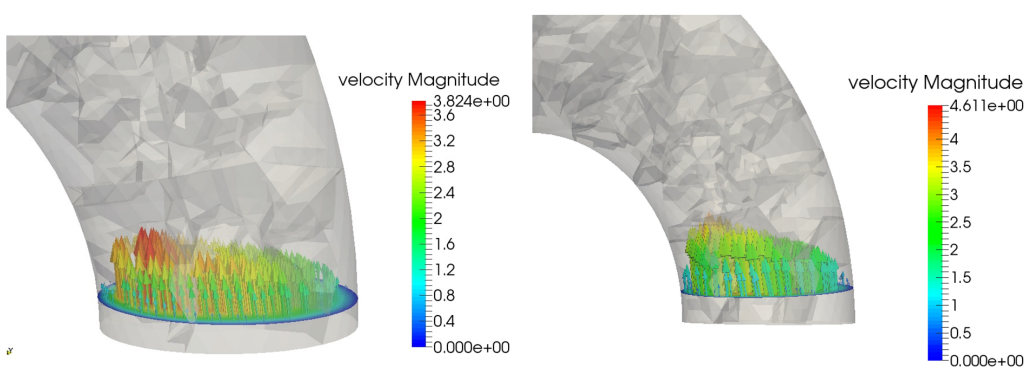

We qualitatively corroborate this statement with Fig. 3.7, where we show the results on the fine mesh, with two different time steps. With a smaller time step we can reduce the relaxation parameter and the results - although comparable - show less numerical dissipa-

tion.

It has been pointed out that the optimal choice of the parameters in LES-EFR is generally problem-dependent [64]. In absence of a precise theoretical framework, these tests will lead to our conclusive statements about the practical selection of those parameters.

3.3.3 Test 3: hemodynamics in a patient-specific aorta

After testing the backflow stabilization performance of the Leray-EFR model in idealized geometries, we consider a complicated geometry used for a real clinical study: a patient-specific aorta with an abdominal aneurysm. In this geometry, the hemodynamics driven by the patient-specific inflow rate at the ascending aorta suffers from backflow instabilities.

Problem setup

The patient's aorta is reconstructed from the CT images using VMTK (Vascular Modeling Tool Kit) [113]. The data were collected in the frame of the `iCardioCloud` Project [114, 37]. The supra-aortic branches, i.e. the brachiocephalic, left common carotid and left subclavian arteries, are included in the image reconstruction, which is shown as the geometry called geo1 in Fig. 3.8a. Then a second geometry was created, called geo2 (see Fig. 3.8b), by adding artificial flow extensions to all the boundaries of geo1. The extensions, assembled with VMTK, are cylinders with axis along the tangent to the centerline at the original boundaries.

The patient-specific inflow rate shown in Fig. 3.9 with a parabolic velocity profile is imposed as the inflow boundary condition at the ascending aorta. The assumption on the velocity profile is common practice due to the lack of data. The resulting Reynolds number at peak systole at the ascending aorta is $Re = 4659$.

At the outflow boundaries Γ_i, for $i = 1, 2, 3, 4$, we prescribe a set of boundary conditions quite popular in the computational hemodynamics community. These conditions stem from a surrogate modeling of the peripheral circulation that goes under the name

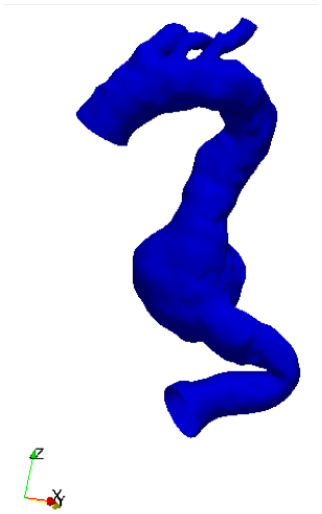

(a) geo1 (without flow extension)

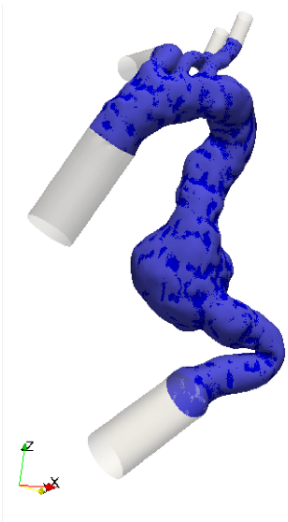

(b) geo2 (with flow extension)

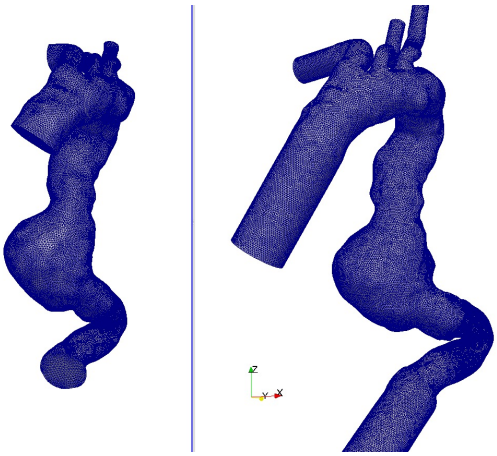

(c) meshes for geo1 and geo2

Figure 3.8: Test 3: patient-specific aorta with abdominal aneurysm reconstructed from CT images (a) without flow extensions (geometry geo1); (b) with flow extensions (geometry geo2); (c) a visualization of the spatial discretization of geo1 (left) and geo2 (right)..

of Three-Element Windkessel (3WK) [18, 35, 37]. In short, the peripheral circulation is described by a differential equation in time that combines the outflow average pressure $\bar{p} \equiv \int_{\Gamma_i} p d\gamma / \int_{\Gamma_i} d\gamma$ and the flow rate $Q \equiv \rho \int_{\Gamma_i} \mathbf{u} \cdot \mathbf{n} d\gamma$. The equation depends on three parameters: R_p and R_d, which represent the viscous dissipation in the proximal and distal region of the outflow, and C (called compliance), which denotes the deformation of the arteries. Then, the 3WK condition at each outflow Γ_i reads

$$p\mathbf{n}_i - 2\mu \nabla^s \mathbf{u} \cdot \mathbf{n}_i = g_i \mathbf{n}_i$$

with $g_i = g_i(t)$ function (with the dimension of a pressure) of time only:

$$g_i(t) = g_i(0)e^{-t/(CR_d)} + R_p \left(Q(t) - Q(0)e^{-t/(CR_d)}\right) + \frac{1}{C}\left(\int_0^t Q(\tau)e^{-(t-\tau)/CR_d} d\tau\right). \tag{3.18}$$

Notice that Q is unknown as it depends on the velocity. These conditions have the same functional form as the conditions (3.1), advocated to stabilize the backflows. However, here the parameters are not tuned to control the negative energy term, rather to provide a lumped parameter description of the downstream circulation. There is no guarantee, in general, that these values stabilize the backflows, as we will see in the results.

The parameters of the 3WK model we use are listed in Table 5.2 and are determined for each outflow using available patient's data as described in [37]. A homogeneous Dirichlet condition is imposed on the arterial wall.

Table 3.3: Test 3: patient-specific Windkessel parameters.

Aortic branches	Three-element Windkessel parameters		
	R_p	R_d	C
	$10^3 \mathrm{dyn} \cdot \mathrm{s/cm}^5$	$10^4 \mathrm{dyn} \cdot \mathrm{s/cm}^5$	$10^{-4} \mathrm{cm}^5/\mathrm{dyn}$
Brachiocephalic artery	0.78	2.03	0.93
Left common carotid	3.80	4.50	0.34
Left subclavian	1.39	3.20	0.58
Abdominal aortic outlet	0.13	0.15	10.90

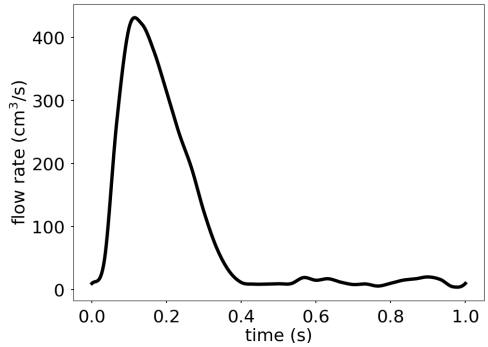

Figure 3.9: Test 3: patient-specific inflow rate over a cardiac cycle.

Geometries geo1 and geo2 are discretized with unstructured tetrahedra, as shown in Fig. 3.8c. The details of the meshes are reported in Table 3.4. Notice that refinement level for the two meshes is comparable. However, due to the presence of the flow extensions in geo2, the number of degrees of freedom for the corresponding mesh is much larger.

Table 3.4: Test 3: details of the meshes used for geometries geo1 and geo2.

geometry	No. of nodes	h_{min}	h_{avg}
geo1	817k	0.03 cm	0.16 cm
geo2	4657k	0.04 cm	0.13 cm

We conducted three numerical tests, called *test 3a, 3b* and *3c*. For all the simulations, $\Delta t = 5 \times 10^{-3}\,\mathrm{s}$ and $T = 6\,\mathrm{s}$, which corresponds to 6 cardiac cycles. The specific setup of the tests is reported in Table 3.5. *Test 3a* uses geo1 and no backflow stabilization at the Neumann boundaries to demonstrate the existence of backflow instability in this patient-specific case. *Test 3b* checks that the backflow instability in geo1 is suppressed when using the Leray-EFR model with $\chi = 0.9$ and $\delta = h_{min}$. The boundary conditions for the Leray-

EFR model are given by:

$$\mathbf{v}^{n+1} = \mathbf{v}_f^{n+1} = \mathbf{u}_{in}^{n+1} \text{ on } \Gamma_{in},$$

$$\mathbf{v}^{n+1} = \mathbf{v}_f^{n+1} = \mathbf{0} \text{ on } \Gamma_{wall},$$

$$(\mu \nabla \mathbf{v}^{n+1} - q^{n+1}\mathbf{I})\mathbf{n}_i = g_i \mathbf{n}_i \text{ on } \Gamma_i,$$

$$(\mu_f^{n+1} \nabla \mathbf{v}_f^{n+1} - q_f^{n+1}\mathbf{I})\mathbf{n}_i = \mathbf{0} \text{ on } \Gamma_i,$$

where the coefficients g_i, for $i = 1, 2, 3, 4$, are the average pressure obtained from the Windkessel model at the outflow boundaries Γ_i as specified in (3.18). In order further evaluate the performance of the Leray-EFR model, we designed *Test 3c* which features a solution comparable to the solution of *Test 3b* but obtained with a different method. For *Test 3c*, we use geo2. The flow extensions in geo 2 are supposed to introduce an energy dissipation that empirically mitigates the impact of backflows [37]. Finally, we recall that the Leray-EFR model in *Test 3b* takes care of the instabilities due the convective term too. To overcome such instabilities in *Test 3a* and *3c*, we apply the classical streamline diffusion stabilization.

Table 3.5: Test 3: setup for the three tests concerning the patient-specific geometry.

Setup	Test		
	Test 3a	*Test 3b*	*Test 3c*
Geometry	geo1	geo1	geo2
Leray-EFR model		$\surd$	
Streamline diffusion	$\surd$		$\surd$
Velocity gradient based backflow Stabilization			$\surd$
Numerically stable	No	Yes	Yes

The results for *Test 3b* and *3c* presented in the next subsection refer to the last cardiac cycle.

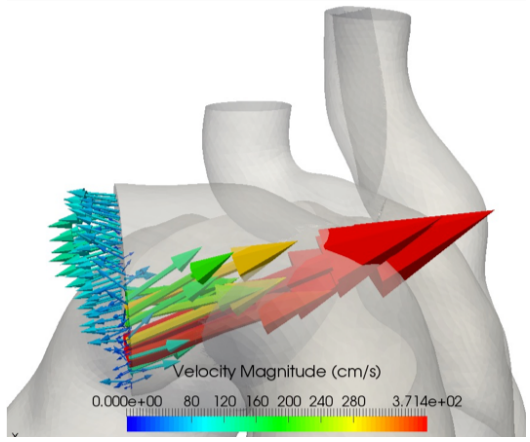

Figure 3.10: Test 3a: velocity vectors at the brachiocephalic artery at $t = 0.32\,\mathrm{s}$, shortly before the simulation crashes.

Numerical results

During the deceleration period following the peak systole, the flow is reverted at the brachiocephalic and left subclavian arteries. The backflow at these two branches causes instabilities for *Test 3a* and eventually makes the simulation crash. Therefore, backflow stabilization is necessary in order to obtain stable numerical results for this patient-specific case. The unstable velocity at the brachiocephalic artery occurring at $t = 0.32\,\mathrm{s}$ is shown in Fig. 3.10. *Test 3b* is numerically stable, indicating that the Leray-EFR model successfully suppresses the backflow instability. *Test 3c* is numerically stable too.

We compare the results of *Test 3b* and *3c*. The comparison of flow rate and average pressure at each outflow boundary (at the same locations) over time is shown in Fig. 3.11 and 3.12, respectively. First of all, from Fig. 3.11 we observe that the results from both *Test 3b* and *3c* capture the reverse flow at the brachiocephalic and left subclavian arteries at the end of systole. The two computed flow rates from *Test 3b and 3c* are consistent, following similar dynamics. The pressure at the supra-aortic branches of *Test 3b* is higher than *Test 3c*. Apart from these details, they follow similar dynamics. The flows rates from *Test 3b and 3c* are more in agreement then the pressures.

In Fig. 3.13 and 3.14, we report the velocity magnitude and vectors from *Test 3b* and

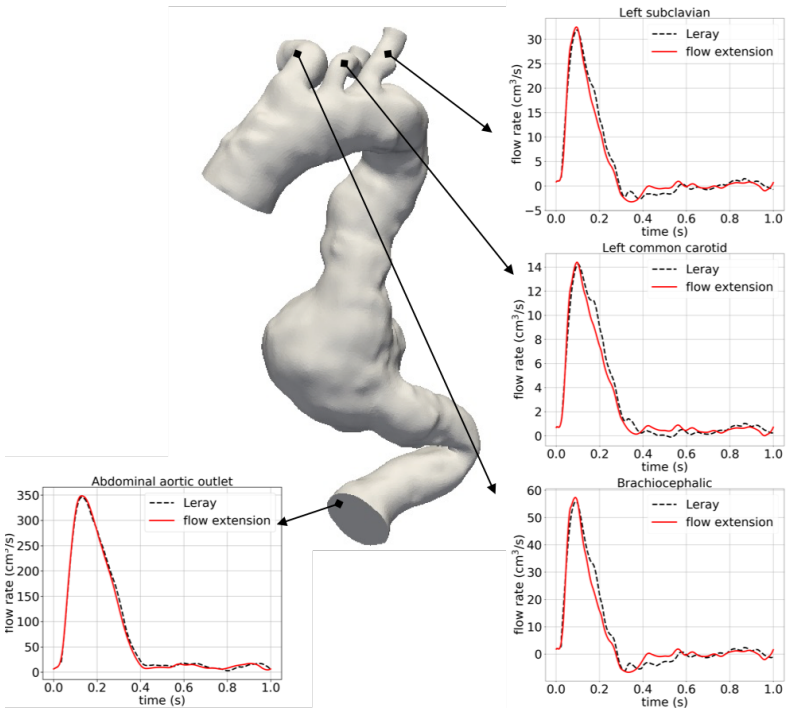

Figure 3.11: Test 3b (Leray) and 3c (flow extension): comparison of the computed flow rate at each outflow boundary over time.

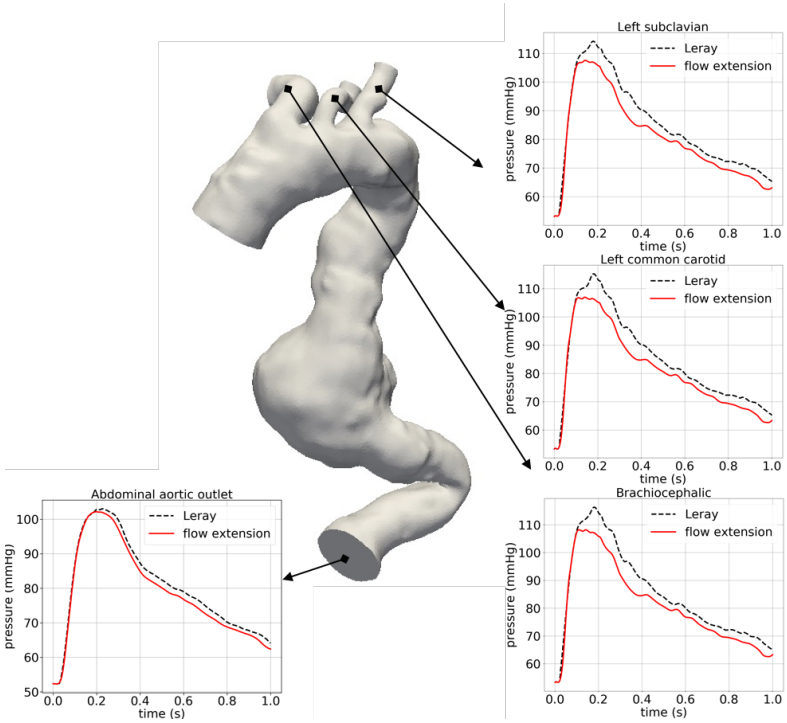

Figure 3.12: Test 3b (Leray) and 3c (flow extension): comparison of the average pressure at each outflow boundary over time.

3c at the brachiocephalic branch at time $t = 0.32\,\mathrm{s}$, which corresponds to the peak backflow. The stabilized velocity from both tests are qualitatively consistent, however their absolute magnitudes are not the same. We suspect that the velocity magnitude in *Test 3c* is smaller due to the artificial diffusion introduced by the streamline diffusion stabilization. In Fig. 3.15, the velocity vectors at the same branch are compared at time $t = 0.13\,\mathrm{s}$, which corresponds to the the peak forward flow. We observe that the velocity field at the brachiocephalic outflow is more uniform in *Test 3c* than expected in physiological conditions [115, 116, 117]. In fact, a physiological flow condition resembles flow in a curved pipe where secondary flow happens [118, 119] depending on different Dean numbers. The more uniform velocity is most likely an effect of the penalization on the velocity gradient introduced at the boundary.

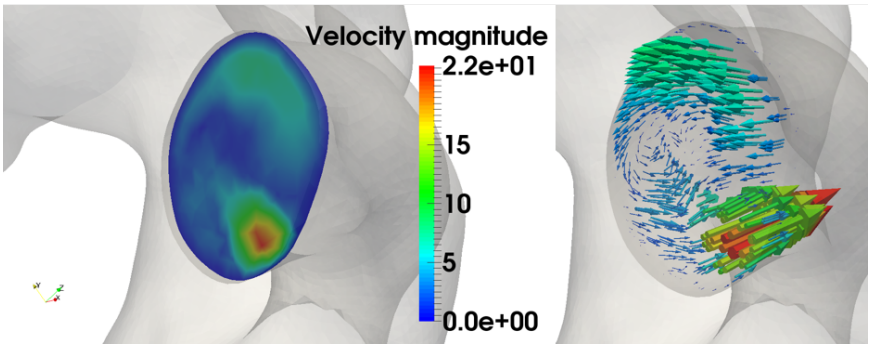

Figure 3.13: Test 3b: velocity magnitude (left) and velocity vectors (right) at the brachiocephalic branch at $t = 0.32\,\mathrm{s}$, which corresponds to the peak backflow.

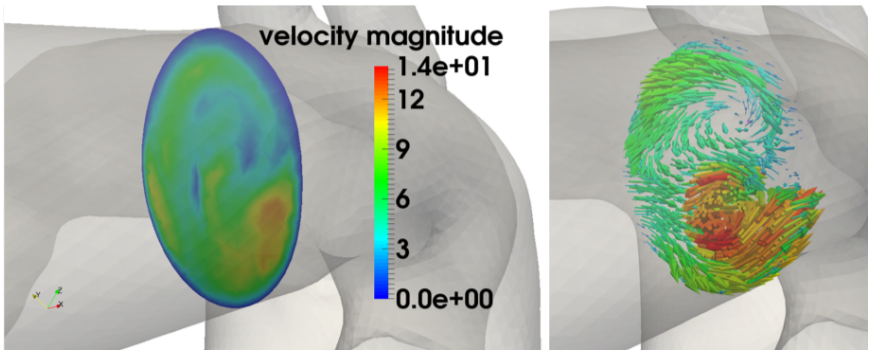

Figure 3.14: Test 3c: velocity magnitude (left) and velocity vectors (right) at the brachiocephalic branch at $t = 0.32\,\mathrm{s}$, which corresponds to the peak backflow.

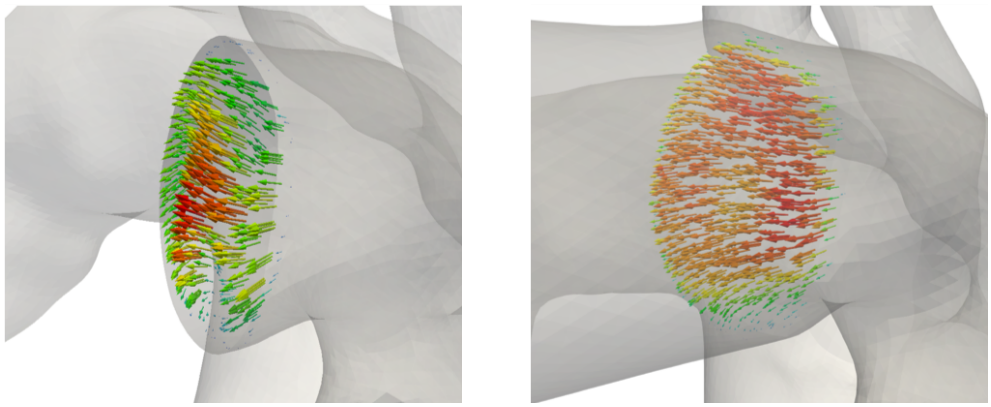

(a) *Test 3b* (b) *Test 3c*

Figure 3.15: Test 3b and 3c: velocity vectors at the brachiocephalic branch at $t = 0.13\,\mathrm{s}$, which corresponds to the peak forward flow.

The time averaged wall shear stress (TAWSS) is one of the clinical quantities of interest in understanding disease progression of abdominal aneurysm [120]. In Fig. 3.16, we compare the TAWSS computed from *Test 3b* and *Test 3c*. The distributions of the magnitude of TAWSS agree well qualitatively, in particular at the location of interest, i.e. the abdominal aneurysm. However, higher TAWSS is observed at the supra-aortic branches in *Test 3b*, which agrees with physiological conditions [55, 121].

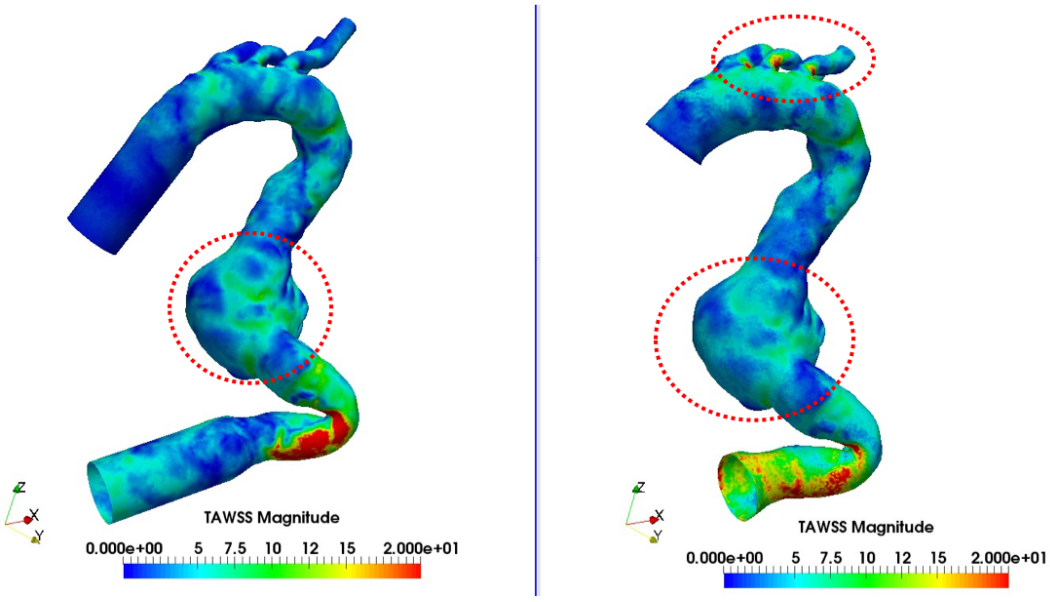

Figure 3.16: Test 3b and 3c: comparison of the TAWSS for *Test 3c* (left) and *Test 3b* (right).

3.4 Discussion and Summary

This work originates from a long-term experience in computational hemodynamics, applied to patient-specific settings. The gap between theory and practice in this context [35] challenges both accuracy and efficiency of numerical tools used for the clinical practice. One of the most problematic aspects is the boundary conditions.

The access to data to use for boundary conditions is prevented by practical and ethical issues, while there is abundance of images to reconstruct the morphology (the so called *"image-legacy" problem*). This leads to the introduction of simplified models to retrieve boundary data (see, e.g., [37]) without impairing the reliability of the simulations. On the other hand, homogeneous Neumann conditions, i.e., "do-nothing" conditions [33], are typically set in the absence of alternatives. This is due to the fact that Neumann conditions are generally less invasive on the numerical solution, being "natural" to a given differential problem (in its variational form). This has some drawbacks, particularly for the stability of the physical problem and its numerical consequences. The flow reversals occurring in some vascular districts, like the aorta, call for stable solvers.

Stability can be achieved by modifying the domain of interest, with the introduction of the so called *flow extensions*, that damp the incoming energy carried in by the flow. This solution - used also for flow rate conditions at the inflow to prescribe the arbitrary velocity profile far away from the region of interest - is highly empirical and, in spite of its relative conceptual simplicity, requires the construction of alterations of the domain of interest that are not always easy [92]. Artifacts may be introduced by an imperfect alignment of the extensions with the centerline of the region of interest. In any case, flow extensions require additional degrees of freedom in the computation, inducing an extra computational cost. For instance, in our numerical experiment *Test 3b*, the CPU time per time step is about 30% of the CPU time per time step required by *Test 3c* with the same computational power (4 cores, i.e. 192 nodes, on the Extreme Science and Engineering Discovery Environment

stampede2 [122]), due to the extra DOFs introduced by the flow extensions.

Another way for damping the incoming energy is the use of Robin conditions [46, 103], which is conceptually similar to the flow extension, but with no additional computational effort. It is worth noting that Robin-like conditions (advocated also for the well posedness of geometrical multiscale models [123]) for Navier-Stokes problms are not standard and may require specific coding; moreover, the fine tuning of the resistance needs physical and/or numerical arguments. Other more sophisticated approaches have been considered in [42, 44, 45, 102, 101].

This paper stems from the practical observation that adding a specific modeling of unresolved scales like the Leray-Deconvolution approach formulated according to the EFR scheme in aortic simulations rarely suffered from the instability due to the flow reversal. While the aortic flow (Reynolds number of the order of few thousands) is amenable to direct numerical simulations, the large volume of clinical data we are considering [39, 37] suggests the introduction of an efficient modeling at relatively coarse mesh discretizations, while guaranteeing a level of accuracy relevant to the clinical practice. From this perspective, LES modeling provides an excellent trade-off between accuracy and efficiency required by patient-specific settings in computer-aided clinical trials. With this motivation, we discovered that our LES modeling may control any backflows and in this paper we provide a rigorous proof and extensive numerical evidence. While not all the simulations in computational hemodynamics suffer from flow reversal, aorta is one of the districts interested by this phenomenon. In favor of our LES approach, we prove here this serendipity circumstance that fixes the need of modeling unresolved scales and the backflow instability at once ("two birds with one stone").

On the choice of the stabilization parameters. Our Theorem is based on energy considerations and a continuity argument with respect to the parameters, particularly the relaxation parameter χ. Unfortunately, our proof does not give specific recipes for calibrating

model parameters χ and δ. This attains to an extensive sensitivity analysis of the role of χ and δ that is a work in progress [64, 124]. In [64], the sensitivity analysis on δ (therein called α) suggests that the velocity computed by our scheme does actually depend on δ in a nonuniform problem-dependent way, so that the selection of the radius may be based on the mesh size in a conservative sense, possibly corrected by some adaptive strategies. In [124], the interplay between the radius and other possible data affecting the results is investigated using Polynomial Chaos Expansion based Sobol' Indexes, specifically for hemodynamics problems. The results show that the choice of δ has an impact only in some specific parts of the heart beat (the diastolic phase) and, in any case, is definitely less impactful than the geometry of the computational domain. These analyses pinpoint the need for further investigations, that are expected to be largely problem-dependent.

Our results empirically led us to some practical guidelines:

1. Selecting δ proportional to h_{min} is generally a recommended strategy, possibly to be corrected in an adaptive fashion with the solution of a sensitivity problem as suggested in [64] and in particular during the phases of the simulation (like, e.g., during the diastole) when the solution is significantly affected by the filter radius (as noted in [124]).

2. It is argued for the turbulence modeling that χ should be proportional to Δt. However, suppression of backflow instability is not related to the time-discretization, so the combination of the stabilizing effects calls for a sub-linear dependence on the time step.

3. Generally, a small filter radius (for instance for a fine mesh) calls for a larger relaxation parameter (and vice-versa). However, backflow stabilization requires some relaxation ($\chi > 0$) even for a large radius δ.

Setting up adaptive strategies will be subject of future developments. As a rule-of-thumb, in our next applications of this solver for aortic simulations (following up [39])

we plan to select $\delta = h_{min}$ and to adjust manually or adaptively χ to prevent instabilities, starting from a tentative value of $\chi \approx f\Delta t$, where f is a problem-dependent factor.

CHAPTER 4

UNCERTAINTY QUANTIFICATION AND SENSITIVITY ANALYSIS

4.1 Motivation

Uncertainties affect the reliability of the numerical simulation of hemodynamics in patient-specific settings and rigorous Uncertainty Quantification (UQ) is in order. This Chapter presents a UQ study on the aorta flow, for assessing the sensitivity of the clinical relevant quantities to the morphology and imprecise knowledge of the boundary condition using the Polynomial Chaos Expansion (PCE) based Sobol' indices. Specifically, we focus here on (i) the variation of the geometry of the patient-specific aorta reconstructed from medical images; (ii) the inflow boundary condition. The geometrical uncertainty is modeled based on a set of *longitudinal* imaging data of a patient with the abdominal aortic aneurysm. The images of the patient's aorta at different stages of the disease are used to create a map that drives the realistic variation of the reconstructed morphology. The aorta is a peculiar site for hemodynamics, since the flow is highly disturbed due to the high Reynolds number during systole, and the modeling of turbulence helps to avoid the high computational costs. Large Eddy Simulation (LES) modeling was considered in the past for these simulations. LES models feature problem-dependent numerical parameters to tune. We borrow the same UQ tools used for physical uncertain quantities to assess the sensitivity of the simulations to one of these numerical parameters in the LES model, the *filter radius*. The sensitivity of the total kinetic energy (TKE), the time average wall shear stress (TAWSS) and the oscillatory shear index (OSI) are analyzed. The results show that the geometry has the most dominant contribution to the uncertainty of all the quantities of interest (QoIs). The sensi-

The work of Chapter 4 is publsihed in Xu et al., Global sensitivity analysis of the nonlinear leray model using the polynomial chaos expansion based sobol' indices. Journal of biomechanical Engineering, 2019. (Under review)

tivity analysis provides confidence intervals for the simulations that quantify the reliability of the numerical predictions.

4.2 Case Studies

4.2.1 Two cases

The study is carried out on an idealized aortic arch and a patient-specific aorta with the degenerated Abdominal Aortic Aneurysm (AAA). The methods of PCE and Sobol' indices are detailed in Sec. 2.2.

The idealized aortic arch. As a proof of concept, the impact of the filter radius δ and inflow rate $Q(t)$ are firstly investigated in a simplified aortic arch (Fig. 4.1). The geometry is composed of a half torus and two cylinders. The detailed dimensions are shown in Fig. 4.1. In this case, we do not test the uncertainty for the geometry. The stochasticity of the inflow and the filter radius are detailed below.

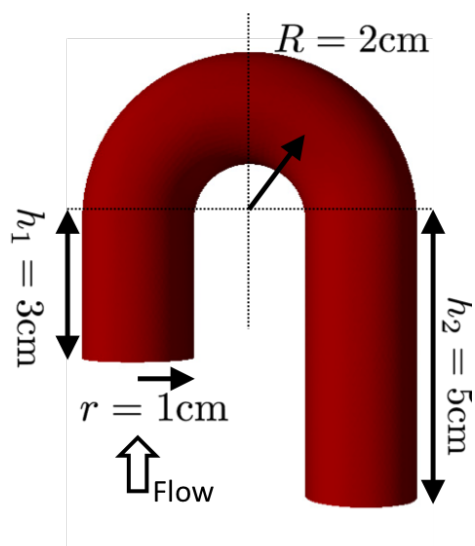

Figure 4.1: The simplified aortic arch and its dimensions.

The patient-specific abdominal aortic aneurysm. In addition to the filter radius δ and inflow rate $Q(t)$, uncertainty in the geometry is investigated by considering a patient-

specific case of the degenerated AAA with the longitudinal imaging data. Two sets of CT images, from 2010 and 2016 respectively, of the diseased aorta from this patient were retrieved from the iCardioCloud Project supported by the Cariplo foundation (No. 2013−1779). The patient had a significant abdominal aortic dilation from 2010 to 2016, as shown in Fig. 4.2. The modeling of the geometrical uncertainty utilizing this set of longitudinal image data is detailed in the flowing section.

4.2.2 Uncertain inputs

Due to the lack of the data representing a large cohort of patients, we need to postulate *a priori* stochastic descriptions on the inputs under consideration. It is important that - even if simplified due to the lack of data representing the population- these descriptions are consistent with the real problem at hand. This is particularly challenging for the vascular geometry, since deformations implied by the probability density function need to be reasonable. Our approach is detailed below and the specific stochastic features is listed in Tab. 4.1.

Uncertainty in the aneurysmal geometry. In order to obtain in the stochastic description of a deformation field consistent with physiological deformations, we introduce a novel approach based on a longitudinal data set in which snapshots available for a patient at instants corresponding to different stages of the aneurysm. Specifically, the reconstructed initial (2010) and follow-up (2016) aortas from CT scans using the vascular modeling tool kit (detailed in Sec. 2.3.1) are shown in Fig. 4.2. The three-dimensional deformation field $D(\mathbf{x})$ quantifying the degeneration of the abdominal aneurysm is computed by the *image-registration* procedure detailed in Sec. 2.3.3. The follow-up geometry (Fig. 4.2 right) is mapped to the initial one (Fig. 4.2 left) using an non-rigid registration method [97]. Once the deformation map D is computed, it is scaled by a uniformly distributed univariate random variable $\xi_G \sim \mathcal{U}[0,1]$ to represent the uncertainty in the morphology. The resulting

Table 4.1: Uncertain inputs and their distributions. Here $\mathcal{N}(\mu, \sigma^2)$ denotes the normal distribution with the mean of μ and variance of σ^2, while $\mathcal{U}[a, b]$ denotes the uniform distribution with the support being $[a, b]$.

Uncertain inputs	Distribution	Polynomial chaos
ξ_δ	$\mathcal{N}(h_{min}, (25\% h_{min})^2)$	Hermite
ξ_Q	$\mathcal{N}(1, 10\%^2)$	Hermite
ξ_G	$\mathcal{U}[0, 1]$	Legendre

uncertain geometry is $G(\mathbf{x}, \xi_G) = G_{initial}(\mathbf{x}) + \xi_G \times D(\mathbf{x})$, where the local uncertain deformation of the aneurysm is assumed to be a fraction the total deformation of the lumen to the follow-up stage. At the best of our knowledge, it is the first time that UQ on geometry is conducted by using a longitudinal data set and a registration method.

Uncertainty in the inflow rate. The uncertainty in the inflow rate due to the lack of patient specific data is modeled by scaling the patient's aortic inflow $q(t)$ (Fig. 4.3) by a normally distributed univariate random variable $\xi_Q \sim \mathcal{N}(\mu_Q, \sigma_Q^2)$, where $\mu_Q = 1$ and $\sigma_Q = 0.1$. Therefore we have the resulting inflow rate $Q(t) = q(t)\xi_Q$. In absence of more specific information, the Gaussian (normal) distribution is the method of choice.

Uncertainty in the filter radius δ. The filter radius δ is modeled as a normally distributed univariate random variable $\xi_\delta \sim \mathcal{N}(\mu_\delta, \sigma_\delta^2)$ with mean being the minimal mesh size $\mu_\delta = h_{min}$ and standard deviation being $\sigma_\delta = 25\% \mu_\delta$.

4.2.3 Model responses (outputs)

The model responses considered here are the TKE, TAWSS and OSI. The definition of TAWSS and OSI are detailed in Sec. 2.3.4. The TKE is defined here as

$$TKE \equiv \frac{1}{2} \int_\Omega \rho \mathbf{u} \cdot \mathbf{u} d\Omega$$

Figure 4.2: Initial (left: acquired at 2010) and follow-up (right: acquired at 2016) aortic geometries of a patient with the abdominal aortic aneurysm.

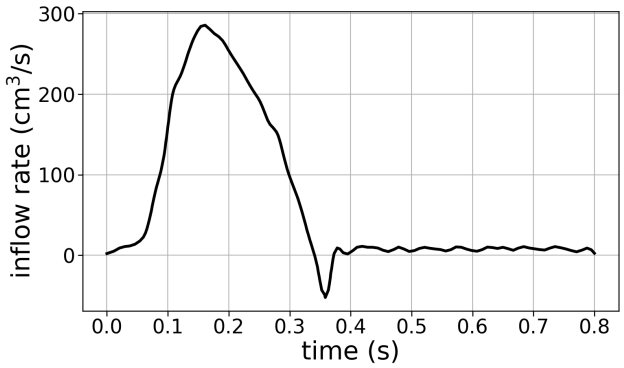

Figure 4.3: The mean inflow rate.

where Ω represents the whole computational domain.

The mean and variance of these QoIs are computed as well as the corresponding Sobol' indices to quantify the relative contribution of different uncertain inputs to the uncertainty of QoIs.

4.3 Results

4.3.1 Results on the idealized aortic arch

As a proof of concept, the impact of the filter radius $\delta = \xi_\delta$ and inflow rate $Q(t) = q(t)\xi_Q$ are investigated in a simplified aortic arch (Fig 4.1). Details of the random input parameters are listed in first two rows of Tab. 4.1.

The truncated PCE approximations of the total kinetic energy, TAWSS are computed with polynomial basis of degree $p = 2$ and $p = 3$. The stochastic modes are approximated using the non-intrusive pseudo-spectral method [88] (as detialed in Sec. 2.2) with the Leja [125, 91] nested sparse grid quadrature points, shown in Fig. 4.4. The numbers of simulations required are 15 and 21, respectively. The difference between the results from the PCE of degree $p = 2$ and $p = 3$ are negligible.

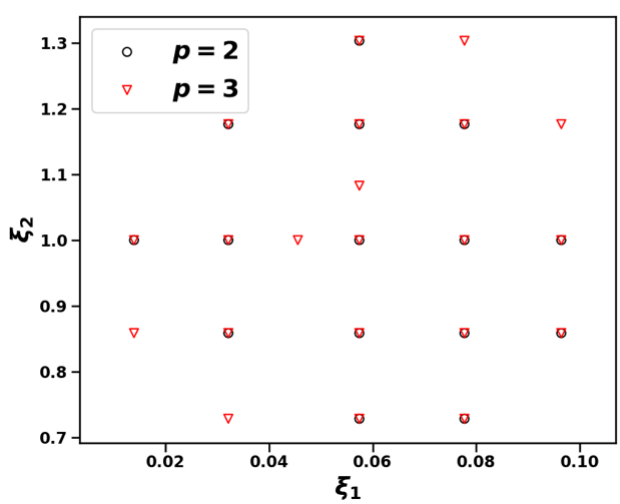

Figure 4.4: The Leja sparse quadrature points for PCE of degree two and three with the two dimensional input parameter space.

The mean, variance and prediction interval of the total kinetic energy for the simplified aortic are shown in Fig. 4.5. The Sobol' indices for the total kinetic energy is shown in Fig 4.7 (left).

The mean, variance and prediction interval for TAWSS are shown in Fig. 4.6, while the Sobol' indices for TAWSS is shown in Fig 4.7 (right).

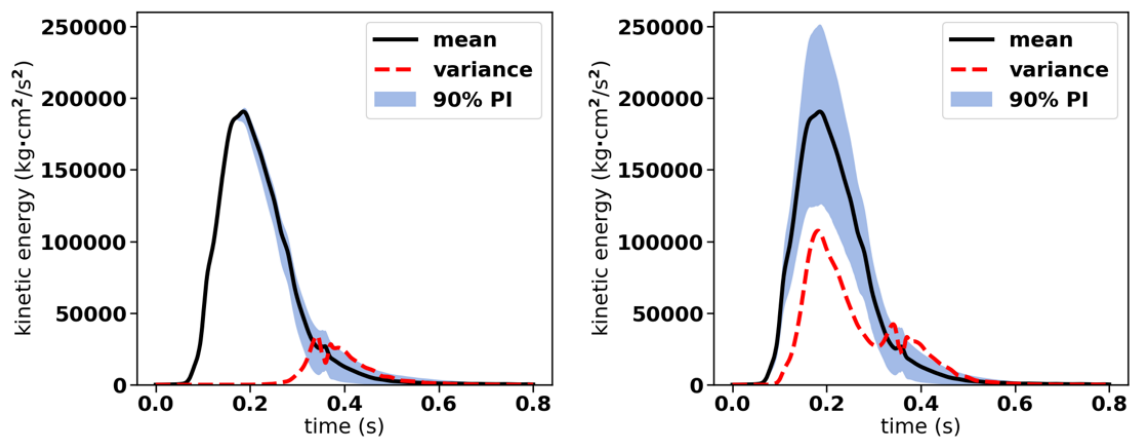

Figure 4.5: The mean, variance, 90% prediction interval for the total kinetic energy in the simplified aortic arch. Only the uncertainty of the filter radius δ is considered in the left plot; The uncertainty of both the filter radius δ and inflow rate $Q(t)$ are considered in the right plot.

4.3.2 Results on the patient-specific AAA

The truncated PCE approximations of the total kinetic energy, TAWSS and OSI are computed with PCE of degree $p = 2$. The stochastic modes are approximated using the non-intrusive pseudo-spectral methods with the Leja nested sparse grid quadrature points. The resulting number of simulations required is 35. The aortic geometries based on the quadrature points for ξ_G are shown in Fig. 4.8.

The mean and Coefficient of Variation (CoV) for the TAWSS (top row) and OSI (bottom row) are shown in Fig. 4.9. The Sobol' indices for the total kinetic energy, TAWSS and OSI are reported in Fig. 4.10 and 4.11, respectively.

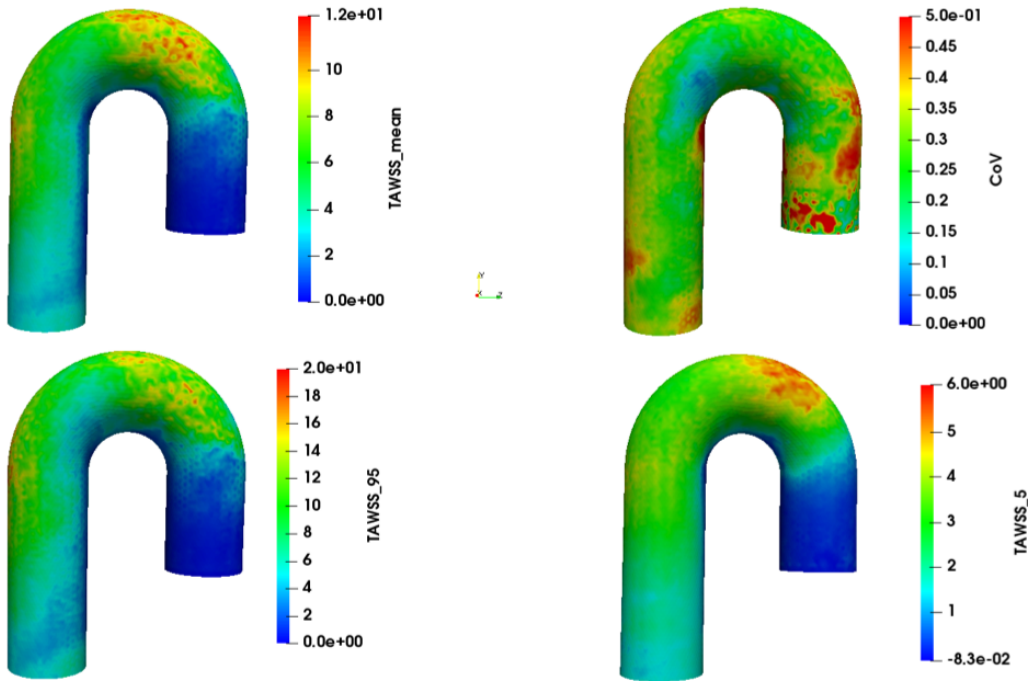

Figure 4.6: Mean, coefficient of variation, $95th$ percentile, $5th$ percentile of TAWSS of the simplified aortic arch.

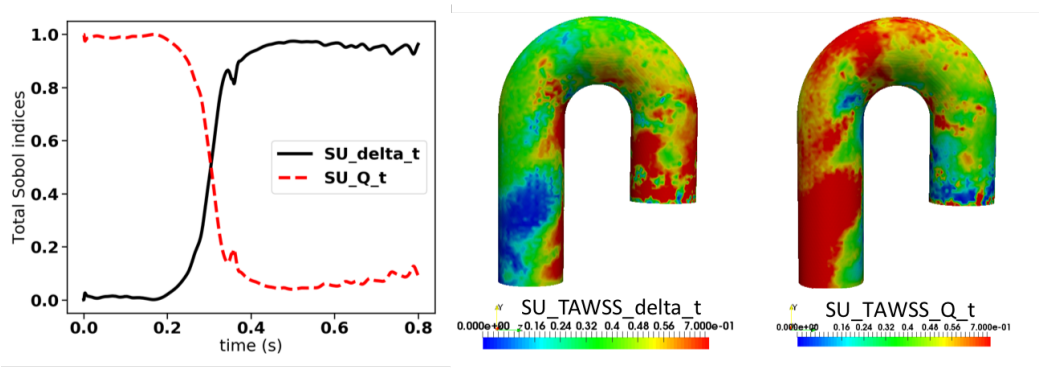

Figure 4.7: Sobol' indicies of filter radius and inflow for TKE (left) and TAWSS (right). SU_delta_t and SU_Q_t denote the total Sobol' index of the filter radius δ and inflow for TKE respectively. $SU\_TAWSS\_delta\_t$ and $SU\_TAWSS\_Q\_t$ denote the total Sobol' index of δ for TAWSS and inflow for TAWSS respectively.

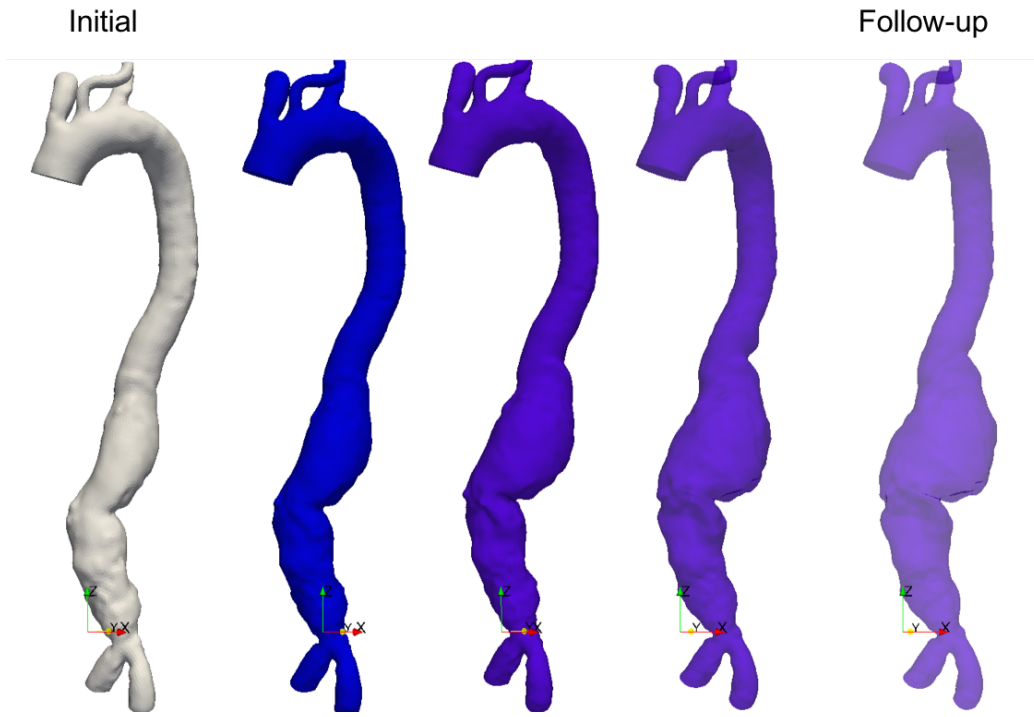

Figure 4.8: The Sampled AAA geometries corresponding to the five quadrature points of ξ_G.

4.4 Discussion and Summary

4.4.1 The idealized aortic arch

The variance of the TKE caused by the variation of the filter radius δ during the systole (from 0 to 0.3 seconds) is minimal, while the influence of the filter radius is evident during the diastole, as shown in Fig. 4.5 (left). However, the impact of the inflow is much higher than that caused by δ, as shown in Fig. 4.5 (right).

Sobol' indices for the TKE. The relative influence of the variations of the filter radius δ as well as the inflow boundary condition on the hemodynamic factors of this simplified aortic arch are investigated using the Sobol' indices. Consistent with the variance results (in Fig. 4.5), the Sobol' index of δ with respect to time in Fig 4.7, which represents the contribution to the variation of the TKE during the systolic phase from δ, is much lower than that from the inflow rate, despite the higher coefficient of variation of δ. This demon-

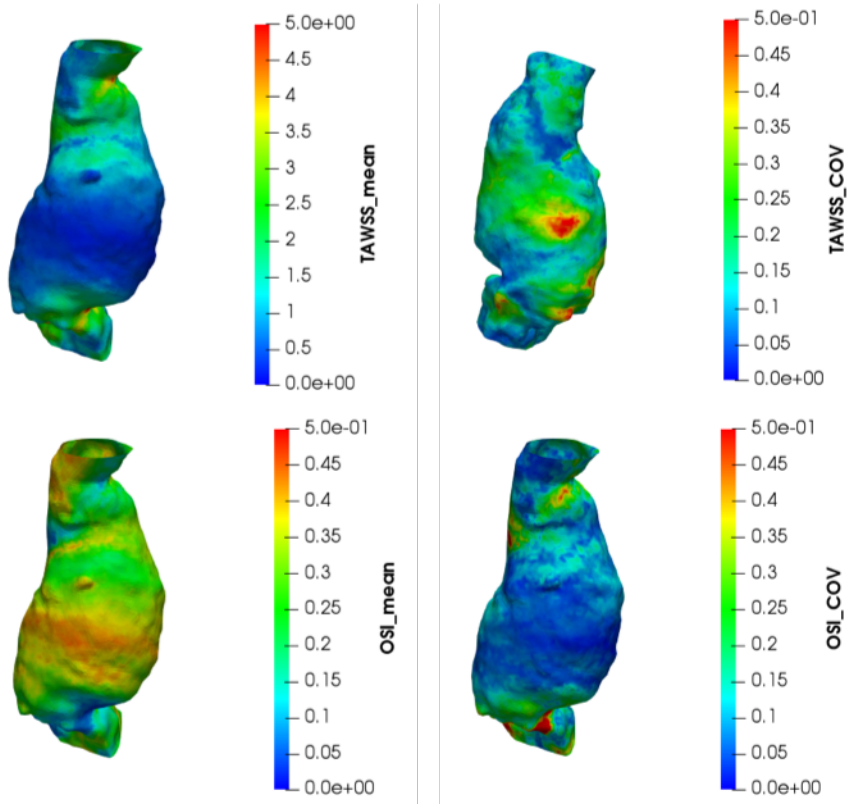

Figure 4.9: Mean and coefficient of variation of TAWSS (top) and OSI (bottom) for the patient-specific AAA case.

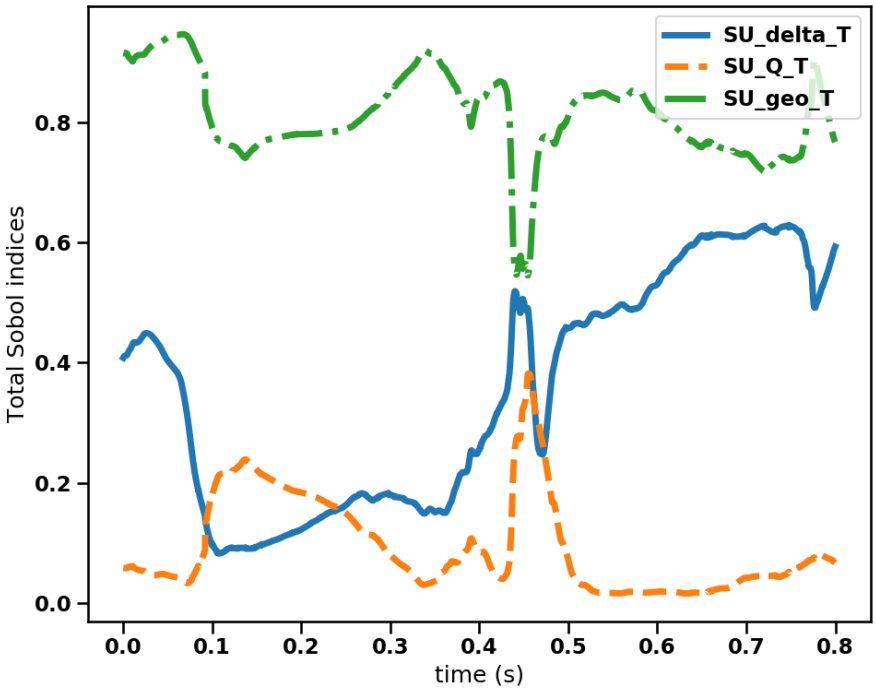

Figure 4.10: Sobol' indices for the TKE for the patient-specific AAA case. (SU_delta_T, SU_Q_T and SU_geo_T represent the total Sobol' indices of δ, inflow and geometry, respectively.)

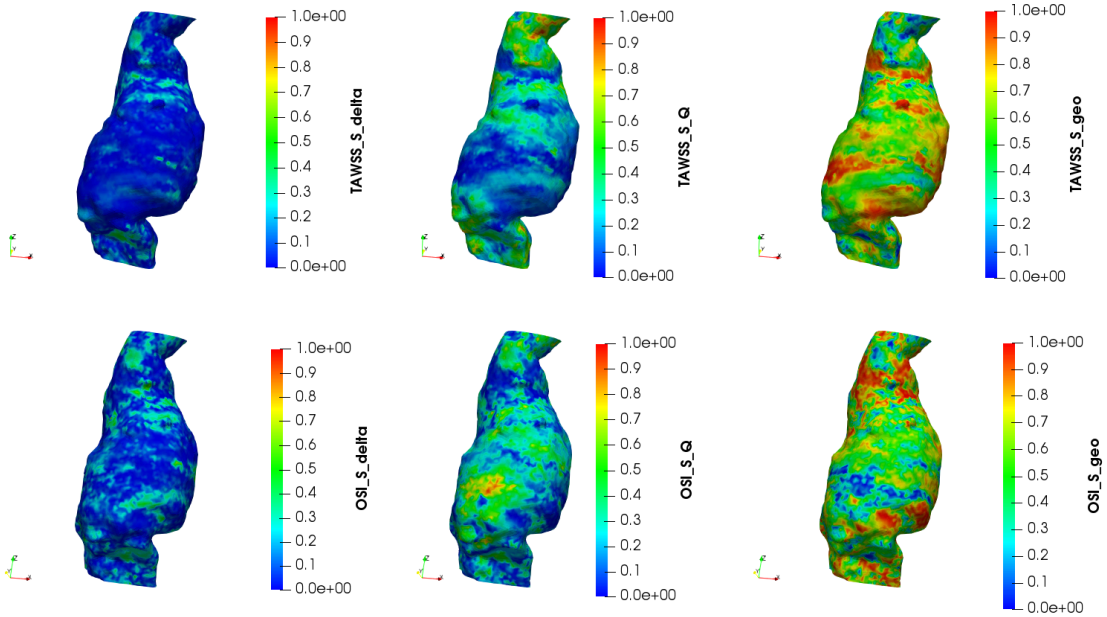

Figure 4.11: Sobol' indices for TAWSS (top row) and OSI (bottom row) for the patient-specific AAA case.

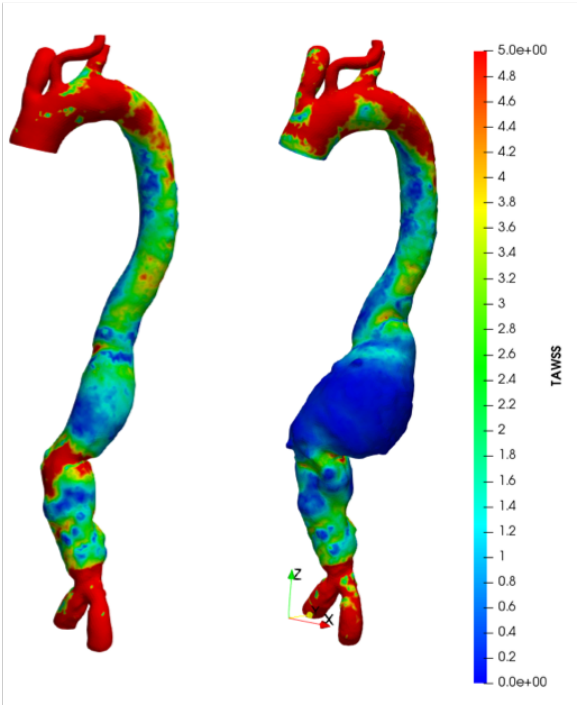

Figure 4.12: TAWSS for the extreme geometries $\xi_G = 0$ (left) and $\xi_G = 1$ (right) for the patient-specific AAA case, when $\xi_\delta = \mu_\delta$ and $\xi_G = \mu_G$.

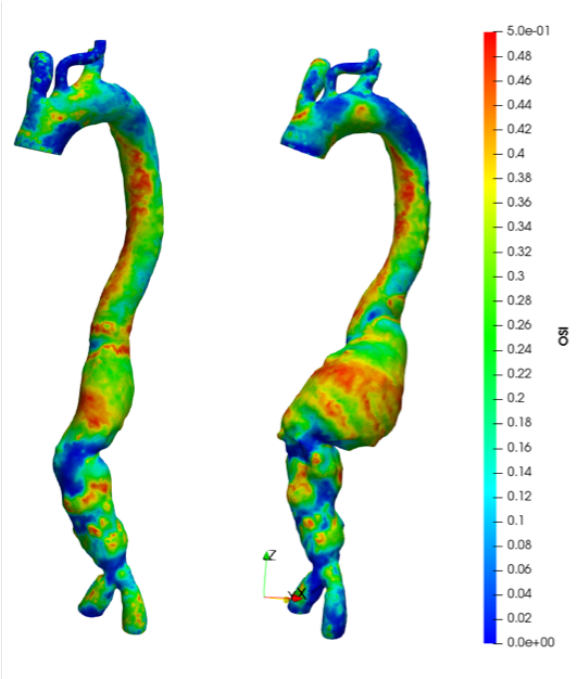

Figure 4.13: OSI for the extreme geometries $\xi_G = 0$ (left) and $\xi_G = 1$ (right) for the patient-specific AAA case, when $\xi_\delta = \mu_\delta$ and $\xi_G = \mu_G$.

strates the robustness of the model during systole. However, the influence of δ exceeds that of the inflow rate during diastole.

For TAWSS, the Sobol' index of δ is lower than that of the inflow in most region of the arch, except for the inflow region and the interior of the arch. The higher Sobol' index of δ in these regions might be due to the influence of the δ during diastolic phase.

4.4.2 The patient-specific AAA case

The mean TAWSS is lower in the region with more growth comparing to other region on the aneurysm. It is contrary for the results of OSI, for which relatively higher OSI are observed in the region with more growth. More interestingly, the CoV for TAWSS is higher in the region with more growth (i.e. region with relatively low mean TAWSS), while the opposite result is observed from OSI.

Sobol' indices for the TKE. The Sobol' indices of the filter radius δ, inflow rate as well as the abdominal aneurysmal geometry with respect to the TKE are shown in Fig. 4.10. The result regarding the relative contribution from the filter radius and inflow rate is consistent with the finding from the simplified aortic arch, i.e. the inflow rate has relatively more contribution to the total variation during systole while the filter radius is more influential than inflow rate during diastole. However, the variation of the abdominal aneurysmal geometry of the aorta has a significantly dominant role for the uncertainty of the TKE through out the whole cardiac cycle. The partial variance caused by the variation in the geometry is larger than those caused by the other two factors combined, as shown in Fig. 4.10.

Sobol' indices for the TAWSS and OSI. The Sobol' indices of the filter radius δ, inflow rate as well as the abdominal aneurysmal geometry with respect to TAWSS and OSI are shown in Fig. 4.11. Consistently with the results for the TKE, the relative contribution of the three investigated factors (ranked from high to low) to both TAWSS and OSI: the aneurysmal geometry, the inflow rate and the filter radius. The TAWSS of the two extreme

quadrature points for ξ_G is shown in Fig. 4.12 and OSI is shown in Fig. 4.13. The filter radius and inflow rate are kept at their mean values, respectively. It is shown that the TAWSS and OSI changes significantly with the changing of the aneurysmal geometry even when the other two factors are kept the same.

4.4.3 Limitations

The work bears some limitations as listed below.

1. Due to the constraint of computational costs, only three sources of uncertainty are considered simultaneously in this study.

2. Simplified models are assumed for the uncertainty in the inflow boundary condition due to the lack of access of patient-specific data of a large population.

3. In the simulations, the arterial wall is assumed to be rigid and the flow is assumed to be Newtonian.

Limitations (1) and (2) will be addressed in future works, while we speculate that the limitations in (3) have a minor impact in the conclusions of the present study. We argue that the qualitative conclusions drawn from the results here, particularly in terms of prioritizing the impact of the different uncertainties hold despite of these limitations.

CHAPTER 5

PATIENT-SPECIFIC STUDY OF AORTIC DISSECTIONS

5.1 Motivation

Progressive false lumen aneurysmal degeneration in type B aortic dissection (TBAD) is a complex process with a multi-factorial etiology. As several groups have pointed out in their studies of acute uTBAD, it is necessary to consider both hemodynamic factors as well as the morphological ones to obtain clinical relevant conclusions on the prognostic factors of the false lumen degeneration [22, 126, 127, 128, 129, 23, 94, 24]. These studies focused upon the impact of hemodynamics on FL degeneration in patients with TBAD. The effect of Wall Shear Stress (WSS) related factors [22, 21, 126, 23], percentage of blood flow passing through the FL [22, 21, 20], the size and location of entry tears [21, 15], the pressure difference between the true and FLs [23, 24, 130], and also the Relative Residence Time (RRT) of flow inside of the FL [128, 24] have been studied. However, only simplified and localized measurements were used in quantifying the FL evolution. Moreover, the correlations between hemodynamic quantities and morphological changes of the FLs were based on observational instead of quantitative analysis, e.g. relatively lower time averaged wall shear stress was observed in the enlarged FLs of the post-aneurysmal aortas than those of the pre-aneurysmal aortas.

This Chapter first focuses on a single patient with a longitudinal imaging data for a comprehensive correlation analysis between morphological and functional (hemodynamics) factors. Then a cross-sectional study involves multiple patients are carried out for a further investigation. In comparison with previous studies, this work brings novelty in

The work of Chapter 5 is published in Xu et al., Coupled morphological–hemodynamic computational analysis of type b aortic dissection: A longitudinal study. Annals of biomedical engineering, 46(7):927–939, 2018.

three aspects:

- The entry tear and the complex morphology trigger flow acceleration and disturbances that challenge the numerical solution. Even if it is generally a non-turbulent flow, very fine mesh scales are typically required, which are unsuitable for large clinical studies. To combat this, the Leray-EFR model is applied the first time in hemodynamic applications and its efficacy is demonstrated.

- Quantification of the FL evolution is not based on a localized measure such as the maximum diameter or an averaged measure like the FL volume. Instead, registration methods are used to give a comprehensive 3D quantification of the aneurysmal growth.

- For the clinical cases in this study, patient-specific measurements to be used for the boundary conditions are missing. This is a common problem in retrospective clinical computational hemodynamics known as "image-legacy problem", as neither the flow or pressure data are often not recorded together with the images. A method is developed in this work that calibrates the parameters of a classical 3WK model at the outflows with the flow splitting derived from patient-specific morphology using the well-known Murray's Law. In this approach, the Murray's law is the key to convert the morphological patient-specific data into hemodynamic ones.

5.2 A Longitudinal Study - A Single Patient

A 60-year-old female was diagnosed with uTBAD in Emory University Hospital (EUH) in 2006 and treated with OMT. However, during the following four years under OMT since 2006, her FL kept dilating and she eventually received open surgery in 2010 because that her FL reached the critical size and was at a high risk of rupture. This is a typical case of original uTBAD that developed the late complication of the FL aneurysmal degeneration. The computed tomography angiography (CTA) was obtained in 2006 and 2010 (initial vs.

follow-up), respectively. The initial and follow-up geometries of this patient's aorta were reconstructed from the CTA using the method described in Section. 2.3.1, as shown in Fig. 5.1. To investigate the prognostic factors of FL degeneration for this TBAD patients, hemodynamics in the dissected aortas are simulated by Leray-EFR model and 3D deformation field representing the FL degeneration are quantified by the non-rigid Point Set Registration (PSR) method, detailed in Section. 2.3.3. Finally, the TAWSS, OSI, as well as RRT are correlated with the FL deformation using Pearson correlation coefficients to identify the indication factor of FL dilation.

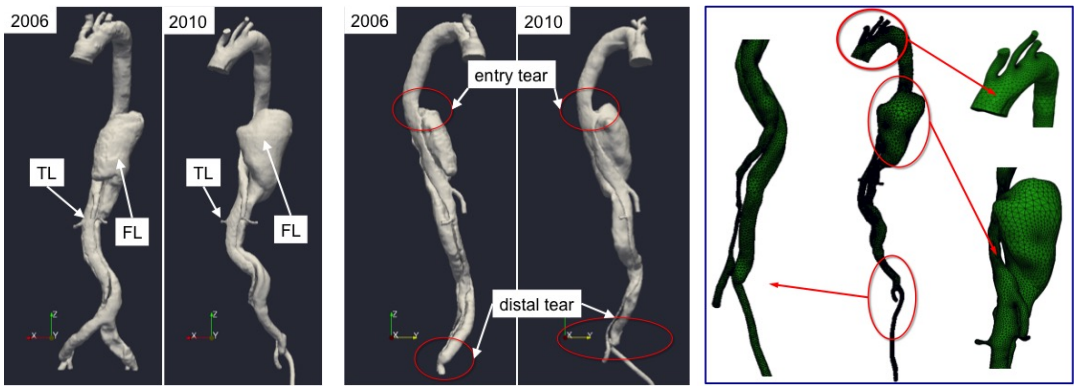

(a) front view (b) lateral view (c) mesh of geometry at 2010

Figure 5.1: Geometry reconstruction of the dissected aorta of an anonymized patient from EUH. This patient was diagnosed with uTBAD in 2006 and later cTBAD in 2010. The CT angiography was performed at both times. (a) and (b) are front and lateral views, respectively, of the reconstructed geometries using VMTK. The entry and distal tears of the FL at 2006 and 2010 are highlighted in red circles. (c) demonstrates the tetrahedral spatial discretization performed for geometry at 2010 using NETGEN.

5.2.1 Geometries of the initial and follow-up aortas

Patient specific aortas of initial and follow-up cases, from the sinotubular junction to the iliac bifurcation, were reconstructed from CTA images, as shown in Figure 5.1a and 5.1b. Initially in 2006, this patient had a relatively small patent FL starting from descending thoracic aorta and extending to left and right common iliacs, as shown in 5.1b. However, the dissected aorta remodeled over 4 years after 2006, with enlarged entry tear (0.55 cm

Table 5.1: Geometrical changes of the dissected aorta between the initial and follow-up image acquisition. The perimeter and hydraulic diameter are in cm and cross-section area is in cm^2.

Location	Geometry parameters		
	Perimeter (2006, 2010)	Cross-section area (2006, 2010)	Hydraulic diameter (2006, 2010)
Ascending aorta	(8.35, 9.29)	(5.48, 6.63)	(2.63, 2.86)
Desending Thoracic	(7.43, 7.73)	(4.36, 4.70)	(2.34, 2.43)
Brachiocephalic	(2.80, 2.96)	(0.60, 0.69)	(0.86, 0.93)
Left common carotid	(1.88, 1.94)	(0.41, 0.29)	(0.58, 0.59)
Left subclavian	(2.30, 2.14)	(0.41, 0.36)	(0.72, 0.67)
Mensenteric artery	(2.04, 2.29)	(0.32, 0.41)	(0.63, 0.72)
Left renal	(1.41, 1.41)	(0.15, 0.15)	(0.44, 0.42)
Right renal	(1.45, 1.10)	(0.16, 0.09)	(0.44, 0.32)
Left common iliac	(2.45/1.88, 2.00)	(0.47/0.28, 0.31)	(0.77/0.59, 0.63)
Right common iliac	(2.67/2.18, 2.46)	(0.56/0.37, 0.48)	(0.83/0.69, 0.77)

vs. 1.28 cm in diameter), significant aneurysmal dilation of FL (maximum diameter 5.09 cm vs. 7.76 cm) as well as changes at the iliac bifurcation, as shown in Figure 5.1b. The original two distal tears at the left and right common iliacs disappeared over the time period and the FL reconnected back through a single distal tear. During the remodeling, cross sections of major proximal branches increased in general. The distal branches, on the other hand, decreased. Detailed geometric information of each major aortic branch,including cross-section area, perimeter as well as hydraulic diameter, are listed in Table 5.1.

5.2.2 Quantification of the false lumen aneurysmal dilation

The non-rigid Point Set Registration method based on a probability regression advocated in [97] detailed in Sec.2.3.3 is adopted to automatically co-register the initial and follow-up FL geometries. In fact, this method is capable of finding both the non-rigid transformation and correspondence between two geometries without making any prior assumptions of any of them - so to apply to many possible different shapes. It also utilizes a regularization based on filtering displacement field during the transformation to preserve the topological structures of the FL.

An initial rigid registration was performed in order to pre-align (i.e. to eliminate the influence of the rigid body transformation) the two geometries and facilitate the registration of the aneurysmal dilation, as shown in Figure 5.2a. Then the registration method matched the Gaussian Mixture Model (GMM) centroids (representing the initial case) to the data (representing the follow-up case) by maximizing the likelihood, such that a correspondence could be assigned between the FL at the initial and follow-up stages, as shown in Figure 5.2b. Three free parameters w, β and λ in the algorithm represent the assumption on the amount of noise, smoothness of the coherence motion regularization as well as the trade off between the goodness of fit and regularization, respectively. Their values were set as $w = 0.1$, $\beta = 2.0$ and $\lambda = 2.0$ based on the test cases shown in the literature [97]. Following the registration result, a three-dimensional deformation field representing the evolution of FL from initial to follow-up state were then computed, as shown in Figure 5.2c. Different values of parameters were tested ($\beta, \lambda \in [1.0, 10.0]$) and registration results were found not sensitive to the parameters in this interval for the FL geometries.

The registered FLs are shown in Figure 5.2b. The 3D deformation field between the initial and follow-up FLs is shown in Figure 5.2c. The spatial maximum expansion was 2.29 cm, collocated with the spot of the largest diameter of the follow-up FL. The maximum dilation rate (averaged over 4-year) was 0.57 cm and spatial averaged dilation rate was 0.22 cm annually.

5.2.3 Patient-specific 3WK parameters

The 3WK parameters were computed for this patient with the proposed approach (Sec. 2.3.2), as listed in Table 5.2. The comparison between these values computed specifically for this patient and the available published results is shown in Tab. 5.3. They are consistent within a range of a similar order of magnitude [131, 132, 133, 134, 135, 136, 137, 138]. The 3WK parameters for the renal and common iliac arteries was not available in previous studies to compare, which are included our geometric models.

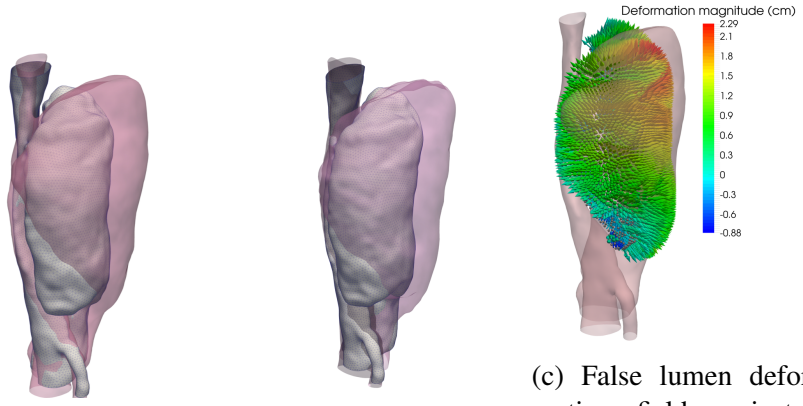

(a) Pre-aligned

(b) Registered

(c) False lumen deformation field projected onto the normal direction of the FL surface.

Figure 5.2: Registration of FLs between initial and follow-up cases. (a) False lumens in 2006 and 2010 were pre-aligned based on the entry tears and true lumens before registration. (b) FL in 2006 was registered to 2010. (d) Three dimensional deformation field characterizing aneurysmal dilation was computed based on registration results. The deformation field was projected to the surface normal direction (outward) of the FL. The surface of the FL in 2006 is presented by the dark gray point cloud, while that in 2010 is in pink. The deformation vector field is color coded by the deformation magnitude and is positive if the deformation vector is in the direction of the normal , negative if opposite. Therefore positive deformation magnitude means dilation and negative means shrinking.

Table 5.2: Patient specific windkessel parameters of the initial and follow-up dissected aortas.

Artery	Windkessel parameters		
	R_p	R_d	C
	$10^3 \mathrm{dyn} \cdot \mathrm{s/cm}^5$	$10^4 \mathrm{dyn} \cdot \mathrm{s/cm}^5$	$10^{-4} \mathrm{cm}^5/\mathrm{dyn}$
	(2006, 2010)	(2006, 2010)	(2006, 2010)
Brachiocephalic artery	(1.22, 0.81)	(7.67, 5.11)	(2.86, 4.21)
Left common carotid	(2.73, 2.02)	(1.72, 1.28)	(1.25, 1.68)
Left subclavian	(1.77, 1.58)	(1.12, 0.99)	(1.92, 2.16)
Mensenteric artery	(2.26, 1.36)	(1.42, 0.86)	(1.51, 2.51)
Left renal	(4.73, 3.90)	(2.98, 2.46)	(0.72, 0.87)
Right renal	(4.74, 6.87)	(2.99, 4.33)	(0.72, 0.50)
Left common iliac	(1.53/2.60, 1.79)	(0.96/1.13, 1.13)	(2.23/1.31, 1.90)
Right common iliac	(1.31/1.97, 1.18)	(0.83/1.24, 0.75)	(2.60/1.73, 2.89)

Table 5.3: Previously published 3WK parameters of aortic branches including Brachiocephalic, left common carotid, left subclavian, as well as left and right external iliac arteries.

Artery	Reference	3WK parameters		
		R_p $(10^3 \mathrm{dyn} \cdot \mathrm{s/cm}^5)$	R_d $(10^3 \mathrm{dyn} \cdot \mathrm{s/cm}^5)$	C $(10^{-4} \mathrm{cm}^5/\mathrm{dyn})$
Brachiocephalic	[19]	0.13	3.06	3.5
	[139]	0.5	0.85	0.95
	[36]	0.63	1.71	1.01
Left Common Carotid	[140]	1.18	1.84	0.77
	[19]	0.15	1.95	0.64
	[139]	1.9	3.22	0.25
	[36]	1.76	4.17	0.41
	[141]	2.6	2.34	1.02
Left Subclavian	[140]	0.97	1.52	0.93
	[19]	0.20	1.52	0.83
	[139]	0.75	1.25	0.64
	[36]	2.41	5.47	0.31
	[141]	1.75	2.94	0.67
Left E. Iliac	[141]	0.85	1.42	0.29
Right E. Iliac	[141]	0.84	1.42	0.28

5.2.4 Assessment of the Leray-EFR model in the follow-up case

Mesh generation

The reconstructed geometries of the dissected aorta were discretized with the open source mesh generator NETGEN [111] and the Computational Geometry Algorithms Library (CGAL) [142] for the Finite Element Simulations. The mesh of the follow-up case is illustrated in Figure 5.1c. The detailed discretization information are shown in Table 5.4.

As it is well known, the mesh size must be carefully selected as a trade-off between accuracy and computational cost. A too coarse mesh may generate unstable or inaccurate numerical results, while a fine mesh generally guarantees more accuracy but it requires high computational costs. However, in practice the numerical error is not significantly improved beyond a certain level of refinement.

The Leray-EFR model allows using relatively coarse meshes to obtain accurate solu-

tions, which is a significant advantage in reducing the computational cost. This computational advantage is tested in this study. More precisely, two meshes (denoted hereafter by *Follow-up* and *Follow-up**) at different refinement levels for the follow-up case were generated. The finest mesh, Follow-up*, was used for a DNS of the problem at hand, to provide a ground-truth numerical solution to be compared with the Leray results. It is worth noting that we assessed the level of refinement of the DNS mesh with an even finer mesh (around 4M elements vs the 1M elements of the *Follow-up** case) with no significant change in the solution. The Leray-EFR result was obtained using the mesh *Follow-up* with a significantly less computing time, with a 80% reduction compared to that of DNS.

Table 5.4: Discretization of initial and follow-up dissected aortas. h_{min}, h_{avg}, h_{max} are the minimum, average and maximum mesh size, respectively.

Case	Discretization				
	Mesh type	Mesh No.	h_{min}/cm	h_{avg}/cm	h_{max}/cm
Initial (2006)	Tetrahedron	934k	1.30e-2	2.19e-2	4.04e-1
Follow-up (2010)	Tetrahedron	645k	1.13e-2	3.43e-2	5.32e-1
Follow-up* (2010)	Tetrahedron	1063k	7.50e-4	2.09e-2	3.01e-1

The general flow distributions were consistent between DNS and Leray-EFR, maximum velocities at each major locations of the aorta, as well as WSS quantities were within 10% difference between two simulations despite the 40% difference in number of elements. Thus we consider the result obtained using the Leray model with the coarser mesh (*Follow-up*) is representative of the hemodynamics in the follow-up case.

5.2.5 Hemodynamic quantities of interest

The hemodynamics of the initial and follow-up cases were simulated using the Leray-EFR model with comparable discretizations.

Table 5.5: Heymodynamic properties.

Hemodynamic properties		2006	2010	2010*
Max peak velocity, cm/s	Ascending	104.7	79.5	85.9
	Arch	73.6	49.5	36.3
	Proximal to entry	179.7	134.0	145.9
	Distal to entry	114.3	112.9	86.7
	Entry tear	216.3	146.4	156.0
Flow Splitting, %	TL	41.8	46.4	44.0
	FL	58.2	53.6	56.0
Peak systolic WSS, dyn/cm^2	Max on FL	22.8	14.6	12.5
	Average on FL	3.2	0.61	0.79
	Entry tear	155.7	124.4	102.3
Time averaged WSS, dyn/cm^2	Max on FL	17.1	9.7	7.4
	Average on FL	2.2	0.75	0.56
	Entry tear	130.4	43.3	46.9
Time averaged WSS gradient, dyn/cm^3	Max on FL	266.8	97.9	-
	Average on FL	3.6	1.7	-
	Entry tear	251.6	240.1	-
Oscillatory shear index	Max on FL	0.5	0.5	0.5
	Average on FL	0.12	0.19	0.17

Velocity and pressure fields

Streamlines of the blood flow at systolic peak of both initial and follow-up cases are shown in Figure 5.3. In both cases, the flow has a significant speed up at the entry tear ($216.3\,\mathrm{cm/s}$ vs $146.4\,\mathrm{cm/s}$). Significant re-circulation of blood flow was observed inside both FLs, as shown in Figure 5.4. The flow in the follow-up cases after remodeling is slower and more helical than that in the initial case in general, as shown in Table 5.5 and Figure 5.5, respectively. The portion of the blood flows into the FL in the initial case is higher (58.2 % vs 53.6 %). The pressure of the TL in 2006 is relatively higher than that of the FL at the location distal to the entry tear. After 4 years, the pressure in the FL is higher than that of TL. This corresponds to the reduced blood flowing into the FL.

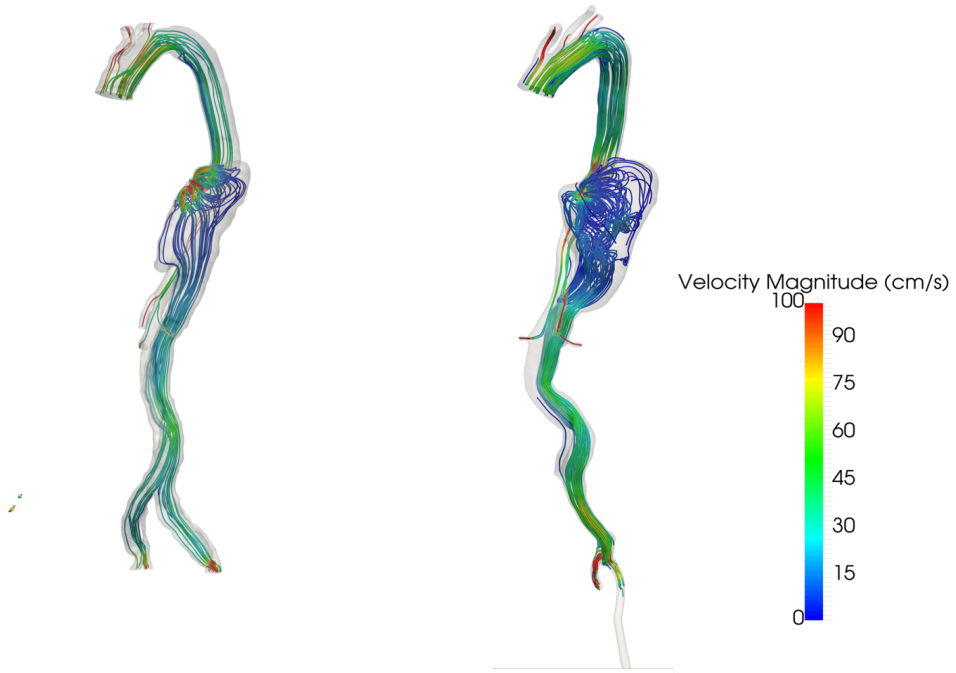

(a) Initial (b) Follow-up

Figure 5.3: Blood flow at peak systole. Streamlines here are color-coded by velocity magnitude.

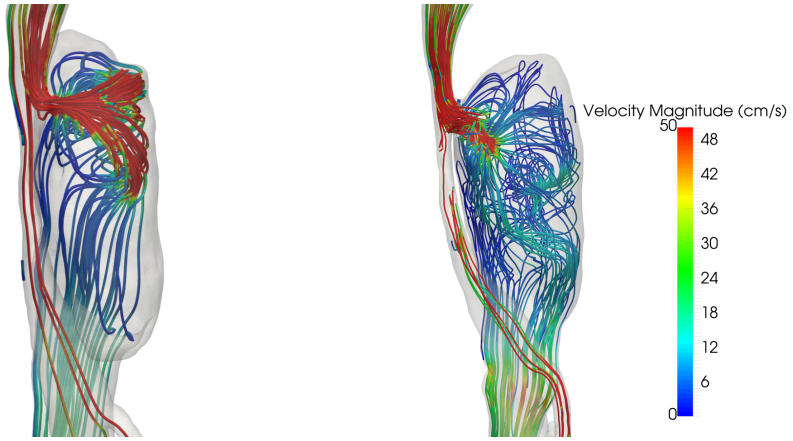

(a) Initial (b) Follow-up

Figure 5.4: Significant recirculation was observed in both initial and follow-up FLs at peak systole. Streamlines here are color-coded by velocity magnitude.

TAWSS, OSI and RRT

The TAWSS contour plots are shown in Figure 5.6. The FL of the initial case has higher maximum (17.1 vs 9.7 dyn/cm^2) and spatial averaged TAWSS (2.2 vs 0.75 dyn/cm^2) than

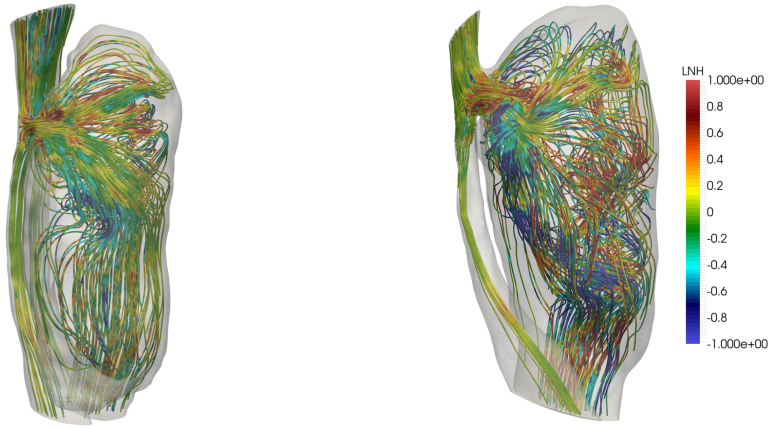

(a) Initial (b) Follow-up

Figure 5.5: Local Normalized Helicity.

the follow-up case does. The maximum TAWSS of the whole aorta located at the entry tear for both cases (130.4 vs 43.3 dyn/cm^2), as shown in Table 5.5.

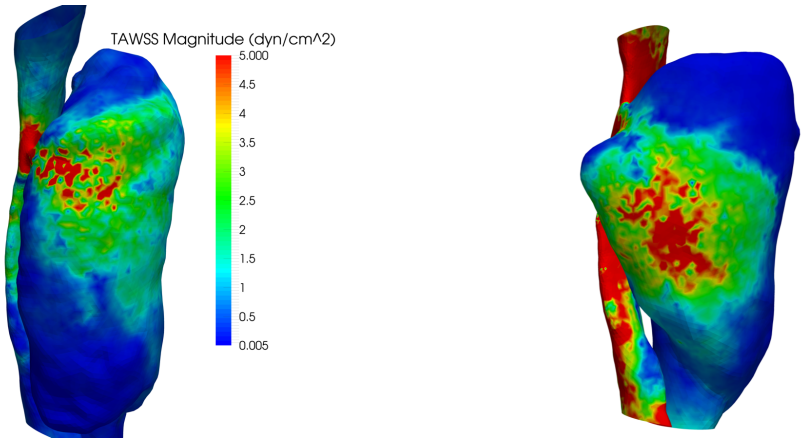

(a) Initial (b) Follow-up

Figure 5.6: Time averaged wall shear stress on FL.

OSI contour plots are shown in Figure 5.7. The surface with highly oscillatory WSS was in the distal of the FL in the initial case. It shifted to the proximal with the further aneurysmal dilation. The averaged OSI on FL is higher in the follow-up case (0.12 vs 0.19).

RRT around the FL surface is shown in Figure 5.8. High RRT indicates residence time of blood particles near the wall (arguably proxy for low and oscillatory WSS). Relatively

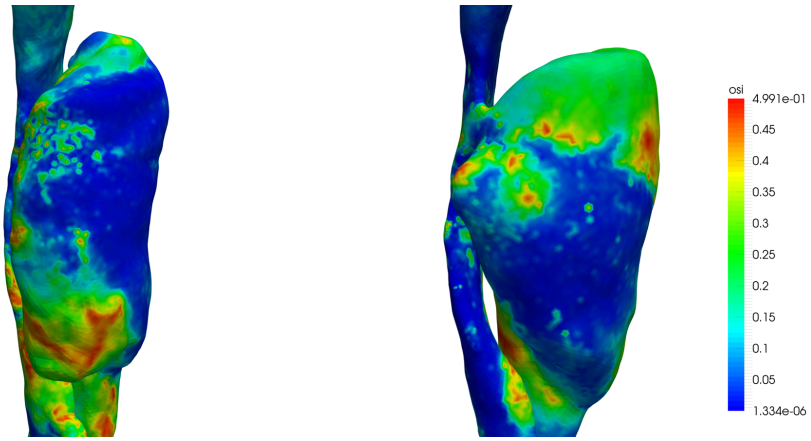

(a) Initial (b) Follow-up

Figure 5.7: Oscillatory shear index on FL.

low RRT was observed on majority of the wall of FL in both initial and follow-up cases. However, there was a small region with high RRT (over 100 cm^2/dyn) on the distal part of the initial FL and it was shifted to the proximal part at the follow-up case.

5.2.6 Correlation between FL deformation and hemodynamic properties

As illustrated in Fig. 5.9, the TAWSS positively correlates with FL dilation. However, the positive correlation is true only for low TAWSS. Interestingly, the magnitude of dilation reached a plateau (about 1.5 cm) at TAWSS of around 2.5 dyn/cm^2, as shown in Figure 5.9a. For TAWSS beyond 2.5 dyn/cm^2, a substantial independence of the dilation on the TAWSS is observed. The detail of the correlation when the range of TAWSS is limited below this threshold is illustrated in Fig 5.9b. In fact, the r^2 increases from 0.25 to 0.44, as shown in Figure 5.9. A mild Negative correlation were found between OSI and deformation (r$^2 = 0.29$). The pattern of the RRT is more complex. Fig. 5.10 shows the RRT on the 2006 FL categorized into two classes (RRT $\geq$ 20 cm2/dyn). Clearly, the high RRT is only in the distal bottom of the FL. Fig. 5.10(right) shows the normal deformation d on the 2006 FL. We split four groups: $d \leq -0.5$, $-0.5 \leq d \leq 0$, $0 \leq d \leq 1.5$ and $d > 1.5$ (in cm). It is evident that there are two regions with negative deformations over the years. One region is in the distal bottom part of the FL, and features the largest negative deformation. The

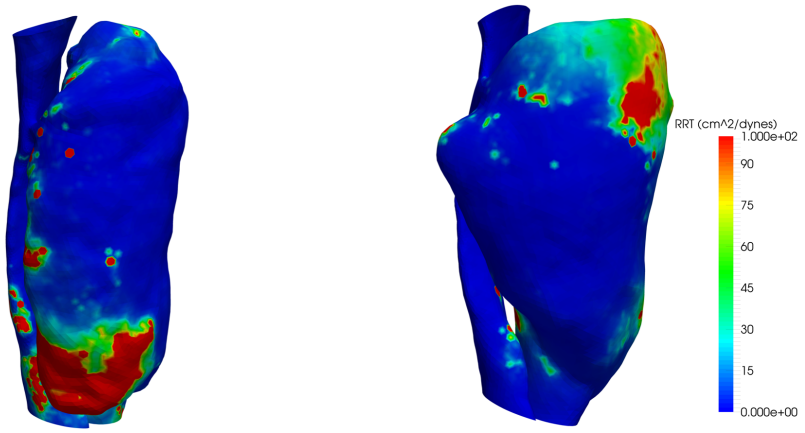

(a) Initial (b) Follow-up

Figure 5.8: Relative residence time. High flow resident time were shown to be related to thrombosis [128, 143]. Meanwhile, the patency of the FL is a significant risk facor of FL dilation [144, 16]. For this patient, low RRT were observed in both initial and follow-up FL, which agrees with the lack of significant thrombosis.

other region is around the entry tear. The RRT is clearly correlated to the former shrinking region.

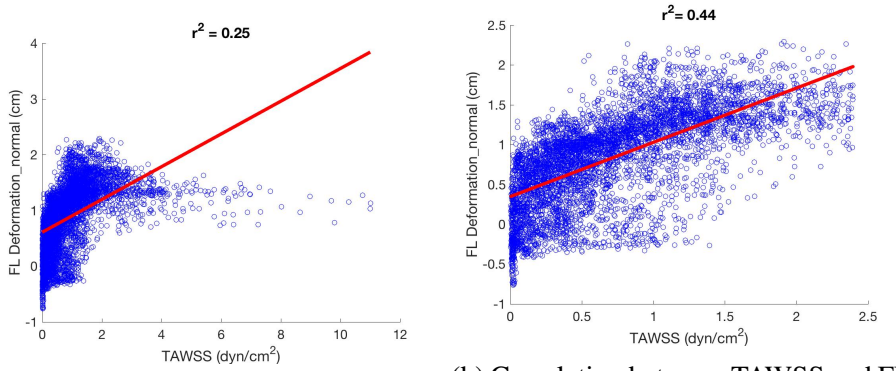

(a) Correlation between TAWSS and FL deformation.

(b) Correlation between TAWSS and FL deformation with TAWSS less than 2.5 dyn/cm^2.

Figure 5.9: Correlation between FL deformation and time averaged wall shear stress.

5.3 A Cross-Sectional Study - A Multi-Patient Study

Codner and his coworkers from Emory University School of Medicine [15] recently identified the location of the Primary Intimal Tear (PIT) as a predictor of aortic growth in acute

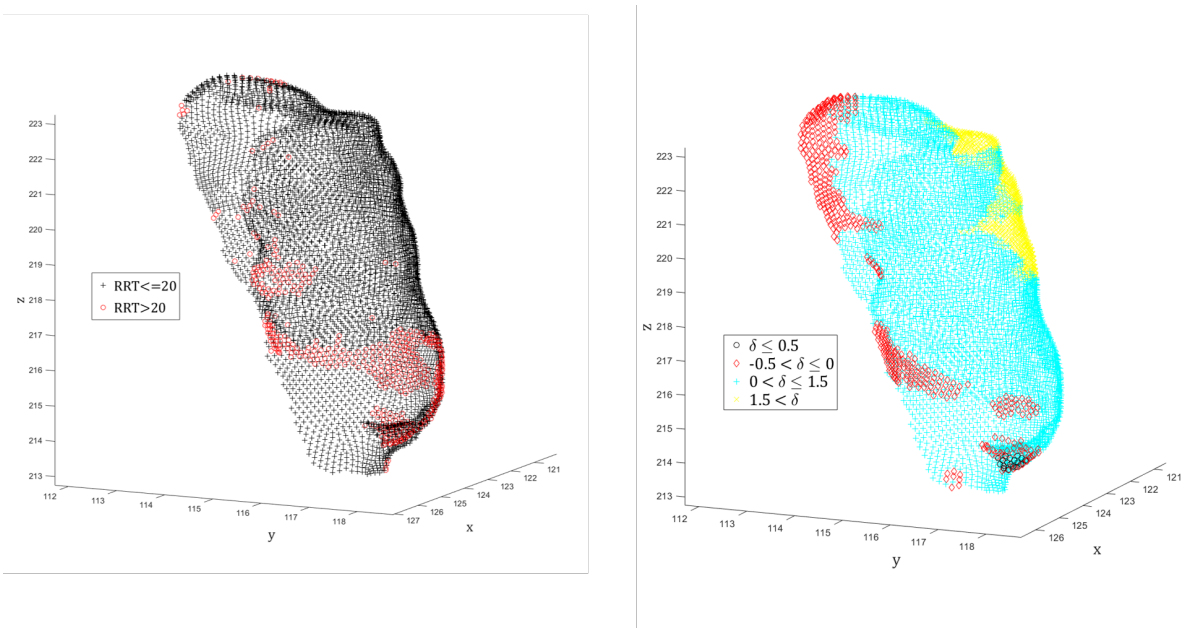

Figure 5.10: Correlation between RRT and FL deformation. Left: Stratification of the RRT on the 2006 FL (black: RRT ≤ 20 cm^2/dyn; red: RRT > 20 cm^2/dyn). Right: Stratification of the normal deformation in 4 groups (unit: cm): $d \leq -0.5$, $-0.5 \leq d \leq 0$, $0 \leq d \leq 1.5$ and $d > 1.5$. It is evident that there are two regions with negative deformations over the years. One region is the distal bottom part of the FL, which features the largest negative deformation. The other region is around the entry tear. The RRT is clearly correlated to the former shrinking region.

uTBAD under OMT. The study was a retro-perspective study analyzing the medical images of 121 patients (growth group $n = 71$ vs. no growth group $n = 49$) under OMT after diagnosed with uTBAD. The distances between the distal edge of the Left Subclavian Artery (LSA) and the proximal edge of the PIT of the FL are compared between the two groups. It was found that aforementioned distances of the growth group are statistically significantly shorter compared to those of the no growth group (growth: 27 mm [9-66 mm] vs. no growth: 77 mm [26-142 mm]; $P < .01$). However, there is no clear criterion determined for the distance between LSA and PIT to be directly used as a predictor, since there is a significant overlap in the distribution of the distances (growth: [9-66 mm] vs. no growth: [26-142 mm]).

Inspired by this study [15], a small cohort of five acute uTBAD patients from EUH are selected in this work for a cross-sectional study, whose purpose is to investigate the poten-

Table 5.6: Comparison between the quantities of interests at the location of the entry tear between the growth and no growth groups of acute uTBAD patients. Here *Distance(LSA, PIT)* denotes the distance between the distal edge of the LSA and the proximal edge of the PIT. *Max_TAWSS_PIT, Avg_TAWSS_PIT, Avg_OSI_PIT, Avg_Vel_PIT* represent the maximum TAWSS, spatially averaged TAWSS, spatially averaged OSI and spatially averaged velocity at the PIT, respectively

QoIs	Growth		No growth		
	g1	g2	ng1	ng2	ng3
Distance(LSA, PIT), cm	3.31	2.14	2.05	2.88	3.14
Max_TAWSS_PIT, dyn/cm2	164.70	49.27	35.18	8.31	47.01
Avg_TAWSS_PIT, dyn/cm2	7.63	4.48	5.70	2.22	4.19
Avg_OSI_PIT	0.18	0.21	0.13	0.19	0.12
Avg_Vel_PIT, cm/s	130.61	70.96	86.91	35.12	48.74

tial hemodynamic difference for patients who had similar distance between LSA and PIT but with different clinical outcomes (growth vs. no growth). The selected five patients were also diagnosed of acute uTBAD and initially treated with OMT. Two of them are from the growth group (labeled as patients g1 and g2), who developed FL aneurysmal degeneration and received intervention by the time of this study. The rest of the three patients are from the no growth group (labeled as patients ng1, ng2 and ng3). More importantly, there is no significant difference for the distance between their LSA and PIT, as detailed in Tab. 5.6. It is worth noting that this is only a preliminary study with a small number of patients, which is intended to be a pilot of a statistical significant retrospective study in the future.

Hemodynamics in all five patients from two groups are simulated using the Leray-EFR model and TAWSS, OSI and RRT are computed based on the simulation results. As shown in Tab. 5.6, the distance between LSA and PIT for the patients in the growth group is not shorter than those in the no growth group. On the contrary, the patient g1 in the growth group has the longest distance between LSA and PIT. Interestingly, this patient has the largest spatially maximum TAWSS and averaged velocity at PIT among all five patients including the growth and no growth groups. This shows that although the PIT is further from the LSA for this patient, the blood flow at the proximal entry tear entering the FL is more significant, comparing to the those from the no growth group. This case further

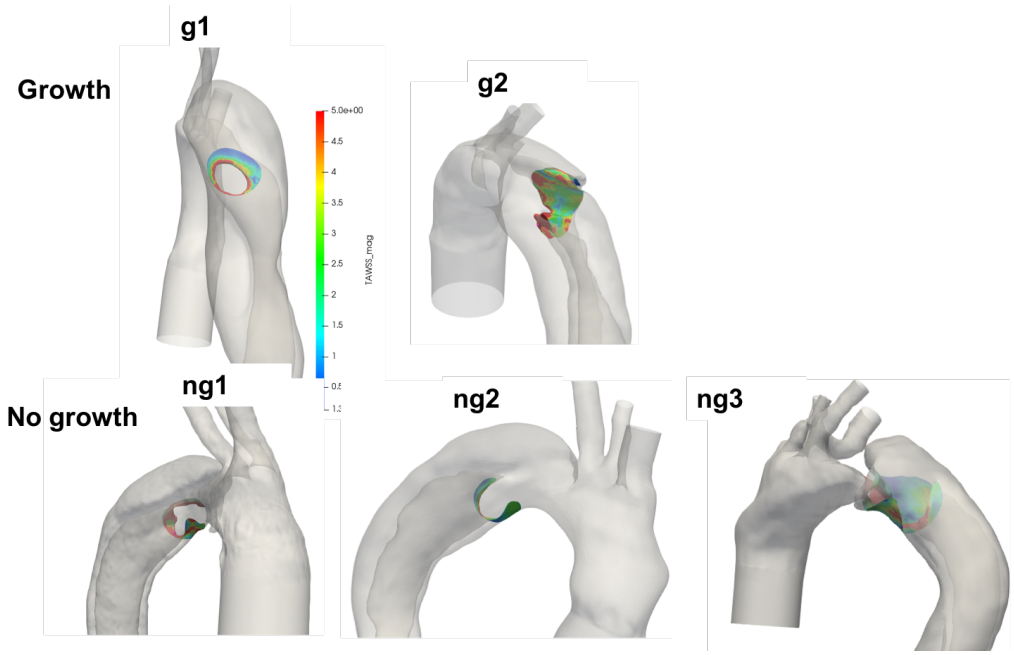

Figure 5.11: TAWSS at the location of the entry tear for all five acute uTBAD patients (growth: top row; no growth: bottom row.)

demonstrated that *the morphological indicator does not contain the complete picture when it comes to the prognostic factor for late FL degeneration.* The TAWSS and OSI at the location of PIT is shown in Fig. 5.11 and 5.12 respectively. Due to the more significant flow, the patient g1 has higher spatially maximum TAWSS and averaged TAWSS at PIT comparing to those of the no growth patients.

The TAWSS on the aortic wall for the five patients are shown in Fig. 5.13. In general, the TAWSS on the FLs of the growth group is relatively lower than those of the no growth group, except for the patient ng1. However, the distal part of the FL of the patient ng1 is fully thrombosed and therefore the virtually non-existing blood flow leads to the low TAWSS (close to zero). It has been shown from the longitudinal study from the previous section that relatively low TAWSS (TAWSS $<$ 2.5 dyn/cm^2) is positively correlated with the FL growth and no clear growth for the region with TAWSS larger than 2.5 dyn/cm^2. Although the TAWSS results for the five patients here are not enough to consolidate the criterion due to the individual variations and no longitudinal registration was performed,

the trend is similar.

The RRT on the aortic wall for the five patients are shown in Fig. 5.14. The fully thrombosed distal FL of patient ng1 corresponds to high RRT. However, no significant trend is observed between patients from the growth and no growth group. No clear trend was found for OSI, neither.

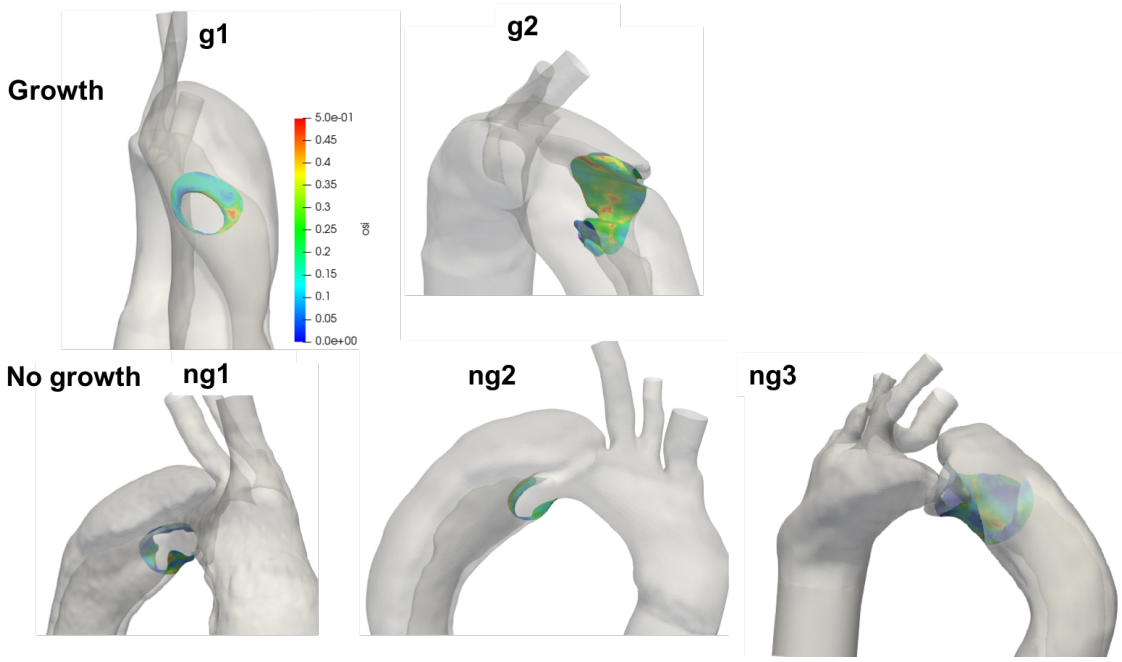

Figure 5.12: OSI at the location of the entry tear for all five acute uTBAD patients (growth: top row; no growth: bottom row.)

5.4 Discussion and Summary

The single patient study is based on a longitudinal data set of one patient with originally uTBAD, but late FL degeneration. On a basis of the rigorous quantification of the FL progression over the years, we detect possible correlations between the FL progression and several hemodynamics factors computed on the early-stage geometry. High TAWSS, low OSI, and RRT appear associated with FL evolution in this patient.

FL progression over the years, we detect possible correlations between the FL progression and several hemodynamics factors computed on the early-stage geometry. High

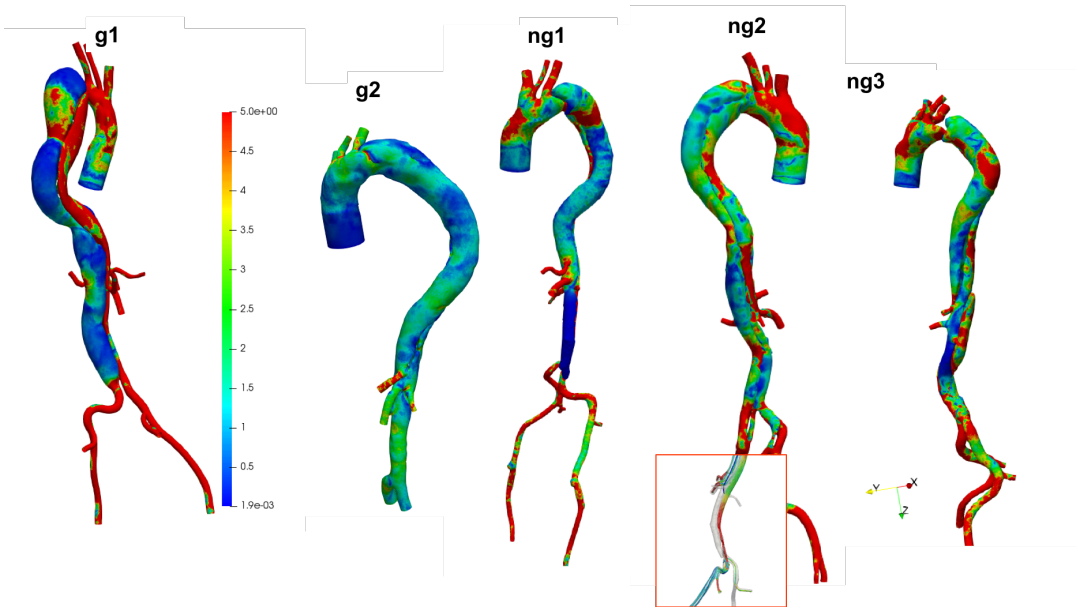

Figure 5.13: TAWSS on the aortic wall for all five acute uTBAD patients. The growth group: patients g1 and g2; The no growth group: patients ng1, ng2 and ng3.

TAWSS, low OSI, and RRT appear associated with FL evolution in this patient. A recent longitudinal study [24] used CFD laminar solver to identify predictive hemodynamic factors. The FL evolution was quantified by diameter and FL volume solely. The boundary conditions were prescribed by combining measures and literature data. As in our study, high RRT was indicated to be related to negative deformation. Another longitudinal study [20] with no patient-specific boundary data used inflow measurements from volunteers and literature outflow data. The aortic remodeling was quantified only by looking at the maximal diameter and luminal volume. Pressure in the FL was reduced in the follow-up case. A data assimilation study [19] focused on the calibration of 3WK parameters by rigorous minimization difference between the measured pressure and computed pressure from the laminar simulation. Parameters found for 3WK are consistent with our results. The overview of the literature above highlights the novelty of our work at the methodological level. As the FL expansion rate has been recognized in the imaging literature as a critical factor, there has been no consensus on quantitative criteria [14, 13, 12, 11, 144].

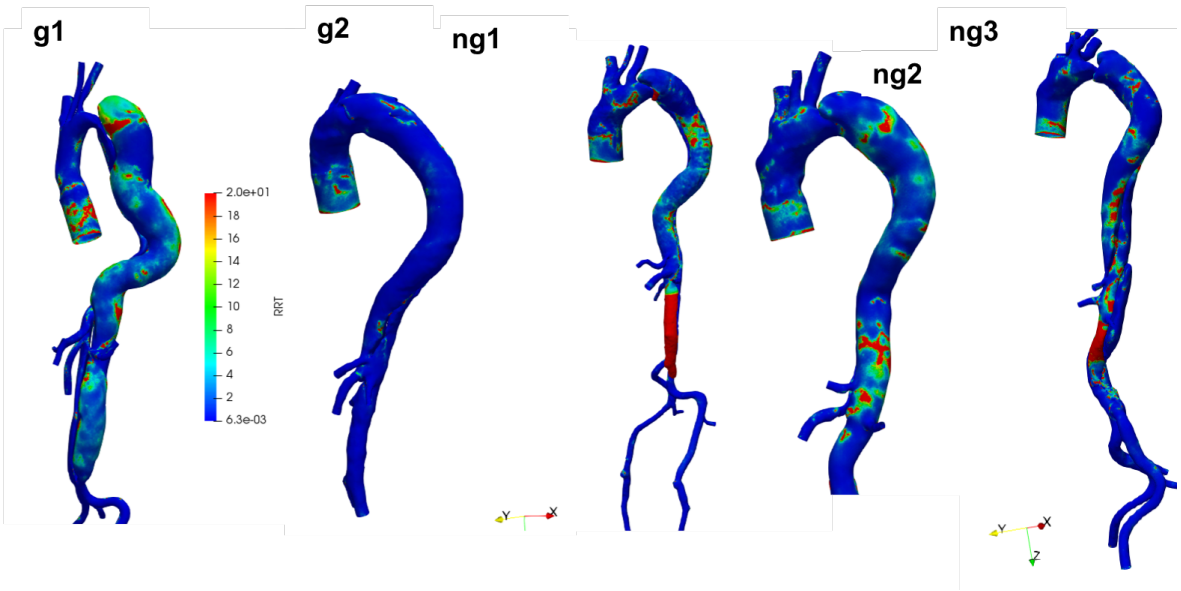

Figure 5.14: RRT on the aortic wall for all five acute uTBAD patients. The growth group: patients g1 and g2; The no growth group: patients ng1, ng2 and ng3.

A 3D comprehensive evaluation of the FL deformation combined with the evaluation of patient-specific hemodynamics represents a significant improvement to identify the prognostic factors of the FL aneurysmal dilation. In particular, the added value of our local analysis is to investigate different regional mechanisms related to different hemodynamic conditions.

The correlation of the TAWSS with the deformation of the FL is apparent only for the region with TAWSS below the threshold of 2.5 dyn/cm^2. For regions affected by larger values of the TAWSS, our study shows no correlation with the remodeling. A similar trend was observed in a previous study [145], where a direct dose–response relationship was observed between WSS and nitrogen oxides (NO) production in porcine aortic artery. A deeper analysis at the tissue level might facilitate identifying in detail the possible correlations between the two studies.

High RRT has been found to correlate with the thrombosis absorption [143, 24], which is usually considered as a positive event. In our patient, the registration analysis of the FL showed two regions with the negative deformation. One is in the neighborhood of the entry

tear. This may be associated with flow re-circulation that may induce fibrotic mechanisms. The other one with the more evident inward remodeling is in the distal bottom part of the FL, where the remodeling seems to be more related to a thrombotic mechanism, with a particle deposition opaque to the follow-up imaging. The correlation with high RRT is apparent only for the second region, consistent with the previous findings [128, 143].

High OSI was found related to intracranial aneurysm rupture in a previous study [146]. However, we found here a mild negative correlation between OSI and deformation. This indicates that OSI may not be the main factor for the FL evolution and other factors may have more important roles.

In the cross-sectional study of the five patients, high TAWSS, blood velocities at the PIT of the patients from the growth group comparing to those from the no growth group, despite that all patients have comparable distance between LSA and PIT. Relatively lower TAWSS were observed on the FL from patients of the growth group. No difference was observed between the growth group and no growth group in terms of the blood pressure, OSI and RRT.

Our study resorts to state-of-the-art techniques of image processing and computational hemodynamics, yet there are several limitations. The arterial wall is assumed to be rigid, as the computational costs of a systematic fluid–structure interaction simulation are out of reach on a large cohort of patients. In addition, we do not have patient-specific constitutive material model for the aortic wall. Furthermore, the patient-specific pressure and flow data for boundary conditions are missing. A flow rate of a patient from a previous publication with flat velocity profile was assumed due to the lack of patient-specific data. In vivo 3D velocity profile measured by PC-MRI has been shown to be more realistic than the flat profile when enforced as inflow boundary condition. The former should be enforced as boundary condition if available in the future follow-up studies. Finally, it is only a study involving a small number of patients, the methodology should be applied to large cohorts of patients in order to draw more substantial clinical conclusions. In the follow-up, we will

organize a clinical study in a way that boundary related data could be collected, yet meeting all the constraints of normal clinical practice. More in general, with the improvement of data collection and computational methods, we will remove many of those limitations. Nevertheless, the combined registration-CFD analysis presented here is a valuable tool to predict which patients with originally uTBAD will develop late complication requiring surgical intervention. In particular, the importance of an accurate local analysis of the geometrical changes over the years is apparent.

CHAPTER 6
IMPLEMENTATION

All the numerical simulations in this thesis are performed with in-house implementations. The Leray-EFR model is implemented in C++ and Python by leveraging on two parallel Finite Element libraries, LifeV and FEniCS, respectively.

The effectiveness of the filter in the Leray models is the key to the success of the model. The codes provide the implementation of the Van Cittert-Helmholtz deconvolution filter [32] with arbitrarily high orders of the approximated deconvolution.

Another critical aspect of Leray models for the LES of incompressible flows at moderately large Reynolds number is the selection of the filter radius. This drives the effective regularization of the filtering procedure, and its selection is a trade-off between stability (the larger, the better) and accuracy (the smaller, the better) [64]. Therefore, the codes provides the implementation of the adjoint equations of the model with respect to the filter radius for the local sensitivity analysis.

6.1 C++ Implementation

The Leray-EFR model is implemented in C++ by leveraging the Object-Oriented parallel C++ Finite Element library LifeV (”Library of Finite Element Five”), which is open source and distributed under the LGPL license on github [147, 148]. The library relies on third-party scientific libraries like Trilinos [149] for the solution of linear systems (data structures and algorithms); ParMETIS for mesh partitioning; SuiteSparse, as a support library extending the capabilities of Trilinos (EPetra, AztecOO, IFPack, Belos); BLAS/LAPACK

The C++ implementation is hosted on Bitbucket: https://bitbucket.org/alephy/lifev/src/ and FEniCS implementation is hosted on GitHub: https://github.com/DeconvolutionEFRemory/DeconvolutionEFR. The FiniCS code will be submitted to Journal of Open Source Software as H. Xu, D. Baroli, and A. Veneziani, DeconvolutionEFR: The large eddy simulation solver for incompressible flows with moderate large reynolds numbers.

libraries (generic or vendor-specific implementations). General-purpose and communication libraries are Boost C++ libraries for memory management (smart pointers); HDF5 for the storage of large data on file; MPI libraries. For patient-specific large scale simulations, the code is deployed onto the stampede2 in the Extreme Science and Engineering Discovery Environment (XSEDE) supported by the National Science Foundation.

6.2 Python Implementation

The python package Leray-α-NL (name to be determined) [150] also implements the deconvolution-based Leray model to provide an alternative for Python users. This package builds on the parallel Finite Element library FEniCS for the discretization of the partial differential equations, FENaPack [151] for preconditioning (the "pressure convection–diffusion" preconditioner) and PETSc [152] for scalable linear solvers.

This package reads input parameters from a YAML configuration file (typically called 'input.yaml') that is located in the simulation output directory (i.e. directory where the numerical results will be written). Structured and unstructured meshes are supported in XDMF format using the build-in class XDMFFILE in Dolfin. The class XDMFFILE is also adopted for writing functions and meshes XDMF ((http://www.xdmf.org)) format. It writes an XML file that describes the data and points to a HDF5 file that stores the actual problem data. Output of data in parallel is supported. XDMF is not suitable for checkpointing as it may decimate some data.

6.3 Virtualization

Containerization has been widely used in the scientific computing community in recent years for its benefits of encapsulation, reproduciblility and portability for both code developers and end-users [153, 154, 155]. Singularity is the container suitable for high performance computing environment and it has been shown with only a negligible performance overhead [154]. By taking advantage of the availability of singularity on Comet and Stam-

pede2 from the Extreme Science and Engineering Discovery Environment (XSEDE), the singularity recipe has been developed for the Leray application code in this study to improve the mobility of the code and the reproduciblity of the numerical simulations. Moreover, the large amount of third-party dependencies of the code prohibits the accessibility of the code from the end-users or other potential developing contributors. With the Singularity container, the end-users and developers are able to use or work on the implementation without going through the “dependency-hell”.

CHAPTER 7
CONCLUSIONS AND OUTLOOK

This thesis is based on the hypothesis that the aortic hemodynamics plays a major role in the progression of the FL aneurysmal degeneration in uTBAD — corroborated by clinical evidence — and that the morphology is the link. In order to contribute to the search for the prognostic factors for the FL degeneration, this thesis has addressed several numerical challenges i.e. investigating the efficiency of a LES model (the Leray-EFR mode) in aortic simulations and its potential for the backflow stabilization; analyzing model uncertainty and other forms of uncertainty involved in the patient-specific simulations to quantify the confidence in model predictions; applying the model to simulating the hemodynamics of type B aortic dissections and correlate the hemodynamic factors with the 3D false lumen degeneration quantified by a registration method.

The LES-EFR model uses deconvolution filters and is the basis of the so-called Evolve-Filter-Relax scheme introduced by Layton, Rebholz and their collaborators as an effective alternative to Direct Numerical Simulations for the moderate or large Reynolds number flow. With a judicious selection of the parameters of this LES scheme, it is possible to suppress the term that triggers the numerical backflow instability, so to obtain reliable and efficient numerical simulations. Therefore, aortic simulations feature Reynolds numbers, flow regimes and boundary conditions that particularly benefit from this *serendipity* (aka 'two-birds-one-stone') circumstance, where a LES modeling is stabilizing a numerical artifact. Moreover, minimal influence of the model parameter δ on clinically relevant quantities has been shown by the global sensitivity analysis, therefore model is robust for obtained clinical relevant results.

In the backflow stabilization analysis, the Leray-EFR model is proved rigorously to be able to implicitly stabilize the backflow instability. Our Theorem is based on energy

considerations and a continuity argument with respect to the parameters, particularly the relaxation parameter χ. With a judicious selection of the parameters of this LES scheme, it is possible to suppress the term that triggers the numerical backflow instability, so to obtain reliable and efficient numerical results. Comparing the popular flow extension approach, Leray-EFR is able to stabilize the backflow instability without introducing extra computational cost. This is particularly attractive in computational clinical studies, where many cases need to be studied within a relatively short time period. The proof is further demonstrated by numerical experiments in both simplified and patient-specific settings. Unfortunately, the proof does not give specific recipes for calibrating model parameters χ and δ. This requires an extensive sensitivity analysis including both χ and δ that is a work in progress.

In order to quantify the reliability of the model predictions, global sensitivity analysis using PCE based Sobol' indices is conducted in this thesis to investigate the impact of the filter radius of the Leray-EFR model, inflow rate, as well as the geometry on the hemodynamic simulations in aortas. The major conclusions of the results can be summarized as follow. (i) Arterial morphology has always been speculated to be an important factor affecting the computational hemodynamic predictions. This is confirmed by the results in this study: the geometry is the most influential uncertain input, comparing to the other inputs considered. Similar results were reported by previous studies on idealized geometries. *Therefore, it is crucial to use patient-specific geometry and to quantify the associated uncertainty to reliably predict clinical relevant results.* (ii) Minimal influence of the model parameter δ on clinically relevant quantities is shown by the Sobol' index of δ with respect to TAWSS and OSI. *The numerical results demonstrated that the clinical QoIs are quite insensitive to the filter radius and therefore the robustness of applying the Leray model in aortic simulations.* (iii) *Different hemodynamic indexes show a different level of reliability in space*, (at a specific location on the arterial wall, one is more trustworthy while the other is less so). In fact, the CoV results of TAWSS and OSI in the patient-specific AAA case

of this study seem to "complement each other", in the sense that one is more trustworthy in a specific region where the other is less and vice versa. This suggests that it is worth computing both in practice and complementing mutually the information they provide to have a complete reliable picture of the clinical condition of the patient, so to use one or the other QoIs in different regions of interest.

The Leray-EFR model is applied to investigate the prognostic factor for uTBAD developing late false lumen degeneration, therefore facilitate the treatment decision. This study first focuses on a single patient with a longitudinal imaging data for a comprehensive correlation analysis between morphological and functional (hemodynamics) factors. The preliminary results are promising. In particular, TAWSS and RRT were found correlated with the FL evolution. The local analysis of the hemodynamics correlation with the remodeling is informative for different mechanisms. Low TAWSS is associated with deformation only below a threshold that may be correlated to biological dynamics in the arterial wall. The RRT seems to be informative of the possible thrombotic dynamics occurring in the bottom part of the FL. Then a cross-sectional study of a small group of patients further demonstrated that *the morphological indicator does not contain the complete picture when it comes to the prognostic factor for late FL degeneration.* Further validation of these results is needed by applying the approach to a more significant cohort of patients, that could enable us to reach our ultimate goal of developing predictive algorithms based on this methodology.

Even though this thesis made significant advancement in studying Leray-EFR model and addressed some of the most challenging aspects involved in the study of uTBAD, future development is necessary. The backflow stabilization analysis of the Leray-EFR model in this thesis only provides a general guideline instead of specific recipes for calibrating model parameters χ and δ. This requires an extensive sensitivity analysis of the role of both χ and δ in the backflow stabilization. In quantifying the uncertainties in the inflow boundary condition, the simplified distribution with assumed parameters was adopted due to the lack of

the patients' population data. In the future work, with the presence of corresponding data, Bayesian inference framework, which incorporates an assume prior distribution and representative patients' data, should be adopted to obtain more realistic distributions. For the patient-specific study for uTBAD, the small cohort in this thesis is not enough for drawing clinical relevant conclusions. The information involved in each patient is vast and heterogeneous. In terms of morphology, it includes distance of the primary entry tear from the left subclavian artery, curvature of the aortic arch, torsion of the aortic arch, thickness of the intimal flap as well as the growth of the FL. In terms of hemodynamics, it includes pressure in the FL and the TL, TAWSS, RRT and vorticity. Statistical analysis, such Principal Component Analysis, should be applied to the functional (hemodynamics) and morphological data from a large cohort of patients to obtain the underlying prognostic factor for the late complications.

REFERENCES

[1] T. P. Tran and A. Khoynezhad, "Current management of type b aortic dissection," *Vascular health and risk management*, vol. 5, p. 53, 2009.

[2] C. A. Nienaber, H. Rousseau, H. Eggebrecht, S. Kische, R. Fattori, T. C. Rehders, G. Kundt, D. Scheinert, M. Czerny, T. Kleinfeldt, *et al.*, "Randomized comparison of strategies for type b aortic dissection the investigation of stent grafts in aortic dissection (instead) trial," *Circulation*, vol. 120, no. 25, pp. 2519–2528, 2009.

[3] R. Hebballi and J. Swanevelder, "Diagnosis and management of aortic dissection," *Continuing education in anaesthesia, critical care & pain*, vol. 9, no. 1, pp. 14–18, 2009.

[4] R. O. Afifi, H. K. Sandhu, S. S. Leake, M. L. Boutrous, V. Kumar, A. Azizzadeh, K. M. Charlton-Ouw, N. U. Saqib, T. C. Nguyen, C. C. Miller, *et al.*, "Outcomes of patients with acute type b (debakey iii) aortic dissection a 13-year, single-center experience," *Circulation*, vol. 132, no. 8, pp. 748–754, 2015.

[5] L. A. Pape, M. Awais, E. M. Woznicki, T. Suzuki, S. Trimarchi, A. Evangelista, T. Myrmel, M. Larsen, K. M. Harris, K. Greason, *et al.*, "Presentation, diagnosis, and outcomes of acute aortic dissection: 17-year trends from the international registry of acute aortic dissection," *Journal of the American College of Cardiology*, vol. 66, no. 4, pp. 350–358, 2015.

[6] R. P. Cambria, R. S. Crawford, J.-S. Cho, J. Bavaria, M. Farber, W. A. Lee, V. Ramaiah, C. J. Kwolek, G. T. Investigators, *et al.*, "A multicenter clinical trial of endovascular stent graft repair of acute catastrophes of the descending thoracic aorta," *Journal of vascular surgery*, vol. 50, no. 6, pp. 1255–1264, 2009.

[7] B. G. Leshnower, Y. M. Duwayri, E. P. Chen, C. Li, C. A. Zehner, J. N. Binongo, and R. K. Veeraswamy, "Aortic remodeling after endovascular repair of complicated acute type b aortic dissection," *The Annals of thoracic surgery*, vol. 103, no. 6, pp. 1878–1885, 2017.

[8] M. F. Conrad, S. Carvalho, E. Ergul, C. J. Kwolek, R. T. Lancaster, V. I. Patel, and R. P. Cambria, "Late aortic remodeling persists in the stented segment after endovascular repair of acute complicated type b aortic dissection," *Journal of vascular surgery*, vol. 62, no. 3, pp. 600–605, 2015.

[9] C. A. Nienaber, S. Kische, H. Rousseau, H. Eggebrecht, T. C. Rehders, G. Kundt, A. Glass, D. Scheinert, M. Czerny, T. Kleinfeldt, *et al.*, "Endovascular repair of

type b aortic dissection long-term results of the randomized investigation of stent grafts in aortic dissection trial," *Circulation: Cardiovascular Interventions*, vol. 6, no. 4, pp. 407–416, 2013.

[10] S. I. Schwartz, C. Durham, W. D. Clouse, V. I. Patel, R. T. Lancaster, R. P. Cambria, and M. F. Conrad, "Predictors of late aortic intervention in patients with medically treated type b aortic dissection," *Journal of vascular surgery*, vol. 67, no. 1, pp. 78–84, 2018.

[11] J.-M. Song, S.-D. Kim, J.-H. Kim, M.-J. Kim, D.-H. Kang, J. B. Seo, T.-H. Lim, J. W. Lee, M.-G. Song, and J.-K. Song, "Long-term predictors of descending aorta aneurysmal change in patients with aortic dissection," *Journal of the American College of Cardiology*, vol. 50, no. 8, pp. 799–804, 2007.

[12] S. Onitsuka, H. Akashi, K. Tayama, T. Okazaki, K. Ishihara, S. Hiromatsu, and S. Aoyagi, "Long-term outcome and prognostic predictors of medically treated acute type b aortic dissections," *The Annals of thoracic surgery*, vol. 78, no. 4, pp. 1268–1273, 2004.

[13] A. Lobato and P Puech-Leao, "Predictive factors for rupture of thoracoabdominal aortic aneurysm," *Journal of vascular surgery*, vol. 27, no. 3, pp. 446–453, 1998.

[14] A. Evangelista, V. Galuppo, D. Gruosso, H. Cuéllar, G. Teixidó, and J. Rodríguez-Palomares, "Role of entry tear size in type b aortic dissection," *Annals of cardiothoracic surgery*, vol. 3, no. 4, p. 403, 2014.

[15] J. A. Codner, X. Lou, Y. M. Duwayri, E. P. Chen, J. N. Binongo, R. Moon, W. D. Jordan Jr, and B. G. Leshnower, "The distance of the primary intimal tear from the left subclavian artery predicts aortic growth in uncomplicated type b aortic dissection," *Journal of vascular surgery*, vol. 69, no. 3, pp. 692–700, 2019.

[16] K. Akutsu, J. Nejima, K. Kiuchi, K. Sasaki, M. Ochi, K. Tanaka, and T. Takano, "Effects of the patent false lumen on the long-term outcome of type b acute aortic dissection," *European journal of cardio-thoracic surgery*, vol. 26, no. 2, pp. 359–366, 2004.

[17] T. Tsai, R Fattori, and S Trimarchi, "Long-term survival in patients presenting with type b acute aortic dissection: Insights from the international registry of acute aortic dissection," *Journal of Vascular Surgery*, vol. 45, no. 5, p. 1087, 2007.

[18] L. Formaggia, A. Quarteroni, and A. Veneziani, *Cardiovascular Mathematics: Modeling and simulation of the circulatory system*. Springer Science & Business Media, 2010, vol. 1.

[19] M. Alimohammadi, O. Agu, S. Balabani, and V. Díaz-Zuccarini, "Development of a patient-specific simulation tool to analyse aortic dissections: Assessment of mixed patient-specific flow and pressure boundary conditions," *Medical engineering & physics*, vol. 36, no. 3, pp. 275–284, 2014.

[20] D. Chen, M. Müller-Eschner, D. Kotelis, D. Böckler, Y. Ventikos, and H. von Tengg-Kobligk, "A longitudinal study of type-b aortic dissection and endovascular repair scenarios: Computational analyses," *Medical engineering & physics*, vol. 35, no. 9, pp. 1321–1330, 2013.

[21] Z. Cheng, C. Riga, J. Chan, M. Hamady, N. B. Wood, N. J. Cheshire, Y. Xu, and R. G. Gibbs, "Initial findings and potential applicability of computational simulation of the aorta in acute type b dissection," *Journal of vascular surgery*, vol. 57, no. 2, 35S–43S, 2013.

[22] E. K. Shang, D. P. Nathan, R. M. Fairman, J. E. Bavaria, R. C. Gorman, J. H. Gorman, and B. M. Jackson, "Use of computational fluid dynamics studies in predicting aneurysmal degeneration of acute type b aortic dissections," *Journal of vascular surgery*, 2015.

[23] K. M. Tse, P. Chiu, H. P. Lee, and P. Ho, "Investigation of hemodynamics in the development of dissecting aneurysm within patient-specific dissecting aneurismal aortas using computational fluid dynamics (cfd) simulations," *Journal of biomechanics*, vol. 44, no. 5, pp. 827–836, 2011.

[24] H. Xu, Z. Li, H. Dong, Y. Zhang, J. Wei, P. N. Watton, W. Guo, D. Chen, and J. Xiong, "Hemodynamic parameters that may predict false-lumen growth in type-b aortic dissection after endovascular repair: A preliminary study on long-term multiple follow-ups," *Medical Engineering & Physics*, 2017.

[25] H. Ha, M. Ziegler, M. Welander, N. Bjarnegård, C.-J. Carlhäll, M. Lindenberger, T. Länne, T. Ebbers, and P. Dyverfeldt, "Age-related vascular changes affect turbulence in aortic blood flow," *Frontiers in physiology*, vol. 9, p. 36, 2018.

[26] J. Leray, "Sur le mouvement d'un liquide visqueux emplissant l'espace," *Acta mathematica*, vol. 63, no. 1, pp. 193–248, 1934.

[27] A. Cheskidov, D. D. Holm, E. Olson, and E. S. Titi, "On a leray–α model of turbulence," *Proceedings of the Royal Society A: Mathematical, Physical and Engineering Sciences*, vol. 461, no. 2055, pp. 629–649, 2005.

[28] D. D. H. Bernard J. Geurts, *Leray and LANS modelling of turbulent mixing*, ser. 1-42 00. Journal of Turbulence, 2005, vol. 00.

[29] W. Layton and R. Lewandowski, "A high accuracy leray-deconvolution model of turbulence and its limiting behavior," *Analysis and Applications*, vol. 6, no. 01, pp. 23–49, 2008.

[30] W Layton and A Takhirov, "A test of a modular, wall adapted nonlinear filter model for underresolved flows," Technical Report TR-MATH 12-11, Department of Mathematics, University of Pittsburgh, Tech. Rep., 2012.

[31] W. Layton, C. C. Manica, M. Neda, and L. G. Rebholz, "Numerical analysis and computational testing of a high accuracy leray-deconvolution model of turbulence," *Numerical Methods for Partial Differential Equations: An International Journal*, vol. 24, no. 2, pp. 555–582, 2008.

[32] L Bertagna, A Quaini, and A Veneziani, "Deconvolution-based nonlinear filtering for incompressible flows at moderately large reynolds numbers," *International Journal for Numerical Methods in Fluids*, vol. 81, no. 8, pp. 463–488, 2016.

[33] J. G. Heywood, R. Rannacher, and S. Turek, "Artificial boundaries and flux and pressure conditions for the incompressible navier–stokes equations," *International Journal for Numerical Methods in Fluids*, vol. 22, no. 5, pp. 325–352, 1996.

[34] U. Morbiducci, R. Ponzini, D. Gallo, C. Bignardi, and G. Rizzo, "Inflow boundary conditions for image-based computational hemodynamics: Impact of idealized versus measured velocity profiles in the human aorta," *Journal of biomechanics*, vol. 46, no. 1, pp. 102–109, 2013.

[35] A. Quarteroni, A. Veneziani, and C. Vergara, "Geometric multiscale modeling of the cardiovascular system, between theory and practice," *Computer Methods in Applied Mechanics and Engineering*, vol. 302, pp. 193–252, 2016.

[36] S Pirola, Z Cheng, O. Jarral, D. O'Regan, J. Pepper, T Athanasiou, and X. Xu, "On the choice of outlet boundary conditions for patient-specific analysis of aortic flow using computational fluid dynamics," *Journal of Biomechanics*, vol. 60, pp. 15–21, 2017.

[37] R. M. Romarowski, A. Lefieux, S. Morganti, A. Veneziani, and F. Auricchio, "Patient-specific cfd modelling in the thoracic aorta with pc-mri–based boundary conditions: A least-square three-element windkessel approach," *International journal for numerical methods in biomedical engineering*, vol. 34, no. 11, e3134, 2018.

[38] A. Veneziani and C. Vergara, "Flow rate defective boundary conditions in haemodynamics simulations," *International Journal for Numerical Methods in Fluids*, vol. 47, no. 8-9, pp. 803–816, 2005.

[39] H. Xu, M. Piccinelli, B. G. Leshnower, A. Lefieux, W. R. Taylor, and A. Veneziani, "Coupled morphological–hemodynamic computational analysis of type b aortic dissection: A longitudinal study," *Annals of biomedical engineering*, vol. 46, no. 7, pp. 927–939, 2018.

[40] I. E. Vignon-Clementel, C. A. Figueroa, K. E. Jansen, and C. A. Taylor, "Outflow boundary conditions for three-dimensional finite element modeling of blood flow and pressure in arteries," *Computer methods in applied mechanics and engineering*, vol. 195, no. 29, pp. 3776–3796, 2006.

[41] L. Formaggia, A. Veneziani, and C. Vergara, "Flow rate boundary problems for an incompressible fluid in deformable domains: Formulations and solution methods," *Computer Methods in Applied Mechanics and Engineering*, vol. 199, no. 9-12, pp. 677–688, 2010.

[42] C Bertoglio, A Caiazzo, Y Bazilevs, M Braack, M Esmaily, V Gravemeier, A Marsden, O Pironneau, I. Vignon-Clementel, and W. Wall, "Benchmark problems for numerical treatment of backflow at open boundaries," *International Journal for Numerical Methods in Biomedical Engineering*, 2017.

[43] G. Arbia, I. Vignon-Clementel, T.-Y. Hsia, J.-F. Gerbeau, M. of Congenital Hearts Alliance (MOCHA) Investigators, *et al.*, "Modified navier–stokes equations for the outflow boundary conditions in hemodynamics," *European Journal of Mechanics-B/Fluids*, vol. 60, pp. 175–188, 2016.

[44] C. Bertoglio and A. Caiazzo, "A stokes-residual backflow stabilization method applied to physiological flows," *Journal of Computational Physics*, vol. 313, pp. 260–278, 2016.

[45] ——, "A tangential regularization method for backflow stabilization in hemodynamics," *Journal of Computational Physics*, vol. 261, pp. 162–171, 2014.

[46] C.-H. Bruneau and P Fabrie, "Effective downstream boundary conditions for incompressible navier–stokes equations," *International Journal for Numerical Methods in Fluids*, vol. 19, no. 8, pp. 693–705, 1994.

[47] K. Valen-Sendstad, M. Piccinelli, R. KrishnankuttyRema, and D. A. Steinman, "Estimation of inlet flow rates for image-based aneurysm cfd models: Where and how to begin?" *Annals of biomedical engineering*, vol. 43, no. 6, pp. 1422–1431, 2015.

[48] A. Brault, L. Dumas, and D. Lucor, "Uncertainty quantification of inflow boundary condition and proximal arterial stiffness–coupled effect on pulse wave propagation in a vascular network," *International journal for numerical methods in biomedical engineering*, vol. 33, no. 10, e2859, 2017.

[49] A. Boccadifuoco, A. Mariotti, S. Celi, N. Martini, and M. V. Salvetti, "Uncertainty quantification in numerical simulations of the flow in thoracic aortic aneurysms," *Institute of Structural Analysis and Antiseismic Research, School of Civil Engineering, National Technical University of Athens, NTUA, Athens, Greece*, pp. 6226–6249, 2016.

[50] S. Bozzi, U. Morbiducci, D. Gallo, R. Ponzini, G. Rizzo, C. Bignardi, and G. Passoni, "Uncertainty propagation of phase contrast-mri derived inlet boundary conditions in computational hemodynamics models of thoracic aorta," *Computer methods in biomechanics and biomedical engineering*, vol. 20, no. 10, pp. 1104–1112, 2017.

[51] S. Sankaran, H. J. Kim, G. Choi, and C. A. Taylor, "Uncertainty quantification in coronary blood flow simulations: Impact of geometry, boundary conditions and blood viscosity," *Journal of biomechanics*, vol. 49, no. 12, pp. 2540–2547, 2016.

[52] M. D'Elia and A. Veneziani, "Uncertainty quantification for data assimilation in a steady incompressible navier-stokes problem," *ESAIM: Mathematical Modelling and Numerical Analysis*, vol. 47, no. 4, pp. 1037–1057, 2013.

[53] S. Sankaran and A. L. Marsden, "A stochastic collocation method for uncertainty quantification and propagation in cardiovascular simulations," *Journal of biomechanical engineering*, vol. 133, no. 3, p. 031 001, 2011.

[54] S. Celi and S. Berti, "Three-dimensional sensitivity assessment of thoracic aortic aneurysm wall stress: A probabilistic finite-element study," *European journal of cardio-thoracic surgery*, vol. 45, no. 3, pp. 467–475, 2013.

[55] A. Boccadifuoco, A. Mariotti, K. Capellini, S. Celi, and M. V. Salvetti, "Validation of numerical simulations of thoracic aorta hemodynamics: Comparison with in vivo measurements and stochastic sensitivity analysis," *Cardiovascular Engineering and Technology*, pp. 1–19, 2018.

[56] J. S. Tran, D. E. Schiavazzi, A. M. Kahn, and A. L. Marsden, "Uncertainty quantification of simulated biomechanical stimuli in coronary artery bypass grafts," *Computer Methods in Applied Mechanics and Engineering*, vol. 345, pp. 402–428, 2019.

[57] A. A. Mishra, J. Mukhopadhaya, G. Iaccarino, and J. Alonso, "An uncertainty estimation module for turbulence model predictions in su2," *arXiv preprint arXiv:1803.00725*, 2018.

[58] J.-X. Wang, R. Sun, and H. Xiao, "Quantification of uncertainties in turbulence modeling: A comparison of physics-based and random matrix theoretic approaches," *International Journal of Heat and Fluid Flow*, vol. 62, pp. 577–592, 2016.

[59] T. A. Oliver and R. D. Moser, "Bayesian uncertainty quantification applied to rans turbulence models," in *Journal of Physics: Conference Series*, IOP Publishing, vol. 318, 2011, p. 042 032.

[60] L. Margheri, M. Meldi, M. Salvetti, and P. Sagaut, "Epistemic uncertainties in rans model free coefficients," *Computers & Fluids*, vol. 102, pp. 315–335, 2014.

[61] M. Emory, J. Larsson, and G. Iaccarino, "Modeling of structural uncertainties in reynolds-averaged navier-stokes closures," *Physics of Fluids*, vol. 25, no. 11, p. 110 822, 2013.

[62] W. Edeling, P. Cinnella, R. P. Dwight, and H. Bijl, "Bayesian estimates of parameter variability in the k–ε turbulence model," *Journal of Computational Physics*, vol. 258, pp. 73–94, 2014.

[63] J. Schaefer, S. Hosder, T. West, C. Rumsey, J.-R. Carlson, and W. Kleb, "Uncertainty quantification of turbulence model closure coefficients for transonic wall-bounded flows," *AIAA Journal*, vol. 55, no. 1, pp. 195–213, 2016.

[64] L. Bertagna, A. Quaini, L. G. Rebholz, and A. Veneziani, "On the sensitivity to the filtering radius in leray models of incompressible flow," in *Contributions to Partial Differential Equations and Applications*, Springer, 2019, pp. 111–130.

[65] T. Crestaux, O. Le Maiˆtre, and J.-M. Martinez, "Polynomial chaos expansion for sensitivity analysis," *Reliability Engineering & System Safety*, vol. 94, no. 7, pp. 1161–1172, 2009.

[66] K. Khanafer and R. Berguer, "Fluid–structure interaction analysis of turbulent pulsatile flow within a layered aortic wall as related to aortic dissection," *Journal of biomechanics*, vol. 42, no. 16, pp. 2642–2648, 2009.

[67] A. N. Kolmogorov, "Dissipation of energy in locally isotropic turbulence," in *Dokl. Akad. Nauk SSSR*, JSTOR, vol. 32, 1941, pp. 16–18.

[68] J. Smagorinsky, "General circulation experiments with the primitive equations: I. the basic experiment," *Monthly weather review*, vol. 91, no. 3, pp. 99–164, 1963.

[69] Y Bazilevs, V. Calo, J. Cottrell, T. Hughes, A Reali, and G Scovazzi, "Variational multiscale residual-based turbulence modeling for large eddy simulation of incompressible flows," *Computer Methods in Applied Mechanics and Engineering*, vol. 197, no. 1-4, pp. 173–201, 2007.

[70] P. Sagaut, *Large eddy simulation for incompressible flows: an introduction*. Springer Science & Business Media, 2006.

[71] W. J. Layton and L. G. Rebholz, *Approximate deconvolution models of turbulence: analysis, phenomenology and numerical analysis*. Springer Science & Business Media, 2012, vol. 2042.

[72] W. Layton, L. G. Rebholz, and C. Trenchea, "Modular nonlinear filter stabilization of methods for higher reynolds numbers flow," *Journal of Mathematical Fluid Mechanics*, vol. 14, no. 2, pp. 325–354, 2012.

[73] A. Quarteroni, R. Sacco, and F. Saleri, *Numerical mathematics*. Springer Science & Business Media, 2010, vol. 37.

[74] H. C. Elman, D. J. Silvester, and A. J. Wathen, *Finite elements and fast iterative solvers: with applications in incompressible fluid dynamics*. Oxford University Press (UK), 2014.

[75] A. Quarteroni, F. Saleri, and A. Veneziani, "Factorization methods for the numerical approximation of navier–stokes equations," *Computer methods in applied mechanics and engineering*, vol. 188, no. 1, pp. 505–526, 2000.

[76] A. Saltelli, M. Ratto, T. Andres, F. Campolongo, J. Cariboni, D. Gatelli, M. Saisana, and S. Tarantola, *Global sensitivity analysis: the primer*. John Wiley & Sons, 2008.

[77] R. G. Ghanem and P. D. Spanos, *Stochastic finite elements: a spectral approach*. Courier Corporation, 2003.

[78] B. Sudret, "Uncertainty propagation and sensitivity analysis in mechanical models–contributions to structural reliability and stochastic spectral methods," *Habilitationa diriger des recherches, Université Blaise Pascal, Clermont-Ferrand, France*, 2007.

[79] I. M. Sobol, "Sensitivity estimates for nonlinear mathematical models," *Mathematical modelling and computational experiments*, vol. 1, no. 4, pp. 407–414, 1993.

[80] B. Sudret, "Global sensitivity analysis using polynomial chaos expansions," *Reliability Engineering & System Safety*, vol. 93, no. 7, pp. 964–979, 2008.

[81] I. M. Sobol, "Global sensitivity indices for nonlinear mathematical models and their monte carlo estimates," *Mathematics and computers in simulation*, vol. 55, no. 1-3, pp. 271–280, 2001.

[82] R. H. Cameron and W. T. Martin, "The orthogonal development of non-linear functionals in series of fourier-hermite functionals," *Annals of Mathematics*, pp. 385–392, 1947.

[83] D. Xiu and G. E. Karniadakis, "Modeling uncertainty in flow simulations via generalized polynomial chaos," *Journal of computational physics*, vol. 187, no. 1, pp. 137–167, 2003.

[84] N. Wiener, "The homogeneous chaos," *American Journal of Mathematics*, vol. 60, no. 4, pp. 897–936, 1938.

[85] J. Bäck, F. Nobile, L. Tamellini, and R. Tempone, "Stochastic spectral galerkin and collocation methods for pdes with random coefficients: A numerical comparison," in *Spectral and high order methods for partial differential equations*, Springer, 2011, pp. 43–62.

[86] S. Hosder, R. Walters, and R. Perez, "A non-intrusive polynomial chaos method for uncertainty propagation in cfd simulations," in *44th AIAA aerospace sciences meeting and exhibit*, 2006, p. 891.

[87] D. Gottlieb and S. A. Orszag, *Numerical analysis of spectral methods: theory and applications*. Siam, 1977, vol. 26.

[88] R. C. Smith, *Uncertainty quantification: theory, implementation, and applications*. Siam, 2013, vol. 12.

[89] X. Huan, C. Safta, K. Sargsyan, G. Geraci, M. S. Eldred, Z. P. Vane, G. Lacaze, J. C. Oefelein, and H. N. Najm, "Global sensitivity analysis and estimation of model error, toward uncertainty quantification in scramjet computations," *AIAA Journal*, vol. 56, no. 3, pp. 1170–1184, 2018.

[90] J. Feinberg, "Some improvements and applications of non-intrusive polynomial chaos expansions," 2015.

[91] J. Feinberg and H. P. Langtangen, "Chaospy: An open source tool for designing methods of uncertainty quantification," *Journal of Computational Science*, vol. 11, pp. 46–57, 2015.

[92] L. Antiga, M. Piccinelli, L. Botti, B. Ene-Iordache, A. Remuzzi, and D. A. Steinman, "An image-based modeling framework for patient-specific computational hemodynamics," *Medical & biological engineering & computing*, vol. 46, no. 11, pp. 1097–1112, 2008.

[93] R. Kikinis, S. D. Pieper, and K. G. Vosburgh, "3d slicer: A platform for subject-specific image analysis, visualization, and clinical support," in *Intraoperative imaging and image-guided therapy*, Springer, 2014, pp. 277–289.

[94] Z Cheng, F. Tan, C. Riga, C. Bicknell, M. Hamady, R. Gibbs, N. Wood, and X. Xu, "Analysis of flow patterns in a patient-specific aortic dissection model," *Journal of biomechanical engineering*, vol. 132, no. 5, p. 051 007, 2010.

[95] C. D. Murray, "The physiological principle of minimum work i. the vascular system and the cost of blood volume," *Proceedings of the National Academy of Sciences*, vol. 12, no. 3, pp. 207–214, 1926.

[96] M. Zamir, P. Sinclair, and T. H. Wonnacott, "Relation between diameter and flow in major branches of the arch of the aorta," *Journal of biomechanics*, vol. 25, no. 11, pp. 1303–1310, 1992.

[97] A. Myronenko and X. Song, "Point set registration: Coherent point drift," *Pattern Analysis and Machine Intelligence, IEEE Transactions on*, vol. 32, no. 12, pp. 2262–2275, 2010.

[98] D. N. Ku, D. P. Giddens, C. K. Zarins, and S. Glagov, "Pulsatile flow and atherosclerosis in the human carotid bifurcation. positive correlation between plaque location and low oscillating shear stress.," *Arteriosclerosis, thrombosis, and vascular biology*, vol. 5, no. 3, pp. 293–302, 1985.

[99] A. L. Bowers and L. G. Rebholz, "Numerical study of a regularization model for incompressible flow with deconvolution-based adaptive nonlinear filtering," *Computer Methods in Applied Mechanics and Engineering*, vol. 258, pp. 1–12, 2013.

[100] A. Bowers, L. G. Rebholz, A Takhirov, and C Trenchea, "Improved accuracy in regularization models of incompressible flow via adaptive nonlinear filtering," *International Journal for Numerical Methods in Fluids*, vol. 70, no. 7, pp. 805–828, 2012.

[101] H. J. Kim, C. Figueroa, T. Hughes, K. Jansen, and C. Taylor, "Augmented lagrangian method for constraining the shape of velocity profiles at outlet boundaries for three-dimensional finite element simulations of blood flow," *Computer Methods in Applied Mechanics and Engineering*, vol. 198, no. 45, pp. 3551–3566, 2009.

[102] M. E. Moghadam, Y. Bazilevs, T.-Y. Hsia, I. E. Vignon-Clementel, A. L. Marsden, *et al.*, "A comparison of outlet boundary treatments for prevention of backflow divergence with relevance to blood flow simulations," *Computational Mechanics*, vol. 48, no. 3, pp. 277–291, 2011.

[103] C.-H. Bruneau and P Fabrie, "New efficient boundary conditions for incompressible navier-stokes equations: A well-posedness result," *ESAIM: Mathematical Modelling and Numerical Analysis-Modélisation Mathématique et Analyse Numérique*, vol. 30, no. 7, pp. 815–840, 1996.

[104] R. Temam, *Navier-Stokes equations and nonlinear functional analysis*. Siam, 1995, vol. 66.

[105] J. G. Heywood and R. Rannacher, "Finite element approximation of the nonstationary navier-stokes problem. i. regularity of solutions and second-order error estimates for spatial discretization," *SIAM Journal on Numerical Analysis*, vol. 19, no. 2, pp. 275–311, 1982.

[106] ——, "Finite element approximation of the nonstationary navier-stokes problem, part ii: Stability of solutions and error estimates uniform in time," *SIAM journal on numerical analysis*, vol. 23, no. 4, pp. 750–777, 1986.

[107] ——, "Finite element approximation of the nonstationary navier-stokes problem iii. smoothing property and higher order error estimates for spatial discretization," *SIAM Journal on Numerical Analysis*, vol. 25, no. 3, pp. 489–512, 1988.

[108] ——, "Finite-element approximation of the nonstationary navier-stokes problem. part iv: Error analysis for second-order time discretization," *SIAM Journal on Numerical Analysis*, vol. 27, no. 2, pp. 353–384, 1990.

[109] J. R. Womersley, "Method for the calculation of velocity, rate of flow and viscous drag in arteries when the pressure gradient is known," *The Journal of physiology*, vol. 127, no. 3, pp. 553–563, 1955.

[110] L. Formaggia, F. Saleri, and A. Veneziani, *Solving numerical PDEs: Problems, applications, exercises*. Springer Science & Business Media, 2012.

[111] J. Schöberl, "Netgen an advancing front 2d/3d-mesh generator based on abstract rules," *Computing and visualization in science*, vol. 1, no. 1, pp. 41–52, 1997.

[112] C. Geuzaine and J.-F. Remacle, "Gmsh: A 3-d finite element mesh generator with built-in pre-and post-processing facilities," *International journal for numerical methods in engineering*, vol. 79, no. 11, pp. 1309–1331, 2009.

[113] *The vascular modeling toolkit website, http://www.vmtk.org/.*

[114] F Auricchio, M Conti, A Lefieux, S Morganti, A Reali, F Sardanelli, F Secchi, S Trimarchi, and A Veneziani, "Patient-specific analysis of post-operative aortic hemodynamics: A focus on thoracic endovascular repair (tevar)," *Computational Mechanics*, vol. 54, no. 4, pp. 943–953, 2014.

[115] S Gupta, A. R. Popescu, R. De Freitas, D Thakrar, J Puthumana, J Carr, and M Markl, "Four-dimensional magnetic resonance flow analysis clarifies paradoxical symptoms in a patient with aortic bypass and retrograde flow mimicking subclavian steal," *Circulation*, vol. 125, no. 6, e347–e349, 2012.

[116] Y. Amano, R. Takagi, Y. Suzuki, T. Sekine, S. Kumita, and M. van Cauteren, "Three-dimensional velocity mapping of thoracic aorta and supra-aortic arteries in takayasu arteritis," *Journal of Magnetic Resonance Imaging*, vol. 31, no. 6, pp. 1481–1485, 2010.

[117] P. Vasava, P. Jalali, M. Dabagh, and P. J. Kolari, "Finite element modelling of pulsatile blood flow in idealized model of human aortic arch: Study of hypotension and hypertension," *Computational and mathematical methods in medicine*, vol. 2012, 2012.

[118] L Talbot and K. Gong, "Pulsatile entrance flow in a curved pipe," *Journal of fluid mechanics*, vol. 127, pp. 1–25, 1983.

[119] F. T. Smith, "Fluid flow into a curved pipe," *Proceedings of the Royal Society of London. A. Mathematical and Physical Sciences*, vol. 351, no. 1664, pp. 71–87, 1976.

[120] A.-V. Salsac, S. Sparks, J.-M. Chomaz, and J. Lasheras, "Evolution of the wall shear stresses during the progressive enlargement of symmetric abdominal aortic aneurysms," *Journal of Fluid Mechanics*, vol. 560, pp. 19–51, 2006.

[121] L. Ellwein, M. M. Samyn, M. Danduran, S. Schindler-Ivens, S. Liebham, and J. F. LaDisa, "Toward translating near-infrared spectroscopy oxygen saturation data for the non-invasive prediction of spatial and temporal hemodynamics during exercise," *Biomechanics and modeling in mechanobiology*, vol. 16, no. 1, pp. 75–96, 2017.

[122] J. Towns, T. Cockerill, M. Dahan, I. Foster, K. Gaither, A. Grimshaw, V. Hazlewood, S. Lathrop, D. Lifka, G. D. Peterson, *et al.*, "Xsede: Accelerating scientific discovery," *Computing in Science & Engineering*, vol. 16, no. 5, pp. 62–74, 2014.

[123] A. Quarteroni and A. Veneziani, "Analysis of a geometrical multiscale model based on the coupling of ode and pde for blood flow simulations," *Multiscale Modeling & Simulation*, vol. 1, no. 2, pp. 173–195, 2003.

[124] H. Xu, D. Baroli, and A. Veneziani, "Global sensitivity analysis of the nonlinear leray model using the polynomial chaos expansion based sobol' indices (in preparation)," 2019.

[125] A. Narayan and J. D. Jakeman, "Adaptive leja sparse grid constructions for stochastic collocation and high-dimensional approximation," *SIAM Journal on Scientific Computing*, vol. 36, no. 6, A2952–A2983, 2014.

[126] M. Alimohammadi, J. M. Sherwood, M. Karimpour, O. Agu, S. Balabani, and V. Díaz-Zuccarini, "Aortic dissection simulation models for clinical support: Fluid-

structure interaction vs. rigid wall models," *Biomedical engineering online*, vol. 14, no. 1, p. 34, 2015.

[127] A. Qiao, W. Yin, and B. Chu, "Numerical simulation of fluid-structure interaction in bypassed debakey iii aortic dissection," *Computer methods in biomechanics and biomedical engineering*, vol. 18, no. 11, pp. 1173–1180, 2015.

[128] Z. Cheng, N. B. Wood, R. G. Gibbs, and X. Y. Xu, "Geometric and flow features of type b aortic dissection: Initial findings and comparison of medically treated and stented cases," *Annals of biomedical engineering*, vol. 43, no. 1, pp. 177–189, 2015.

[129] C. Karmonik, S. Partovi, M. Müller-Eschner, J. Bismuth, M. G. Davies, D. J. Shah, M. Loebe, D. Böckler, A. B. Lumsden, and H. von Tengg-Kobligk, "Longitudinal computational fluid dynamics study of aneurysmal dilatation in a chronic debakey type iii aortic dissection," *Journal of vascular surgery*, vol. 56, no. 1, pp. 260–263, 2012.

[130] Z Cheng, C Juli, N. Wood, R. Gibbs, and X. Xu, "Predicting flow in aortic dissection: Comparison of computational model with pc-mri velocity measurements," *Medical engineering & physics*, vol. 36, no. 9, pp. 1176–1184, 2014.

[131] O. S. Randall, M. D. Esler, R. V. Calfee, G. F. Bulloch, A. S. Maisel, and B. Culp, "Arterial compliance in hypertension," *Australian and New Zealand journal of medicine*, vol. 6, no. 4, pp. 49–59, 1976.

[132] Z. Liu, C.-T. Ting, S. Zhu, and F. Yin, "Aortic compliance in human hypertension.," *Hypertension*, vol. 14, no. 2, pp. 129–136, 1989.

[133] R. H. Marcus, C. Korcarz, G. McCray, A. Neumann, M. Murphy, K. Borow, L. Weinert, J. Bednarz, D. D. Gretler, and K. Spencer, "Noninvasive method for determination of arterial compliance using doppler echocardiography and subclavian pulse tracings. validation and clinical application of a physiological model of the circulation.," *Circulation*, vol. 89, no. 6, pp. 2688–2699, 1994.

[134] N Stergiopulos, J. Meister, and N Westerhof, "Evaluation of methods for estimation of total arterial compliance," *American Journal of Physiology-Heart and Circulatory Physiology*, vol. 268, no. 4, H1540–H1548, 1995.

[135] D. Chemla, J.-L. Hébert, C. Coirault, K. Zamani, I. Suard, P. Colin, and Y. Lecarpentier, "Total arterial compliance estimated by stroke volume-to-aortic pulse pressure ratio in humans," *American Journal of Physiology-Heart and Circulatory Physiology*, vol. 274, no. 2, H500–H505, 1998.

[136] G. F. Mitchell, "Pulse pressure, arterial compliance and cardiovascular morbidity and mortality," *Current opinion in nephrology and hypertension*, vol. 8, no. 3, pp. 335–342, 1999.

[137] G. E. McVeigh, C. W. Bratteli, D. J. Morgan, C. M. Alinder, S. P. Glasser, S. M. Finkelstein, and J. N. Cohn, "Age-related abnormalities in arterial compliance identified by pressure pulse contour analysis aging and arterial compliance," *Hypertension*, vol. 33, no. 6, pp. 1392–1398, 1999.

[138] B. M. Pannier, A. P. Avolio, A. Hoeks, G. Mancia, and K. Takazawa, "Methods and devices for measuring arterial compliance in humans," *American journal of hypertension*, vol. 15, no. 8, pp. 743–753, 2002.

[139] P. Moireau, N. Xiao, M. Astorino, C. A. Figueroa, D. Chapelle, C. Taylor, and J.-F. Gerbeau, "External tissue support and fluid–structure simulation in blood flows," *Biomechanics and modeling in mechanobiology*, vol. 11, no. 1-2, pp. 1–18, 2012.

[140] H. J. Kim, I. E. Vignon-Clementel, C. A. Figueroa, J. F. LaDisa, K. E. Jansen, J. A. Feinstein, and C. A. Taylor, "On coupling a lumped parameter heart model and a three-dimensional finite element aorta model," *Annals of biomedical engineering*, vol. 37, no. 11, pp. 2153–2169, 2009.

[141] N. Xiao, J. D. Humphrey, and C. A. Figueroa, "Multi-scale computational model of three-dimensional hemodynamics within a deformable full-body arterial network," *Journal of computational physics*, vol. 244, pp. 22–40, 2013.

[142] C. Jamin, P. Alliez, M. Yvinec, and J.-D. Boissonnat, "Cgalmesh: A generic framework for delaunay mesh generation," *ACM Transactions on Mathematical Software (TOMS)*, vol. 41, no. 4, p. 23, 2015.

[143] V. Rayz, L Boussel, L Ge, J. Leach, A. Martin, M. Lawton, C McCulloch, and D Saloner, "Flow residence time and regions of intraluminal thrombus deposition in intracranial aneurysms," *Annals of biomedical engineering*, vol. 38, no. 10, pp. 3058–3069, 2010.

[144] E. Sueyoshi, I. Sakamoto, K. Hayashi, T. Yamaguchi, and T. Imada, "Growth rate of aortic diameter in patients with type b aortic dissection during the chronic phase," *Circulation*, vol. 110, no. 11 suppl 1, pp. II–256, 2004.

[145] R. M. Nerem, D. G. Harrison, R. W. Taylor, and W. R. Alexander, "Hemodynamics and vascular endothelial biology.," *Journal of cardiovascular pharmacology*, vol. 21, S6–S10, 1993.

[146] J. Xiang, S. K. Natarajan, M. Tremmel, D. Ma, J Mocco, L. N. Hopkins, A. H. Siddiqui, E. I. Levy, and H. Meng, "Hemodynamic–morphologic discriminants for intracranial aneurysm rupture," *Stroke*, vol. 42, no. 1, pp. 144–152, 2011.

[147] *Https://bitbucket.org/lifev-dev/lifev-release/wiki/home*.

[148] T. Passerini, A. Quaini, U. Villa, A. Veneziani, and S. Canic, "Validation of an open source framework for the simulation of blood flow in rigid and deformable vessels," *International journal for numerical methods in biomedical engineering*, vol. 29, no. 11, pp. 1192–1213, 2013.

[149] M. A. Heroux, R. A. Bartlett, V. E. Howle, R. J. Hoekstra, J. J. Hu, T. G. Kolda, R. B. Lehoucq, K. R. Long, R. P. Pawlowski, E. T. Phipps, *et al.*, "An overview of the trilinos project," *ACM Transactions on Mathematical Software (TOMS)*, vol. 31, no. 3, pp. 397–423, 2005.

[150] H. Xu, D. Baroli, and A. Veneziani, *Deconvolutionefr: The large eddy simulation solver for incompressible flows with moderate large reynolds numbers*, 2019.

[151] J. Blechta and M. Řehoř, *Fenapack 2016*, http://dx.doi.org/10.5281/zenodo.56754.

[152] S. Balay, S. Abhyankar, M. F. Adams, J. Brown, P. Brune, K. Buschelman, L. Dalcin, A. Dener, V. Eijkhout, W. D. Gropp, D. Karpeyev, D. Kaushik, M. G. Knepley, D. A. May, L. C. McInnes, R. T. Mills, T. Munson, K. Rupp, P. Sanan, B. F. Smith, S. Zampini, H. Zhang, and H. Zhang, *PETSc Web page*, `https://www.mcs.anl.gov/petsc`, 2019.

[153] Z. Sampedro, A. Holt, and T. Hauser, "Continuous integration and delivery for hpc: Using singularity and jenkins," in *Proceedings of the Practice and Experience on Advanced Research Computing*, ACM, 2018, p. 6.

[154] E. Le and D. Paz, "Performance analysis of applications using singularity container on sdsc comet," in *Proceedings of the Practice and Experience in Advanced Research Computing 2017 on Sustainability, Success and Impact*, ACM, 2017, p. 66.

[155] G. M. Kurtzer, V. Sochat, and M. W. Bauer, "Singularity: Scientific containers for mobility of compute," *PloS one*, vol. 12, no. 5, e0177459, 2017.

VITA

Huijuan Xu was born and raised in Anhui, China. She received her B.S. in Mechanical Engineering from Xi'dian University, Xi'an, China. She has worked within the Emory Center for Mathematics and Computing in Medicine under the direction of Prof. Alessandro Veneziani since 2015 and co-advised by Prof. Robert Nerem from the Georgia Institute of Technology. She also worked at Siemens Corporate Technology as a graduate intern during the summer of 2017 and 2019. Huijuan's research interests are in all aspects of computational mechanics from numerical algorithms, software development, and data analysis to solve interdisciplinary problems in engineering and physics.